

C

RAMAN SPECTROSCOPY OF Co^{2+} IN
MgO AND OF $\beta\text{-In}_2\text{Se}_2$.

by

JACQUES TRUDEL

©

A Thesis

submitted to the Faculty of Graduate Studies
and Research in partial fulfillment of the
requirements for the degree of
Doctor of Philosophy

Department of Physics
McGill University
Montreal, Quebec, Canada

August 1983

RAMAN SPECTROSCOPY OF Co^{2+} IN MgO AND OF $\beta\text{-In}_2\text{Se}_2$

STATEMENT OF ORIGINALITY

I report for the first time the electronic Raman spectra of Co^{2+} in MgO which is consistent with my theoretical predictions and the Raman spectrum of Co^{2+} in KZnF_3 [18]. I calculated the dynamical Jahn-Teller interaction of the E_g and T_{2g} vibrational modes with the excited spin-orbit levels of the $^4T_{1g}$ orbital ground state of the cobalt impurity. The inclusion of the coupling to the T_{2g} mode is essential to explain the electronic levels observed in the Raman spectra.

The temperature variation of the 300 cm^{-1} region in the Raman spectrum indicates (notwithstanding the claim of Guha [23]) that the 305 cm^{-1} peak belongs to the electronic Raman spectrum of Co^{2+} while the 280 cm^{-1} peak is an impurity induced vibrational mode in resonance with the acoustic modes at the boundary of the Brillouin zone.

I observed, for the first time, the layer to layer shear mode of $\beta\text{-In}_2\text{Se}_2$ (E_{2g}^2 : 19 cm^{-1}) so that now the vibrational Raman spectrum is complete. I calculated the force constants of the linear chain model for the shear mode; I found a very good agreement with the experimental frequencies and predicted the frequencies of the optically inactive shear modes.

ABSTRACT

We have observed the electronic transitions within the ${}^4T_{1g}$ ground state of Co^{2+} in MgO by Raman spectroscopy. We identified the $\Gamma_{6g} \rightarrow \Gamma_{8g}^1$ transition at 305 cm^{-1} and the $\Gamma_{6g} \rightarrow \Gamma_{8g}^2$ transition at 930 cm^{-1} ; the $\Gamma_{6g} \rightarrow \Gamma_{7g}$ transition is not seen and is lost in the two-phonon band. We also observed an impurity induced vibration mode at 280 cm^{-1} , in resonance with the acoustic phonon branches at the surface of the Brillouin zone. The position of the electronic levels cannot be explained by crystal field theory, with the spin-orbit interaction to second-order included. We have calculated the effect of a dynamical Jahn-Teller interaction and have shown, for the first time, the necessity to include the coupling to the T_{2g} mode, in addition to the coupling to the E_g mode, although Co^{2+} in MgO is a weak Jahn-Teller system.

We also used Raman spectroscopy to observe the vibrational modes of $\beta\text{-In}_2\text{Se}_2$. We observed, for the first time, the layer to layer shear mode (E_{2g}^2), at 19 cm^{-1} . The position of this peak and the others, at $42(E_{1g}^1)$, $117(A_{1g}^1)$, $179(E_{2g}^1)$, $181(E_{1g}^2)$ and $231\text{ cm}^{-1}(A_{1g}^2)$, follows the trend of the vibrational spectra of $\beta\text{-Ga}_2\text{S}_2$ and of $\beta\text{-Ga}_2\text{Se}_2$ [65]. Using the linear chain model, we calculated the shear force constants and deduced the position of the doublet (E_{2g}^1 and E_{1g}^2) with very good agreement with the experimental values.

RÉSUMÉ

Nous avons observé les transitions électroniques entre les niveaux de l'état fondamental $^4T_{1g}$ du Co^{2+} dans le MgO par spectroscopie Raman. Nous avons identifié la transition $\Gamma_{6g} \rightarrow \Gamma_{8g}^1$ à 305 cm^{-1} et la transition $\Gamma_{6g} \rightarrow \Gamma_{8g}^2$ à 930 cm^{-1} ; l'intensité de la transition $\Gamma_{6g} \rightarrow \Gamma_{7g}$ étant trop faible, le pic correspondant est enfoui dans le spectre de diffusion Raman par deux phonons. Nous avons également observé une vibration induite par Co^{2+} à 280 cm^{-1} qui est en résonance avec les phonons acoustiques de la surface de la zone de Brillouin. La position des niveaux électroniques ne peut être expliquée par la théorie du champ cristallin lorsque l'interaction spin-orbite au second ordre est incluse. Nous avons évalué l'effet de l'interaction Jahn-Teller dynamique et montré, pour la première fois, la nécessité d'inclure le couplage au mode T_{2g} , en plus du couplage au mode E_g , même si l'ion divalent de cobalt dans l'oxyde de magnésium est soumis à un faible effet Jahn-Teller.

Nous avons également utilisé la spectroscopie Raman pour étudier les modes vibratoires du $\beta\text{-In}_2\text{Se}_2$. Nous avons observé, pour la première fois, le mode de scission (E_{2g}^2) à 79 cm^{-1} ; les cinq autres pics observés sont situés à 42 (E_{1g}^1), 117 (A_{1g}^1), 179 (E_{2g}^1), 181 (E_{1g}^2) et 231 cm^{-1} (A_{1g}^2). La position des six pics suit le comportement des spectres vibratoires du $\beta\text{-Ga}_2\text{S}_2$ et du $\beta\text{-Ga}_2\text{Se}_2$ [65]. Utilisant le modèle de la chaîne linéaire, nous avons calculé les constantes de force des modes de scission et déduit la position du doublet (E_{2g}^1 et E_{1g}^2) confirmant les valeurs expérimentales.

ACKNOWLEDGEMENTS

I greatly appreciate the fruitful discussions with Dr. D. Walsh, my thesis director. I would like to thank Dr. L. Chase ($\text{MgO}:\text{Co}^{2+}$) and Dr. S. Jandl (In_2Se_2) for providing us with some of the samples used in the experiments. Special thanks to Dr. A. Poirier with whom was discussed the finer points of the theory. I also thank Mr. J. Auclair, research assistant, and Mr. F. Van Gils, technician, for their technical assistance.

I acknowledge the financial support and the encouragement of the Physics' department and gratefully thank Mrs. J. Hay for typing this thesis.

Glossary

Constants

Bohr magneton
Boltzmann's constant
Electronic charge
Gyromagnetic factor
Mass of electron
Planck's constant
Vacuum permittivity
Vacuum permeability
Velocity of light in vacuum
Avogadro's number

Units

Angstroms
Electron-volt
Kelvin (degree)
Kilogram
Meter
Millimeter
Nanometer
Second
Wavenumber

Symbols

$\beta = -9.2741 \times 10^{-24} \text{ J/tesla}$
 $k_b = 1.380 \times 10^{-23} \text{ J/deg.K}$
 $e = 1.602 \times 10^{-19} \text{ C}$
 $g_o = 2.0023$
 $m_e = 9.11 \times 10^{-31} \text{ kg}$
 $h = 6.626 \times 10^{-34} \text{ J s}$
 $\epsilon_o = 8.8542 \times 10^{-12} \text{ farad/m}$
 $\mu_o = 4\pi \times 10^{-7} \text{ henry/m}$
 $c = 2.998 \times 10^8 \text{ m/s}$
 $N_o = 6.022 \times 10^{23} \text{ mole}^{-1}$

Symbols

$\text{\AA} = 10^{-10} \text{ m}$
 $\text{eV} = 1.602 \times 10^{-19} \text{ J}$
 $^\circ \text{K}$
kg
m
 $\text{mm} = 10^{-3} \text{ m}$
 $\text{nm} = 10^{-9} \text{ m}$
s or sec
 $\text{cm}^{-1} = 1.24 \times 10^{-4} \text{ eV}$

<u>Terms</u>	<u>Abbreviations</u>
Cobaltous and cobaltic oxides	$\text{CoO}, \text{Co}_2\text{O}_3$
Collective mode operator	Q_α
Conjugate momentum operator	P_α
Covalency parameters	k, k'
Crystal field parameter	Dq
Divalent cobalt	Co^{2+}
Divalent magnesium	Mg^{2+}
Divalent oxygen	O^{2-}
Elastic constant of LCM	C_α^β ($\alpha = b, g, w; \beta = c, s$)
Electric vector of light	$\vec{E}_{i,s}$
Frequency	ω, Ω
Gallium selenide	Ga_2Se_2
Gallium sulfide	Ga_2S_2
Hamiltonian	H
Incident and scattered light	i, s (subscript)
Indium selenide	In_2Se_2
Infrared	IR
Ionic krypton	Kr^+
Irreducible representations	i.r., irrep
Jahn-Teller	jt, JT
JT coupling coefficients	V_e, V_t
JT energies	$E_{jt}(E), E_{jt}(T)$
JT orbital operators	E_α, T_β ($\alpha = \theta, \epsilon; \beta = \xi, \eta, \zeta$)
Linear chain model	LCM
Magnesium hydroxide	$\text{Mg}(\text{OH})_2$
Magnesium oxide	MgO

Terms

Mode effective mass
 Orbital angular momentum
 (effective)
 Orbital angular momentum
 operators
 Orbital angular momentum
 (total)
 Parity of an i.r.
 Phonon occupation numbers
 Phonon operators
 Phonon wavefunctions
 Point group of β -polytype
 Point group of γ -polytype
 Point group of ϵ -polytype
 Point group of the L point
 Point group of the octahedron
 Point group of the X point
 Points of high symmetry in
 the Brillouin zone
 Polarisation vectors
 Polytypes or stacking sequence
 Potassium zinc fluoride
 Racah's parameter
 Reciprocal lattice vector
 Spin operators
 Spin-orbit coupling constants
 (free-ion, first-,
 second-order)
 Term mixing parameter

Abbreviations

μ_e, μ_t
 ℓ_0
 $L_{\pm}, L_z, \ell_{\pm}, \ell_z$
 L
 $u = \text{odd}, g = \text{even}$ (subscript)
 n, n_0
 q_{α}, b, b^+
 u_{α} ($\alpha = 1, 2, 3$)
 D_{6h}
 C_{3v}
 D_{3h}
 D_{3d}
 O_h
 D_{4h}
 $L(\frac{1}{2}\frac{1}{2}\frac{1}{2}), X(001)$
 $\vec{e}_{i,s}$
 $\beta-, \gamma-, \epsilon-$
 $KZnF_3$
 B
 \vec{G}
 S_{\pm}, S_z
 $\lambda_0, \lambda, \lambda'$
 a

TermsAbbreviations

Total angular momentum
(effective)

j

Trivalent chromium ion

Cr^{3+}

Wavevector of light

$\vec{q}_{f,s}$

Wavevector of phonons

$\vec{k}_\alpha, \vec{k} \quad (\alpha = 1, 2)$

LIST OF FIGURES

<u>FIGURE</u>	<u>PAGE</u>
I-1. Raman and Rayleigh scattering	9
I-2. Cobalt impurity site in MgO	13
I-3. Energy levels of Co^{2+} in MgO	15
I-4. Experimental set-up	22
I-5. Sample space	26
I-6. Uniaxial pressure system	28 & 30
I-7. Orientation of sample S1A	47
I-8. Orientation of samples S2A, S3B, S4B and SP	49
I-9. Stokes Raman spectra of S1A and S2A	52
I-10. Spectrum of S1A with $L = 20717 \text{ cm}^{-1}$	54
I-11. Stokes Raman spectrum of S3B(Γ_{5g})	56
I-12. Stokes Raman spectrum of S3B($\Gamma_{1g} + \Gamma_{3g}$)	58
I-13. Stokes Raman spectrum of S2A($\Gamma_{1g} + \Gamma_{3g}$)	60
I-14. Stokes Raman spectra of S4B($T = 6$ to 292°K)	64 - 72
I-15. Dependence of $I(280 \text{ cm}^{-1})/I(305)$ with temperature	74
I-16. Local modes for an immobile impurity	77
I-17. Phonon frequency distribution	78
I-18. Stokes Raman spectrum of SP($\Gamma_{1g} + \Gamma_{3g}$)	81
I-19. Second-order Raman spectra of pure MgO	83
I-20. The Jahn-Teller energies	91
I-21. Energy levels of Co^{2+} at an octahedral site	99

<u>FIGURE</u>	<u>PAGE</u>
II-1. Structure of one layer of indium selenide	109
II-2. Stacking sequence of β -In ₂ Se ₂	110
II-3. Stacking sequence of ϵ - and γ -In ₂ Se ₂	112 & 113
II-4. Raman active modes of β -In ₂ Se ₂	117
II-5. Orientation and polarization of the sample	121
II-6. Raman spectra of β -Ga ₂ S ₂	124
II-7. Raman spectra of β -Ga ₂ Se ₂	126
II-8. Stokes Raman spectra of β -In ₂ Se ₂	131 & 132
II-9. Spectra of β -In ₂ Se ₂ with $L = 14781 \text{ cm}^{-1}$	134
II-10. Linear chain model	137
II-11. Atomic distances and valence force constants of β -In ₂ Se ₂	144
F-1. Example of a spectrum and its deconvolution ...	202

LIST OF TABLES

<u>TABLE</u>	<u>PAGE</u>
I-1. Plasma lines of the Kr ion laser	32
I-2. Power of the lasing lines of the Kr ⁺ laser	37
I-3. Optically active irreducible representations of O_h	44
I-4. Covalency parameters (k,k') that fit the experimental results	88
II-1. Vibrational modes of β -Ga ₂ S ₂ and β -Ga ₂ Se ₂	127
II-2. Comparison of our results with the linear chain model for β -In ₂ Se ₂	138
II-3. Shear modes frequencies	141
A-I. Matrix elements of the first-order spin-orbit interaction	151
A-II. Wavefunctions of the first-order spin-orbit levels	152
A-III. Matrix elements of the second-order spin-orbit interaction	153
A-IV. Diagonalized matrix elements of Eq. A-8	155
C-I. Irreducible representations and the multiplication table of O_h	161
C-II. Matrix elements of E_θ	163
C-III. Matrix elements of E_ϵ	165

<u>TABLE</u>	<u>PAGE</u>
C-IV. Symmetrized wavefunctions of the coupling between an E_g and a Γ_{8g}	167
C-V. Matrix elements of T_ξ	168
C-VI. Matrix elements of T_η	170
C-VII. Matrix elements of T_ζ	172
C-VIII. Symmetrized wavefunctions of the coupling between a T_{2g} and a Γ_{8g}	174
E-Ia) Character table of D_{3h}	191
E-Ib) Reducible character of atom motion in the primitive cell	192
E-II. Notation	193
E-III. Space and point groups of $\beta\text{-In}_2\text{Se}_2$ and its optical activity	197
F-I. Convolution parameters (a) and intensity ratio (b)	200

TABLE OF CONTENTS

	<u>PAGE</u>
STATEMENT OF ORIGINALITY	i
ABSTRACT	ii
ACKNOWLEDGEMENTS	iv
GLOSSARY	v
LIST OF FIGURES	ix
LIST OF TABLES	xi
GENERAL INTRODUCTION	1
PART I: ELECTRONIC RAMAN SPECTROSCOPY OF $MgO:Co^{2+}$	
INTRODUCTION	5
CHAPTER I - THEORY	7
I.1 Electronic Raman	7
1.1 Principles of Raman Scattering	7
1.2 Probability of Transition	10
I.2 Perturbations on the Free Ion	11
CHAPTER II - EXPERIMENTAL SET-UP	20
II.1 Apparatus	20
II.2 Details on Sources and Targets	24
CHAPTER III - RESULTS AND ANALYSIS	41
III. 1.1 Samples Information	41
III. 1.2 Orientation and Polarization	43
III. 2. Presentation and Interpretation of the Data	50

	<u>PAGE</u>
2.1 Comparison of Traces	50
2.2 Temperature Measurements	50
2.3 Identification of the Peaks	75
III. 3. Results of Calculations	85
3.1 Spin-Orbit Interaction	85
3.2 Comparison with our Data	86
3.3 Dynamic Jahn-Teller Interaction ..	87
III. 4. Uniaxial Stress and Other Treatments ..	92
III. 5. Other Systems Studied	93
III. 6. Discussion	95
CHAPTER IV - CONCLUSION	101
PART II: VIBRATIONAL RAMAN SPECTROSCOPY OF β -In ₂ Se ₂	
INTRODUCTION	104
CHAPTER I - THEORY	105
1.1 Probability of Transition	105
1.2 Crystal Structure of the In ₂ Se ₂ Polytypes ..	107
1.3 Group Theory of the Phonon Modes	111
CHAPTER II - RESULTS AND ANALYSIS	119
II.1 Information on the Samples	119
II.2 Comparison with Equivalent Systems	122
II.3 Linear Chain Model	135
3.1 Calculations of Belenkii	135
3.2 Force Constants Calculations	140

	<u>PAGE</u>
CHAPTER III - CONCLUSION	145
APPENDIX A - Spin Orbit Interaction	147
APPENDIX B - Second-Order Correction to Spin-Orbit	156
APPENDIX C - Dynamical Jahn-Teller Interaction	157
APPENDIX D - Force Constants of β -In ₂ Se ₂	175
APPENDIX E - Group Theory	179
APPENDIX F - Method of Deconvolution	199
REFERENCES	203

RAMAN SPECTROSCOPY
OF Co^{2+} IN MgO AND
OF $\beta\text{-In}_2\text{Se}_2$

GENERAL INTRODUCTION

Dr. C.V. Raman and his collaborators [1] in 1928 observed the scattering of filtered sunlight by a liquid and, with the incident wavelength blocked out by a complementary filter, saw some additional wavelengths. Then, using a mercury arc lamp, a spectrograph and a photographic plate, they obtained the scattering spectrum for some gases, liquids and solids. They showed that the frequency shifts were independent of the exciting frequency and were characteristic of the substance investigated: Raman spectroscopy was born.

In the years that followed, this method was used (mainly by chemists) to probe the modes of rotation and vibration of molecules in liquids and in gases, that are transparent to the exciting wavelengths of the mercury arc. From 1940, the observation of the normal modes of vibration of crystals became possible with the availability of good quality monocrystals and better instrumentation. The use of lattice dynamics [2] and group theory [3,4] permitted a better interpretation of the Raman spectra. With the invention of the laser (~ 1960) which gives an intense monochromatic beam of light, the field of Raman spectroscopy expanded enormously; nowadays, this tool is used by biochemists, chemists and even physicists.

Researchers in Solid State use Raman spectroscopy to look at one phonon [5,6] and two-phonon [7,8] spectra and many kinds of excitations like polaritons [9], plasmons [10,11] and magnons [12,13]; they even observed electronic transitions

from donors and acceptors in semiconductors [14-16]. But few have looked at electronic transitions within the ground state of deep impurities in insulators [17-19].

The divalent cobalt ion (Co^{2+}) in a cubic crystal, like magnesium oxide (MgO), has a threefold ground orbital state and is expected to be Jahn-Teller active [20]. The Raman spectra of this system by others is inaccurate [21] and inconsistent with theory [22,23]. Part I of this thesis is concerned with the Raman study of $\text{MgO}:\text{Co}^{2+}$. In the first chapter, the general principle of the Raman effect is explained with some notions of the selection rules for electronic transitions; we also present the different perturbations applied on the cobalt ion. Chapter II presents the experimental set-up used for this system and for In_2Se_2 (Part II). Chapter III gives the experimental results and its interpretation with the aid of theoretical calculations, detailed in Appendices A, B and C; this chapter terminates with a discussion of our results with respect to the literature.

Vibrational Raman spectroscopy was applied primarily to the study of three dimensional crystals but recently some work was done on layer structure compounds [23-26]. Upon the request of Dr. S. Jandl, Université de Sherbrooke, we investigated the spectra of indium selenide (In_2Se_2) at low temperature with the red lines of the Kr^+ laser; this work is included in Part II. The first chapter of this part presents the

probability for vibrational Raman scattering and the selection rules based on the symmetries of the layer structure of the different polytypes. Chapter II gives the correlation between similar systems and our experimental results. We also compare these to the frequencies calculated by Belenkii et al [66] from the linear chain model (LCM); using the same model, we calculated the force constants for the shear modes.

The Appendices present the calculations of the first- and second-order spin-orbit interaction (A), the $\Gamma_{8g}^1 + \Gamma_{8g}^2$ spin-orbit correction (B) and the dynamical Jahn-Teller interaction (C). The force constants for $\beta\text{-In}_2\text{Se}_2$ in the LCM approximation are calculated in Appendix D; the pertinent information and the usual notation of group theory are included in Appendix E. Appendix F explains the method of deconvolution used for the analysis of the temperature data.

PART I

ELECTRONIC RAMAN
SPECTROSCOPY OF
/ MgO:Co²⁺

INTRODUCTION

The degenerate (non-Kramers) electronic ground state of an impurity ion in a crystal is unstable with respect to some asymmetric nuclear displacement and will undergo a static distortion to a new configuration of minimum energy (lower symmetry), if the coupling between the electrons and such displacements is stronger than the zero-point energy of the associated vibrational mode. But if the zero-point vibrational energy is comparable with the energy barrier separating equivalent configurations, the complex exhibits a coupled motion of the electrons and the vibrational mode; this latter situation is referred to as the dynamical Jahn-Teller effect [73,74,95].

This important effect explains the short spin-lattice relaxation times observed for some transition metal ions at an octahedral site [87,88]. Phase transitions in some rare-earth compounds have been driven by the lattice distortions associated with the Jahn-Teller ions [89,94]. The Jahn-Teller effect is also responsible for the tunability of some solid state lasers [91,92].

The preceding applications result from an understanding of the corresponding Jahn-Teller ion as an isolated entity in a crystal matrix. One of the possible candidates is divalent cobalt in MgO for which the spin-orbit energy levels

of the ground ${}^4T_{1g}$ state were not measured. Raman spectroscopy can determine these levels while the use of very dilute samples ($\text{Co}^{2+} \lesssim 100$ ppm) will guarantee that we will observe the electronic levels characteristic of the isolated ion and so the exact concentration is not crucial.

Most of the reports on $\text{MgO}:\text{Co}^{2+}$ observed the levels of the excited ${}^4T_{2g}$ and ${}^4A_{1g}$ by absorption and luminescence spectroscopy [32,51,57]. Using the only experimental result available at the time (from magnetic susceptibility data of $\text{MgO}:\text{Co}^{2+}$ which was capable of giving the first excited Γ_{8g} level [49]), Ray and Regnard [33] calculated the corresponding Γ_{8g} level using the dynamical Jahn-Teller model with coupling to E_g vibrational modes only. Since Raman measurements are capable of observing all the energy levels of the ${}^4T_{1g}$ state, we were in a position to check Ray's assumption that the coupling to the T_{2g} mode is not important. Guha [23] during the course of our work surmised that a Raman line, which he observed in Co^{2+} doped MgO at 935.7 cm^{-1} (at 18°K), must be due to an electronic transition to the second excited Γ_{8g} state, although he mistook the transition to the first excited Γ_{8g} state for a vibrational transition.

CHAPTER I - THEORY

I. 1 - Electronic Raman

I. 1.1 - Principles of Raman Scattering

The phenomenon of light scattering [4] can be explained by the following general principles. An electron in an initial state (Fig. I-1) makes a transition (electric dipole) to one of many excited states by absorbing an incident photon (ω_i, \vec{q}_i); then the electron makes a transition from that intermediate state to a final state by emitting a photon (ω_s, \vec{q}_s). The energy is not conserved for each step taken separately but for the over-all process it is conserved:

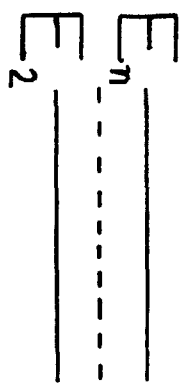
$$\hbar\omega_i = \hbar\omega_s \pm \hbar\Omega \quad (I-1)$$

where $\hbar\Omega$ is the energy of the excitation created (+) or destroyed (-) in the process (in Fig. I-1, $\hbar\Omega = E_1 - E_0$).

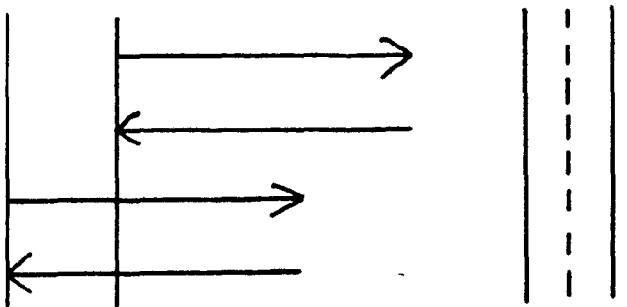
If the final state is the initial state, we have Rayleigh scattering; if they are different, we have Raman scattering. If the initial state is higher than the final state (Fig. I-1a), the energy of the scattered photon includes the energy of the destroyed excitation: it is the anti-Stokes spectrum. If the order of the states is reversed (Fig. I-1c), the scattered photon is less energetic than the incident photon and an excitation is created: it is the Stokes spectrum. In most cases, the initial state of the electron for the Stokes process is the ground state, but for the anti-Stokes, it is an excited state and is dependent on the temperature. If the energy difference between the initial and the intermediate states is equal to the

Fig. I-1. Raman and Rayleigh scattering. The unshifted Rayleigh peak ($\bar{\nu}$; b) is a million times more intense than either the anti-Stokes peak (a), upshifted in frequency ($+\bar{\nu}_0$), or the Stokes peak (c), downshifted in frequency ($-\bar{\nu}_0$); the shifts are usually measured in cm^{-1} (wavenumber).

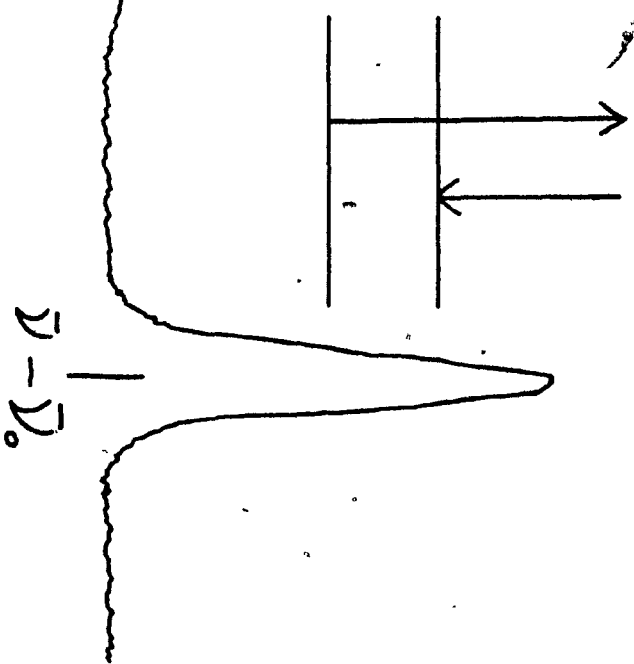
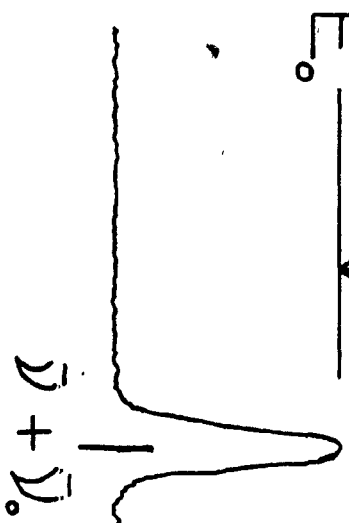
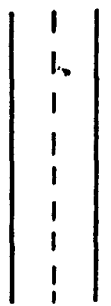
(a)



(b)



(c)



energy of the incident photon, we have a resonant Raman spectrum; for both systems studied here, we worked outside that regime.

I. 1.2 - Probability of Transition

The probability of Raman scattering by electronic states is derived by Loudon [4] from the theory of atomic Raman scattering of Heitler [27] and is proportional to the following expression:

$$\left| \sum_j \left[\frac{\vec{e}_0 \cdot \vec{p}_{ij} \vec{e}_s \cdot \vec{p}_{jf}}{E_j - E_i - \pi\omega_0} + \frac{\vec{e}_s \cdot \vec{p}_{ij} \vec{e}_0 \cdot \vec{p}_{jf}}{E_j - E_i + \pi\omega_s} \right] \right|^2 \quad (\text{I-2})$$

The first term in the square bracket takes care of the process where an incident photon of polarization \vec{e}_0 and energy $\pi\omega_0$ is absorbed first by an electron making an electric dipole transition (\vec{p}) from an initial (i) to an intermediate (j) state and then returning by an electric dipole transition to a final state (f) by emitting a photon of polarization \vec{e}_s and energy $\pi\omega_s$. The second term is related to the process where the scattered photon is emitted, before the incident photon is absorbed; the first term dominates the probability.

The selection rules depend on the symmetries of the initial and final states; for an ion situated at a center of inversion, these states must have the same parity and, if the temperature is low enough, the initial state is the electronic ground state. The intermediate states have to be of opposite parity to the initial state for the transitions to take place by electric

dipole; higher-order multipole transitions contribute less, outside the resonance regime. Some Raman transitions could be weak or absent even if they are group theoretically allowed.

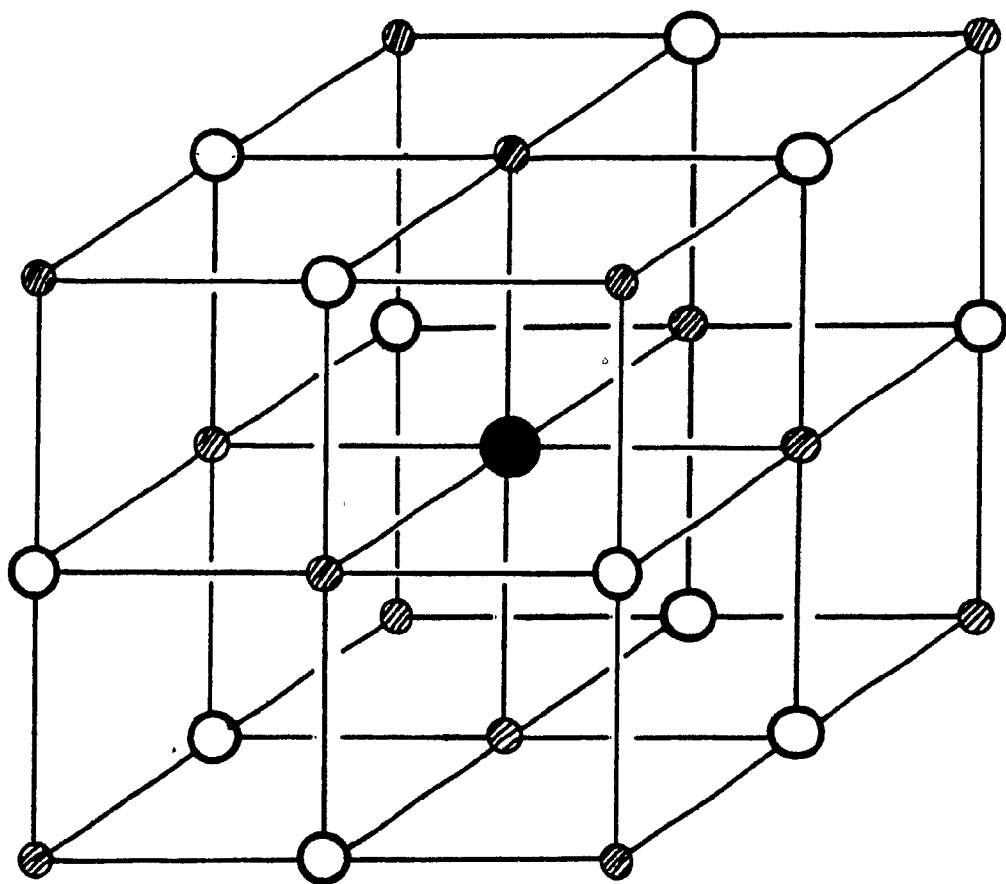
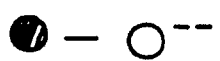
I. 2. - Perturbations on the Free Ion

The free divalent cobalt ion, which has two s electrons removed, has seven electrons in its 3d-shell; using Russell-Saunders coupling scheme and Hund's rules [28] its ground term, is a 4F . The Co^{2+} ion is an isoelectronic impurity when it enters substitutionally at the magnesium site in MgO (Fig. I-2). This compound being a large gap ($\sim 8eV$)[29] insulator, the impurity is deep in the gap and its electronic wavefunctions are localized [30]. The ion behaving as a nearly free ion is subjected mainly to the electrostatic interaction of the nearby oxygen atoms (molecular cluster model). MgO crystallizes in the $O_h^5(Fm3m)$ space group with the NaCl structure and the electric potential of the octahedron of the nearest neighbour oxygen ions on the cobalt ion is [31]:

$$V_{CF} = \frac{35e}{4a_0^5} (x^4 + y^4 + z^4 - \frac{3}{5}r^4) \quad (I-3)$$

with e the electronic charge and a_0 the distance between the impurity and the oxygen ions. The influence of the potential, in the intermediate crystal field scheme, will split the F term ($L = 3$) into a ground $^4T_{1g}(3)$ and excited $^4T_{2g}(3)$ and $^4A_{2g}(1)$ states (Fig. I-3); the orbital degeneracy of each state is given in parenthesis beside their irreducible representations (i.r.).

Fig. I-2. Cobalt impurity site in MgO. The cobalt ion is at the center of the octahedron formed by the nearest-neighbour oxygens. The space group is in the Schoenflies notation with the International symbol in parenthesis.



Space group: O_h^5 (Fm3m)

Crystal structure: NaCl

Fig. 1-3. Energy levels of Co^{2+} in MgO .

In the left we present the low lying terms of the free divalent cobalt ion ($^4\text{P} \sim 14,550 \text{ cm}^{-1}$; $^2\text{G} \sim 16400$); the higher terms (not shown) are at 22000 cm^{-1} (^2H , ^2P and ^2D) and at 35000 cm^{-1} (^2F) [32]. The octahedral crystal field splits and shifts the three lowest terms into different states labelled by their irreducible representation (i.r.) in O_h . The rest of the figure concerns only the interactions (spin-orbit and Jahn-Teller) acting on the ground $^4\text{T}_{1g}$ state (the subscript g is dropped for clarity).

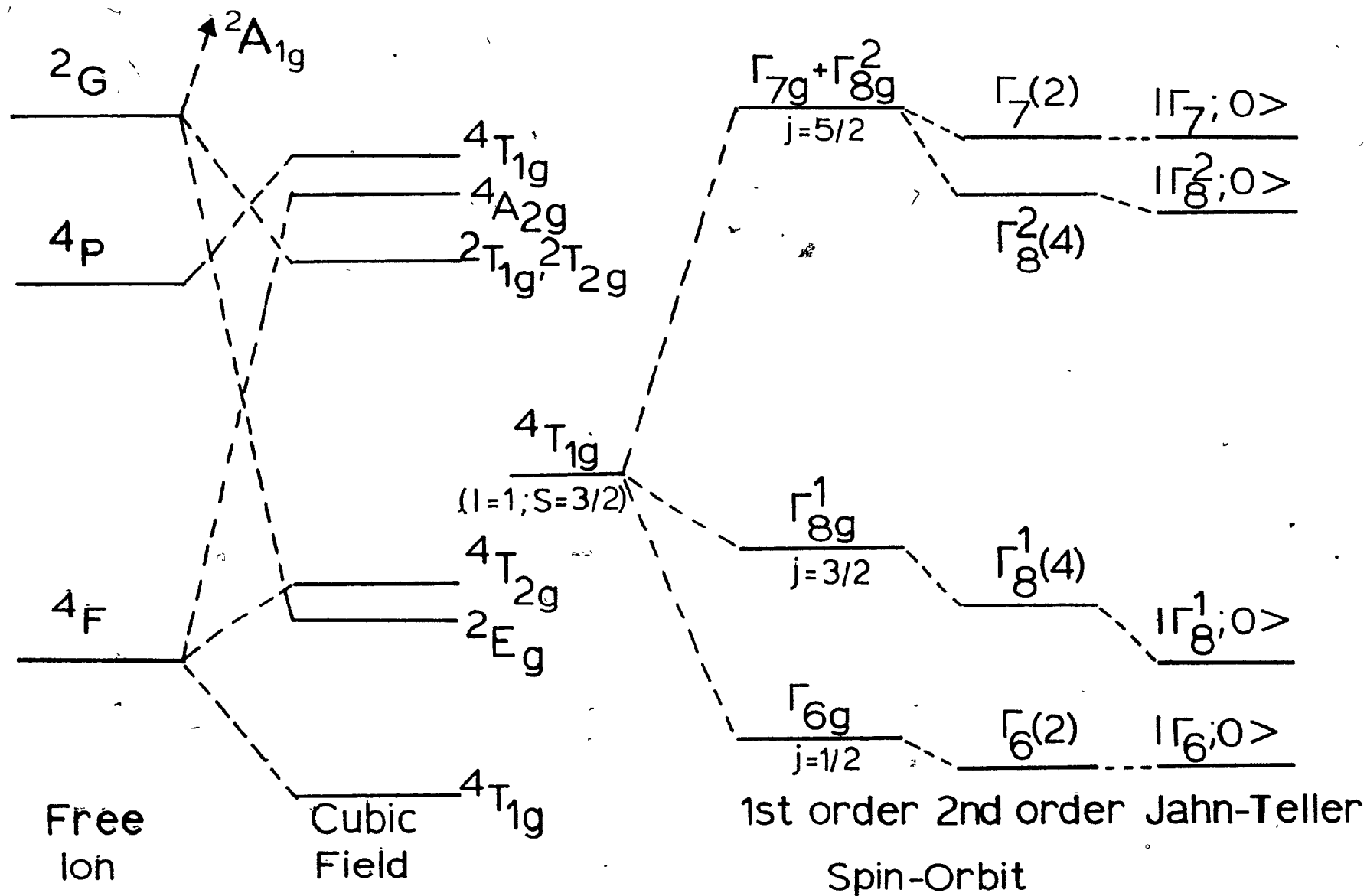


Fig I-3

The ground triplet state ${}^4T_{1g}$ is behaving as if it had an effective orbital angular momentum of $\vec{l} = 1$. The energy separation between the first two states is approximately 8000 cm^{-1} (Δ) [32] which is of the same order of magnitude as the term separation ($11,000 \text{ cm}^{-1}$) and justifies the use of the intermediate crystal field scheme; this means that \vec{L} and \vec{S} are good quantum numbers but that \vec{J} will not be.

Next, in order of lesser importance, is the spin-orbit interaction up to second-order [33]:

$$H_{SO} = \lambda'(\vec{l} \cdot \vec{S}) + \frac{15}{4\Delta} \lambda^2 [(\vec{l} \cdot \vec{S})^2 - 2(\ell_x^2 S_x^2 + \ell_y^2 S_y^2 + \ell_z^2 S_z^2)] \quad (\text{I-4})$$

where λ' and λ are the effective first- and second- order spin-orbit coupling parameters. The first-order term splits the ${}^4T_{1g}$ ground state into effective j values of $1/2$, $3/2$ and $5/2$ (Fig. I-3), the degeneracy of the higher level being partially removed by the second-order term. The total angular momentum \vec{J} not being a good quantum number, equation I-4 is transformed to give for the first-order term:

$$H_{SO}^{(1)} = \lambda' [\ell_z S_z + \frac{1}{2} (\ell_+ S_- + \ell_- S_+)] \quad (\text{I-5a})$$

and for the second-order term:

$$H_{SO}^{(2)} = - \frac{15\lambda^2}{4\Delta} \left\{ \ell_z^2 S_z^2 + \frac{1}{4} [(\ell_+^2 S_+^2 + \ell_-^2 S_-^2) + (\ell_+ \ell_- S_+ S_- + \ell_- \ell_+ S_- S_+)] \right. \\ \left. - \frac{1}{2} [\ell_z S_z (\ell_+ S_- + \ell_- S_+) + (\ell_+ S_- + \ell_- S_+) \ell_z S_z] \right\} \quad (\text{I-5b})$$

with the operators A_{\pm} defined as $A_{\pm} = A_x \pm iA_y$ ($A = \ell$ or S) being the raising (+) and lowering (-) operators. For the ${}^4T_{1g}$, the spin-orbit coupling parameters are related to the free ion value λ_0 (-180 cm^{-1} for Co^{2+}) by the following expressions:

$$\lambda' = -\frac{3}{2} ak\lambda_0 \quad (\text{I-6a})$$

$$\lambda^2 = akk'\lambda_0^2 \quad (\text{I-6b})$$

The covalency parameters $k({}^4T_{1g})$ and $k'({}^4T_{2g})$ reduce the orbital angular momentum and so does also the parameter "a" which takes account of the configuration mixing between the ${}^4T_{1g}$ of 4F and the ${}^4T_{1g}$ of 4P . The conditions on the parameters are:

$$0 < k' \leq k \leq 1 \quad \text{and} \quad 0 < a \leq 1 \quad (\text{I-6c})$$

and they take their maximum values when there is no reduction. The wavefunctions which diagonalize the spin-orbit energy matrix to second-order are presented in Appendix A (Table A-IIa and Eq. A-8).

The electronic levels of the cobalt ion having a degeneracy higher than two, can interact with degenerate vibrations of the cluster formed by the octahedron of nearest neighbour oxygens. If the electron-phonon interaction does not reduce the site symmetry we are in the dynamical Jahn-Teller regime. The corresponding levels are now vibronic (part electronic,

part phonon) and will be shifted to a lower energy.

The only modes of vibration of the cluster which can couple to a T_{1g} orbital triplet are the E_g and T_{2g} modes. The corresponding Hamiltonian of the electron-phonon interaction, in the approximation of the molecular cluster model, is [34]:

$$H_{jt} = V_e(Q_\theta E_\theta + Q_\epsilon E_\epsilon) + V_t(Q_\xi T_\xi + Q_\eta T_\eta + Q_\zeta T_\zeta) \quad (I-7)$$

V_e and V_t are the coupling parameters of the electronic orbitals with the corresponding modes of vibration; the Q_α is the displacement operator of the modes with $\alpha = \theta, \epsilon$ for the partners of the doublet E_g mode of frequency ω_e and $\alpha = \xi, \eta, \zeta$ for those of the triplet T_{2g} mode of frequency ω_t . The displacement operator is defined as:

$$Q_\alpha = \left(\frac{\pi}{2\mu\omega_\alpha}\right)^{1/2} (b_\alpha^+ + b_\alpha) \quad (I-8a)$$

where μ is the mass of the ligand oxygen ion and ω_α is the frequency of the modes; for the partners of a mode, this frequency is the same. Applying the creation (b^+) and annihilation (b) operators on the occupation number state $|n\rangle$, we have:

$$b^+ |n\rangle = (n+1)^{1/2} |n+1\rangle \quad (I-8b)$$

$$b |n\rangle = (n)^{1/2} |n-1\rangle \quad (I-8c)$$

The electronic orbital operators E_α and T_β ($\alpha \neq \beta$) may be

given in terms of the orbital angular momentum operators L_{\pm} and L_z , with $\vec{L} = -\frac{3\hbar}{2}\vec{e}_z$, as [35]:

$$E_{\theta} = \frac{1}{2}(3L_z^2 - L^2) \quad (\text{I-9a})$$

$$E_{\epsilon} = \frac{\sqrt{3}}{4}(L_+^2 + L_-^2) \quad (\text{I-9b})$$

for the E_g mode coupling and as:

$$T_{\xi} = -\frac{i}{2}[(L_+L_z + L_zL_+) - (L_-L_z + L_zL_-)] \quad (\text{I-10a})$$

$$T_{\eta} = \frac{1}{2}[(L_+L_z + L_zL_+) + (L_-L_z + L_zL_-)] \quad (\text{I-10b})$$

$$T_{\zeta} = -\frac{i}{2}[L_+^2 - L_-^2] \quad (\text{I-10c})$$

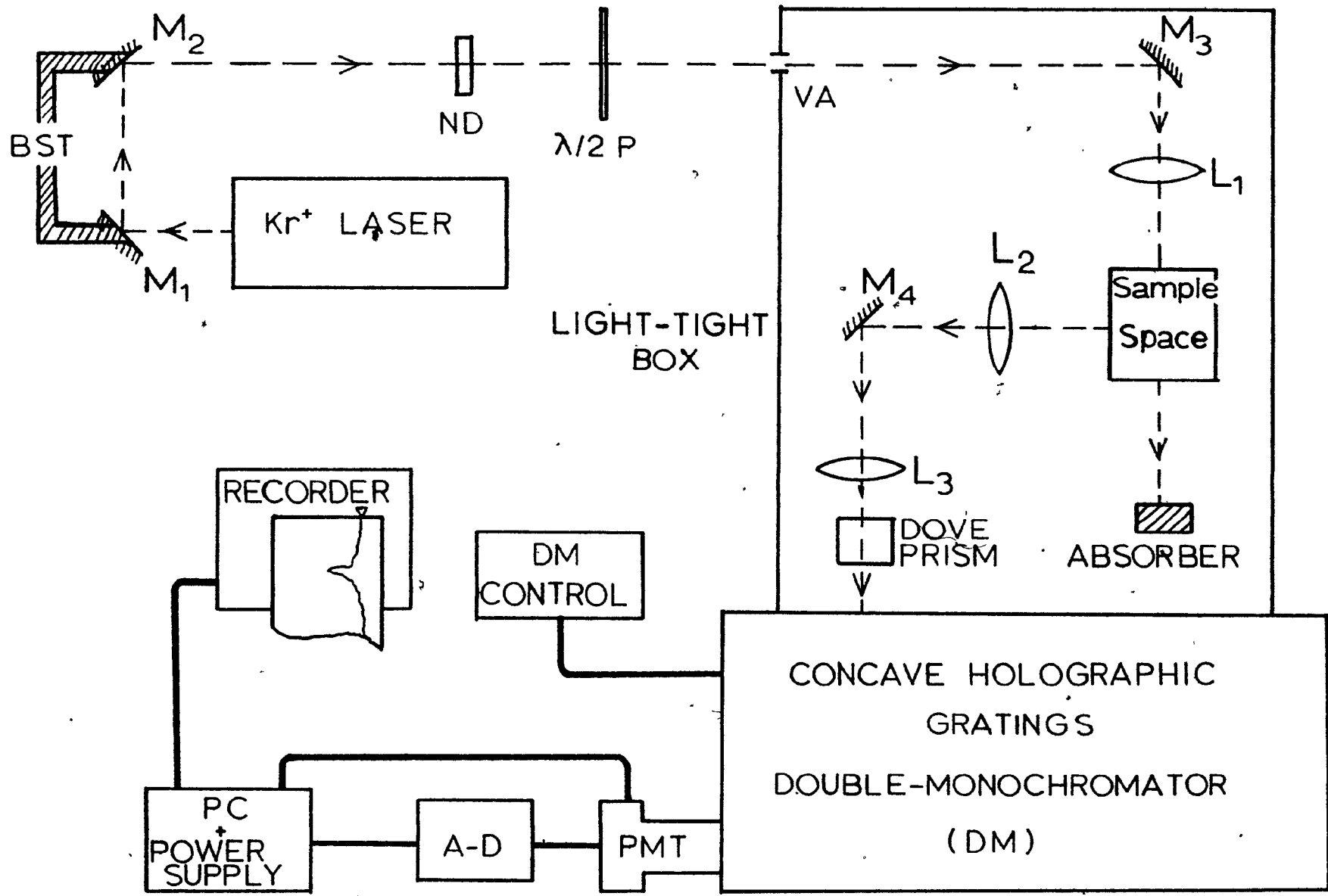
for the T_{2g} mode coupling. The matrix elements of these operators and the corresponding Jahn-Teller shifts are given in Appendix C.

CHAPTER II - EXPERIMENTAL SET-UPII. 1 - Apparatus

All the light from the Spectra Physics (Model 270) krypton ion laser (see Fig. I-4) is directed by a Newport beam steerer ($M_1 + M_2 = \text{BST}$) and traverses a long path in the air permitting diffusion of the plasma light which is greatly reduced when the laser beam passes through the variable aperture (VA) at the entrance of the light-tight box (background reducer); the laser works in the TEM_{00} mode. Before going through the diaphragm, the laser beam intensity can be reduced by neutral density filters (ND) and its polarization can be rotated by a half-wave plate ($\lambda/2 \text{ P}$). After entering the box, the beam is deflected by a plane mirror (M_3) that can rotate vertically and horizontally (Newport gimbal) and thus permits positioning of the beam on (or in) the sample; the mirror can also be displaced parallel to the incident beam (Ealing transverse slide) and thus permitting different scattering configurations. Then, the beam goes through a spherical focusing lens (L_1) that can be displaced along the beam direction; it can also be moved up and down (Ealing vertical slide) to adjust the horizontality of the beam in a transparent sample. In the 90° grazing incidence configuration (see Fig. II-5 in part II) a cylindrical lens (at L_1) gives a vertical image of the laser to minimize the heating effect on the sample of indium selenide. The laser beam after leaving the sample space is absorbed by a black cloth.

The scattered light is collected by a Cinelux 75mm f/1.6

Fig. I-4. Experimental set-up. The designation of the components is given in the text and the sample space is shown in Fig. I-5.



lens (L_2) which can be translated and rotated, vertically and horizontally by a Newport Corporation gimbal. Mirror M_4 is inserted in a small gimbal and directs the scattered beam through a spherical focusing lens (L_3). The Jobin-Yvon Ramanor HG2S double-monochromator (DM) has horizontal slits and a Dove prism was inserted between L_3 and the entrance slit of the DM for the experiment on In_2Se_2 . All the plane mirrors used are of the multilayer dielectric type.

The scattered light, after being dispersed by the concave holographic gratings of the DM, is detected by a Hamamatsu (R666S) photomultiplier tube (PMT) having a gallium arsenide photocathode; the PMT is enclosed in a radio frequency protected housing (Products for Research TE-177-RF) and thermoelectrically cooled. The electric pulses are amplified (PAR 1120 Amplifier-Discriminator) and counted; an analog output from the photon counter (PC) (PAR 1105) is fed to a Gould thermal chart recorder (Brush 110); the PAR-PC also gives the high-voltage necessary for the operation of the PMT.

The sample space structure is shown in Fig. I-5 and the base of the Janis Vari-Temp dewar (model DT) is clamped to reduce vibrations. The uniaxial stress system is presented in Fig. I-6a and was used on the $\text{MgO}:\text{Co}^{2+}$ samples; the calibration curve for the piezoelectric transducer is given in Fig. I-6b.

I participated in the assembly and the installation of the Raman system and supervised the construction of the uniaxial stress system; we also built a level detector for the helium reservoir of the Dewar.

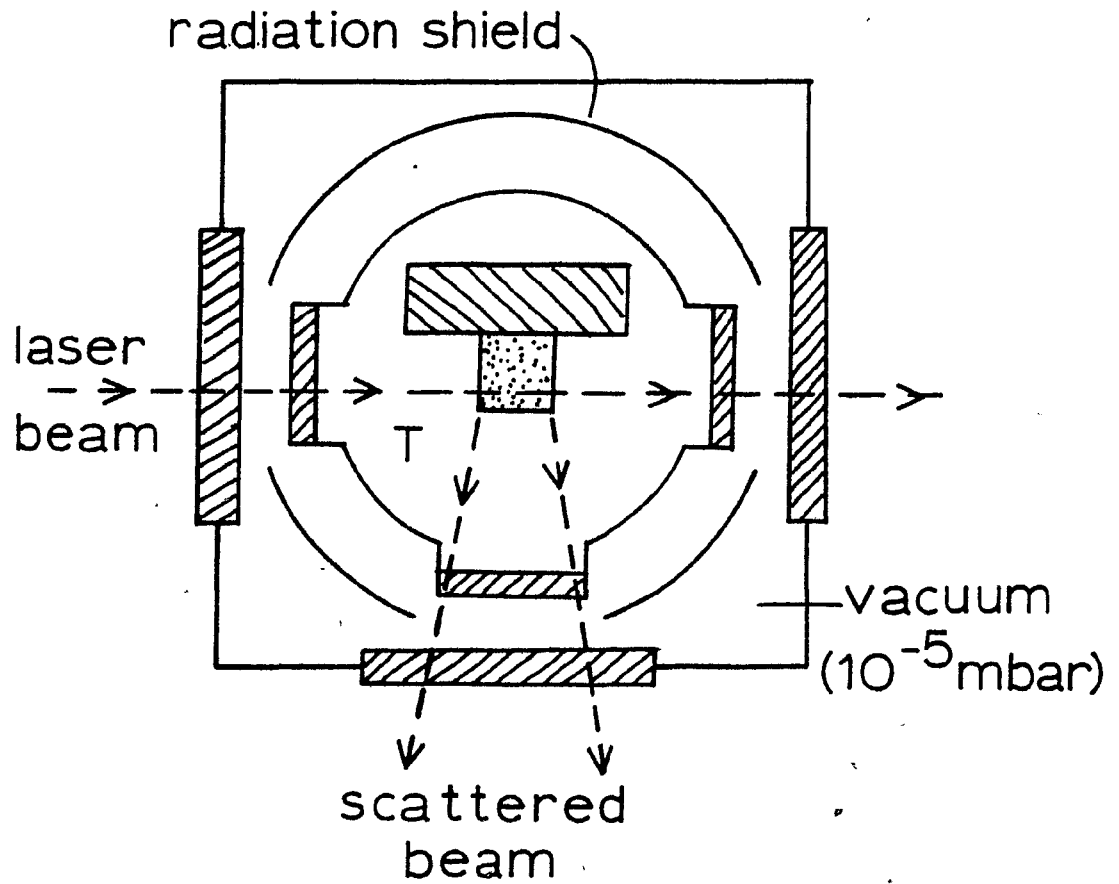
II. 2 - Details on Sources and Targets

The cobalt in the magnesium oxide samples gives them a rosy tint [50], but they are still transparent; the direct energy gap of magnesium oxide at 85°K is 7.833eV ($63,180 \text{ cm}^{-1}$) [36]. All the wavelengths available from the krypton ion laser could be used but the scattering being proportional to the fourth power of the incident frequency [4] we used the lines in the blue-green region: 530.9 nm (18836 cm^{-1}), 520.8 (19195), 482.5 (20717), and 476.2 (20991); the spectra using this last laser line have two plasma lines hiding the 300 cm^{-1} structure and the best spectra were obtained with the 18836 cm^{-1} laser line.

The indium selenide samples (part II) are metallic-like in appearance and translucent red for very thin sheets; its direct gap at room temperature is 1.187 eV (9573 cm^{-1}) [37]. We used the grazing incidence with the observation of

Fig. I-5. Sample space.

We are showing the 90° scattering configuration for the $\text{MgO}:\text{Co}^{2+}$ samples: these samples were in helium gas and the temperature (T) was near 10°K . For the experiment of part II ($\beta\text{-In}_2\text{Se}_2$) the samples were in superfluid helium and T was near 2°K . (figure not to scale)



-  sample
-  windows(Suprasil)
-  copper holder

Fig. I-6(a). Uniaxial pressure system.

The top part is at room temperature while the bottom part is near the liquid helium temperature ($\sim 5^\circ\text{K}$). The pressure from a nitrogen bottle is applied to the piston (Alkon D24) and is transmitted by a rod to the uniformisation cylinder and the top hammer. The pressure is measured by the piezoelectric transducer (Sundstrand, Kistler 601B1); its charge signal is amplified (Kistler 504E) and displayed on a voltmeter (Keithley 177) (the system is not drawn to scale).

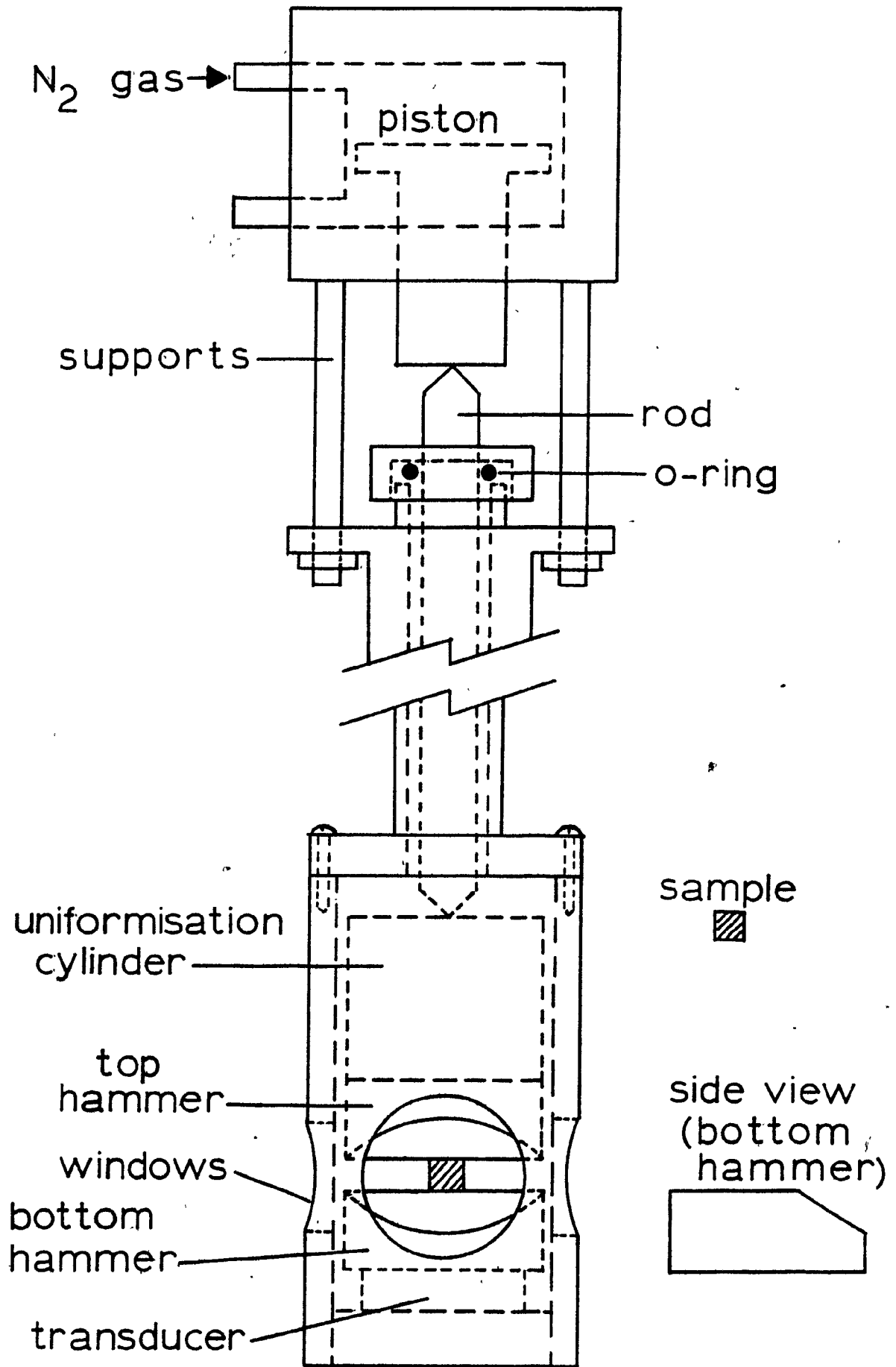


Fig. I-6.(b) Calibration of Pressure Transducer. The calibration was recorded with the transducer immersed in liquid He below the λ point. The slope calculated from linear regression is 9.36 PSI/V. The insert indicates the internal resistance of the system at low pressure (less than 15 PSI). The conversion of the pressure in most common units is

$$P \text{ (kgf/mm}^2\text{)} = .1.091 \frac{P_o \text{ (PSI)}}{A \text{ (mm}^2\text{)}}$$

with A the contact area of the sample with the hammer.

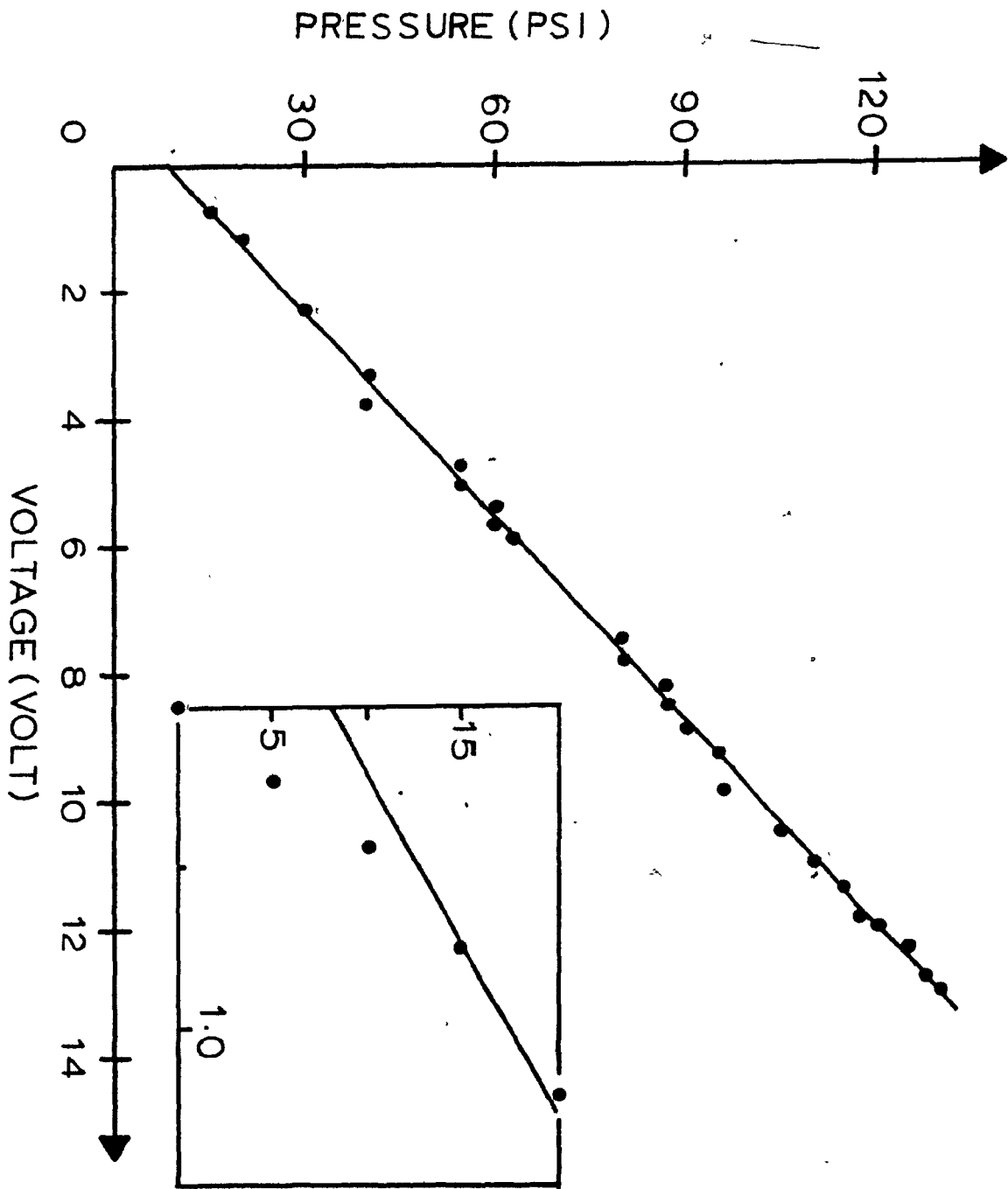


Fig 10

the scattered light at 90° from the crystal layers. The following Kr^+ laser lines were used: 752.5nm (13292 cm^{-1}), 674.4 (14781) and 647.1 (15451) with this last line giving the best spectra.

Despite the background reducer and because our system is very sensitive, some spectra showed some of the Rayleigh scattered lines of the laser plasmas. To identify these lines, a spectrum of the scattered light from a sample of indium selenide (grazing incidence) was made at room temperature with the laser current below the lasing threshold for all the lines (16 Amp). In table I-1 are the wave numbers of these plasma lines with their shift from the nearest preceding lasing line. Table I-2 gives the power range of the lasing lines according to the D.C. current in the laser tube.

The intensities of the plasma lines in the different spectrum of the samples is dependant on many factors. The most important is the quality of the sample: the presence of microbubbles in a transparent sample, the stair-like structures on the cleaved faces, the polished surfaces. For the SB samples ($\text{MgO}:\text{Co}^{2+}$) most of the background noise comes from the scattering of the laser beam at the entrance and exit faces of the crystal. Its contribution is reduced if the dimension of the sample along the beam is such that its image at the entrance slit of the spectrometer covers

Table I-1. Plasma lines of our Kr ion laser. The laser was below lasing threshold (16A) and the scattering surface was a sample of indium selenide at room temperature (the power of the lines is too small to produce Raman lines for this sample). In the first column we have the normal lasing lines; in the second column are the peaks seen in the spectrum and in the third column we give the separation ($\Delta\bar{\nu}$) from the nearest highest usually lasing line (scan: $20 \text{ cm}^{-1}/\text{min}$; time constant 4.7 sec; error: $\pm 2 \text{ cm}^{-1}$). No spectrum was taken between 17500 and 15460 cm^{-1} .

TABLE I-1

Laser (cm^{-1})	Plasma (cm^{-1})	$\Delta\nu$ (cm^{-1})
21360	21332	28
	310	50
	295	65
	274	86
	095	265
	039	321
	008	352
	20991	369
20991	20976	15
	946	45
	876	115
	844	147
	776	215
	717	274
20717	20688	29
	671	46
	661	56
	626	91
	603	114
	582	135
	528	189
	366	351
	341	376
	336	381
	213	504
	204	513
	155	562
	080	637

TABLE I-1 (Cont'd)

Laser (cm^{-1})	Plasma (cm^{-1})	$\Delta\bar{\nu}$ (cm^{-1})
20717	20064	657
	000	717
	19941	776
	904	813
	882	835
	872	845
	860	857
	811	906
	779	938
	735	982
	729	988
	708	1009
	690	1027
	670	1047
	654	1063
	513	1204
	503	1214
	437	1280
	348	1369
	307	1410
273	1444	
224	1493	
195	1522	
19195	19160	35
	134	61
	116	79
	058	137
	017	178
	18966	229

TABLE I-1 (Cont'd)

Laser (cm^{-1})	Plasma (cm^{-1})	$\Delta\bar{\nu}$ (cm^{-1})
19195	18946	249
	908	287
	836	359
18836	18802	34
	784	52
	760	76
	746	90
	699	137
	669	167
	603	233
	452	384
	383	453
	366	470
	356	480
	283	553
	256	580
	208	628
	180	656
	102	734
	072	764
	036	800
026	810	
004	832	
	17974	862
	966	870
	954	882
	948	888
	916	920

TABLE I-1 (Cont'd)

Laser (cm^{-1})	Plasma (cm^{-1})	$\Delta\bar{\nu}$ (cm^{-1})
18836	17750	1086
	694	1142
	624	1212
	619	1217
	597	1239
	571	1265
	557	1279
15451	541	1322
	15355	96
	216	235
14781	138	313
	14781	672
	14766	15
14781	675	106
	551	230
	480	301
	398	383

Table I-2. Typical power of the krypton ion laser. These values were true at the time of the installment of the recent tube (13/11/80). The power rating for a certain line will be obtained at a higher discharge current as the tube ages (maximum current 49A); the power is not a linear function of the current.

TABLE I-2

LASER(cm^{-1})	POWER(mW)	CURRENT(A)
21360	125	45
20991	170-400	35-45
20717	220-420	35-45
19195	780	45
18836	280-1750	35-45
15451	760-2100	25-35
14781	400-920	25-35

more than the slit length (sample S4B); for these samples the bulk scattering is so weak that the laser beam cannot be seen going through it. Some spectra were done with a spectral filter (Anaspec 300S) of 20 cm^{-1} band width in front of the laser and thus eliminated the plasma lines (laser power reduced by $\sim 20\%$).

During the experiment on magnesium oxide, the sample space was continuously fed a new supply of helium gas ($\sim 5^\circ\text{K}$) by slow pumping; the temperature was monitored by a silicon diode (Lake Shore Cryotronics) in contact with the copper support of the sample. No temperature measurements were made when the sample was under uniaxial pressure.

The samples of indium selenide (part II) were immersed in liquid helium at reduced pressure; the temperature in the sample space was below 2°K (superfluid helium) but the sample scattering face was closer to 100°K . This measurement was found from the ratio of the anti-Stokes (as) to the Stokes (s) intensities of the $\bar{\nu}_0 = 42 \text{ cm}^{-1}$ Raman peak (Fig. II-8). The intensities are related to the occupation number n_0 of the phonon mode (Bose-Einstein statistics) and the fourth power of the scattered frequency [75a]:

$$\frac{I_{as}}{I_s} = \left[\frac{\bar{\nu} + \bar{\nu}_0}{\bar{\nu} - \bar{\nu}_0} \right]^4 \frac{n_0 + 1}{n_0} \approx \exp(-hc\bar{\nu}_0/K_b T) \quad (\text{I-11})$$

the equation is valid when $\bar{\nu}$ does not correspond to a resonance

of the system and the approximation is sufficient when $\bar{\nu}_0 \ll \bar{\nu}$ (18836 cm^{-1}); this approximation was used to estimate the temperature (K_b is the Boltzman constant).

CHAPTER III - RESULTS AND ANALYSIS

III. 1.1 - Sample information

Pure magnesium oxide (MgO) in the crystalline form is transparent and colorless but the cobalt-doped samples (MgO:Co²⁺) have a pink coloration which is due to the presence of the cobalt ion (Co²⁺) at the magnesium site. The SB group of samples are from a crystal produced by the Oak Ridge National Lab. (USA), with 5% cobaltic oxide (Co₂O₃) in the melt. The SA samples were cut from a big monocrystal (doped with CoO) given to us by Dr. L. Chase, Department of Physics, University of Indiana (Bloomington, Ind., USA) and also grown at Oak Ridge. The color density of the latter samples is less than for the SB samples and we deduce that the cobalt concentration is also less. A sample of the SB family (larger cobalt concentration) was irradiated for one week by a low flux neutron source (²³⁸Pu-⁹Be); the nuclear spectrum of this sample did not show the characteristic gammas of ⁶⁰Co (1.17 and 1.33 MeV). Crystals cut from the same boules as our samples contain in the order of 100 ppm of Co²⁺ as evidenced by extensive EPR studies [88]; thus the Co²⁺ ions are independent particles and the exact concentration is not crucial. We are only interested in the electronic level structure of isolated cobalt ions in MgO.

The S2A, S3B, S4B and SP (pure MgO) samples were cut and cleaved along {100} faces; sample S1A was cut along

the {110} and (001) faces. The cut faces were polished using the following sequence of 3M lapping sheets: 12, 9, 3 and 1μ . The humidity in the air can degrade the quality of the faces by depositing on them a fine powder of magnesium hydroxide ($Mg(OH)_2$); some of the faces of the samples had to be repolished to correct this defect.

All the samples (doped and pure) showed around $14,200\text{ cm}^{-1}$ the luminescence lines characteristic of the presence of the chromium ion (Cr^{3+}) at the magnesium site [38].

III. 1.2 - Orientation and Polarization

The direct product of the irreducible representations (i.r.) of the initial and final states is reducible in i.r. which have basis functions that can be related to the product of the directions of the polarization of the incident and scattered light (as defined with respect to the crystallographic axes)[39]. We saw in chapter I (Fig. I-3) that the ${}^4T_{1g}$ ground state split via the spin-orbit interaction into $\Gamma_{6g}, \Gamma_{8g}^1, \Gamma_{8g}^2$ and Γ_{7g} levels, in order of increasing energy; the only transitions possible at low temperature are two $\Gamma_{6g} \rightarrow \Gamma_{8g}$ and the $\Gamma_{6g} \rightarrow \Gamma_{7g}$ and the direct product of these i.r. reduces to (Table C-I-b):

$$\Gamma_{6g} \times \Gamma_{8g} = \Gamma_{3g} + \Gamma_{4g} + \Gamma_{5g} \quad (I-12a)$$

$$\Gamma_{6g} \times \Gamma_{7g} = \Gamma_{2g} + \Gamma_{5g} \quad (I-12b)$$

We give in Table I-3, the optically active i.r. of the double point group O_h with their dimensions (or degeneracy) and their basis functions. In conjunction with this table and Fig. I-7, we see that the sample S1A with the incident light polarized horizontally (X + Y) and the scattered light polarized vertically (X - Y) should permit us to see the $\Gamma_{6g} \rightarrow \Gamma_{8g}$ transitions only. The observation of the spectrum of sample S2A with the same HV polarization (input Y, output X) should show us both the $\Gamma_{6g} \rightarrow \Gamma_{8g}$ and the $\Gamma_{6g} \rightarrow \Gamma_{7g}$ transitions (see Fig. I-8); the spectra of these samples are shown in Fig. I-9.

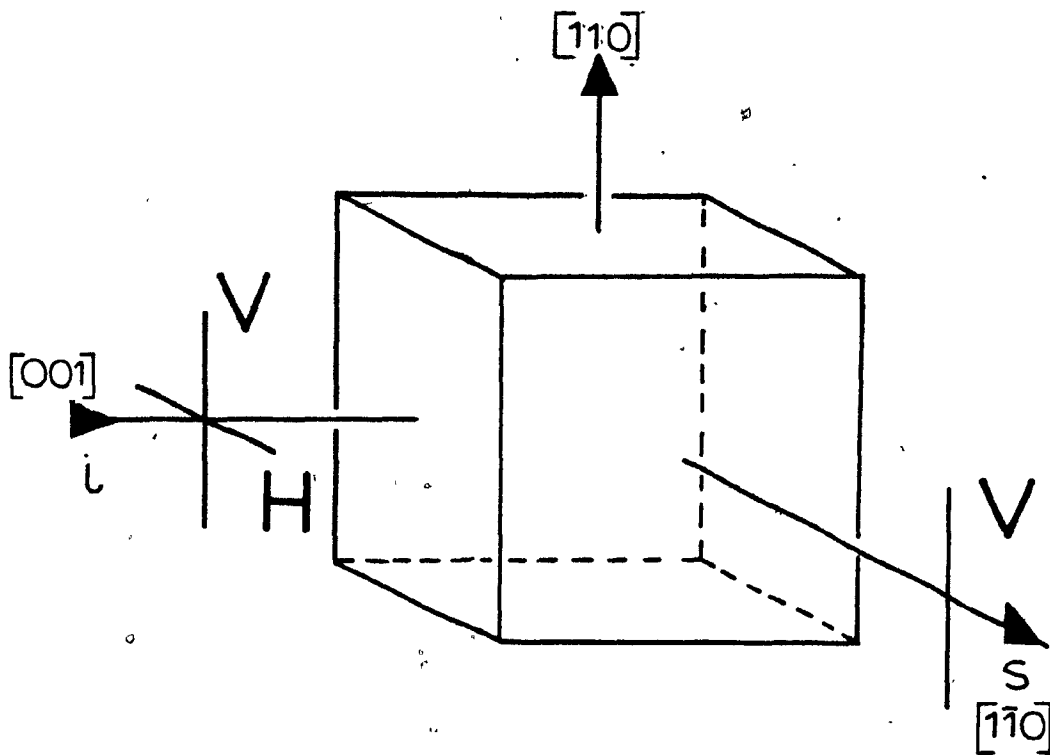
Table I-3. Optically active irreducible representations (i.r.) of O_h .

The dimension (dim.) of an i.r. is the same as the degeneracy of the corresponding level. No other representation of the group is optically active.

TABLE I-3

i.r.	dim.	bases	opt. activ.
Γ_{1g}	1	$x^2+y^2+z^2=r^2$	Raman
Γ_{3g}	2	$(3z^2-r^2), (x^2-y^2)$	Raman
Γ_{5g}	3	yz, zx, xy	Raman
Γ_{4u}	3	x, y, z	Infra-red

Fig. I-7. Orientation of sample SI.A. The product of the polarisations of the incident (i) and scattered (s) light give the basis of the irreducible representations (i.r.) that are activated (see Table I-3; V = vertical, H = horizontal).

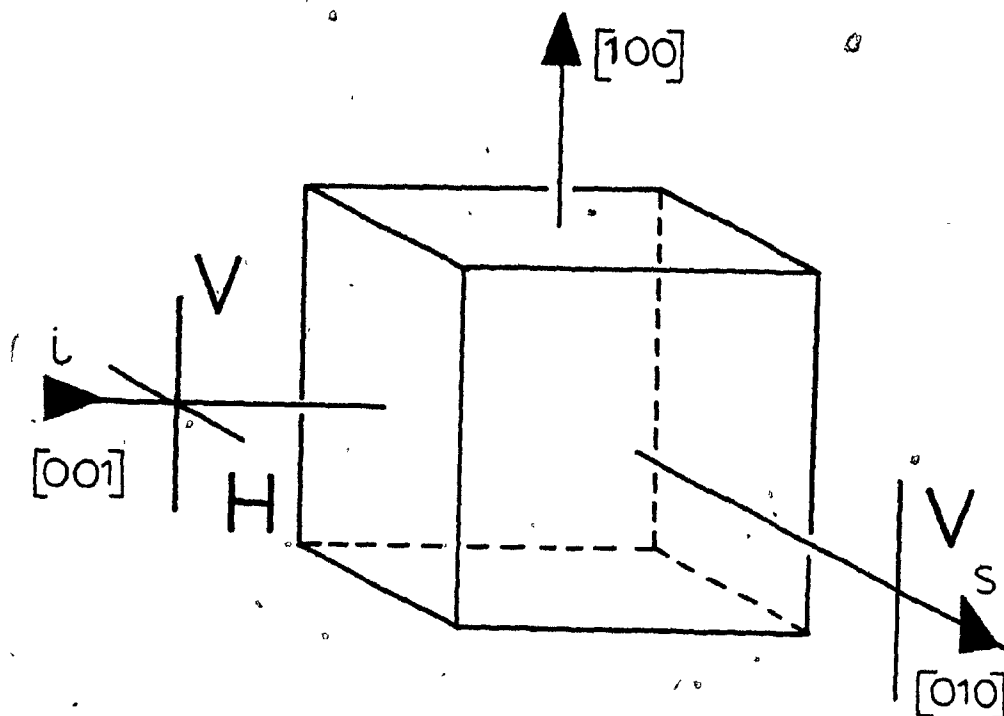


configurations

$$\begin{aligned}
 H \cdot V &= (x - y) \cdot (x + y) \\
 &= (x^2 - y^2) \sim \Gamma_{3g}
 \end{aligned}$$

$$\begin{aligned}
 V \cdot V &= (x + y) \cdot (x + y) \\
 &= (x^2 + y^2) + 2xy \\
 &\sim (\Gamma_{1g} + \Gamma_{3g}) + \Gamma_{5g}
 \end{aligned}$$

Fig. I-8. Orientation of samples S2A, S3B, S4B
and SP. See Fig. I-7 for details.



configurations

$$\begin{aligned}
 H \cdot V &= (y) \cdot (x) \\
 &= (yx) \sim \Gamma_{5g}
 \end{aligned}$$

$$\begin{aligned}
 V \cdot V &= (x) \cdot (x) \\
 &= (x^2) \sim \Gamma_{1g} + \Gamma_{3g}
 \end{aligned}$$

0

III. 2. Presentation and Interpretation of the Data

III. 2.1 - Comparison of Traces

Referring to Fig. I-9, beside the sharp peaks labeled p that are plasma lines (see section II.2 and [40]), both traces have some common features at 112, 280, 305, 930 and 1024 cm^{-1} from the laser line; all of these features are seen in the spectrum of sample S1A (Fig. I-10), obtained using a different lasing line (20718 cm^{-1}) which proves that they are Raman peaks. These features are more intense in the Γ_{3g} trace (Fig. I-9a) than in the Γ_{5g} trace (Fig. I-9b) except for the 1024 cm^{-1} peak which is more intense in the Γ_{3g} configuration; in this geometry an additional peak is seen at 900 cm^{-1} . In the same geometry we present the spectrum of the more doped sample (S3B) in Fig. I-11. Comparing the spectra of S3B (Fig. I-12) and S2A (Fig. I-13) under the $\Gamma_{1g} + \Gamma_{3g}$ configuration we found the following relation between the intensities (measured from the background) for the 280, 305 and 930 cm^{-1} lines: $I(S3B)/I(S2A) \sim 2$. We attribute these peaks to the presence of cobalt; the other features do not follow this relation.

III. 2.2 - Temperature Measurements

To characterize the nature of the peaks in the 300 cm^{-1} region, we measured the spectrum of sample S4B at different temperatures between 6°K and room temperature (19°C). This

Fig. I-9. Stokes Raman Spectra of S1A and S2A.

a) S1A in the Γ_{3g} geometry with 150 mW of laser power (18836 cm^{-1}) at $T = 15^\circ\text{K}$ (intensity values on the right).

b) S2A in the Γ_{5g} geometry with 170 mW of laser power (18836 cm^{-1}) at $T = 10^\circ\text{K}$ (intensity values on the left).

For both traces, the slits were 2 cm^{-1} , the scan rate was $20 \text{ cm}^{-1}/\text{min}$ and the time constant was 4.7 sec; the values of the peaks are precise to $\pm 1 \text{ cm}^{-1}$ and the peaks labelled "p" are Rayleigh scattered plasma lines of the krypton laser.

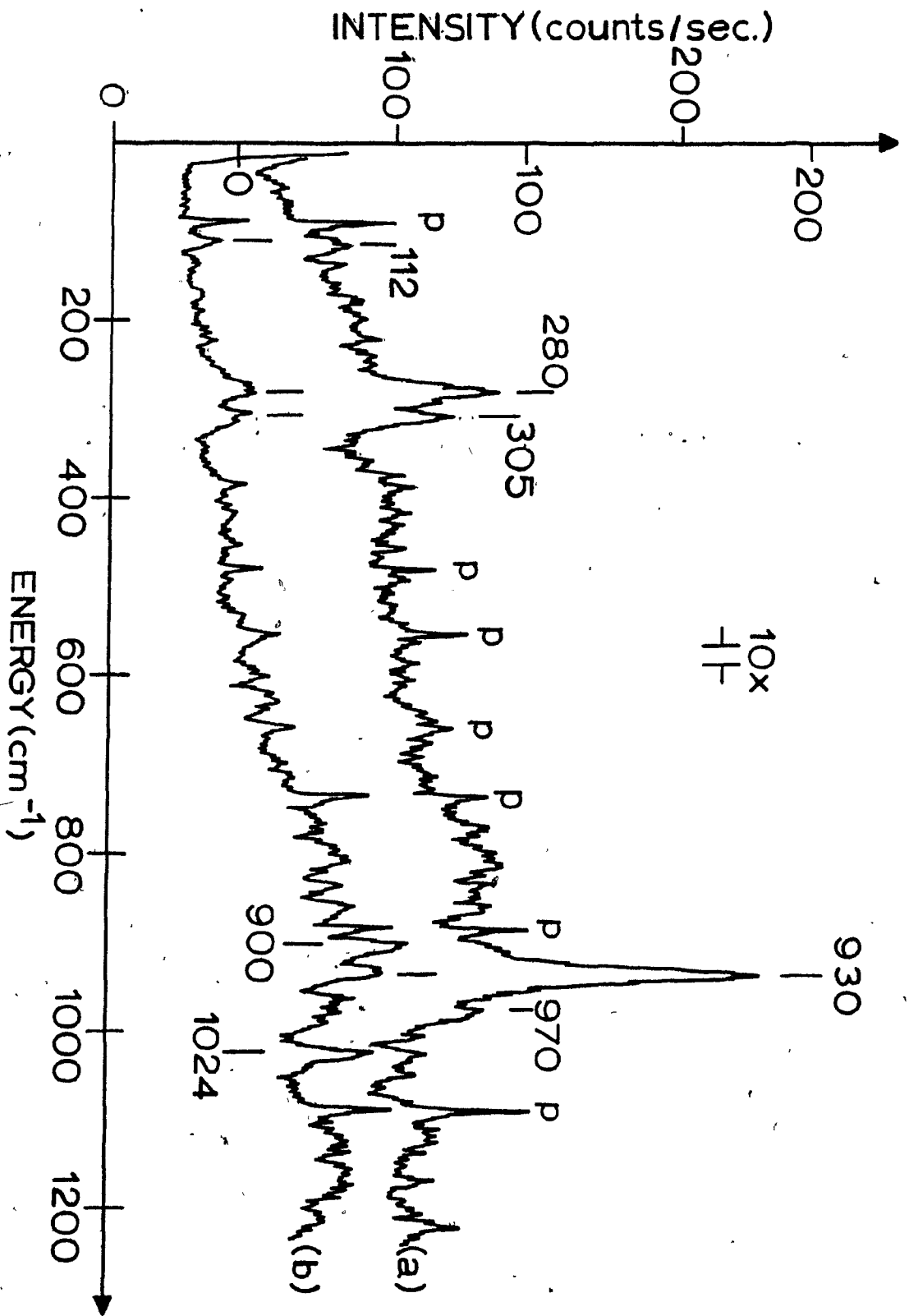


Fig. I-10. Spectrum of SIA with $L = 20717 \text{ cm}^{-1}$

This spectra was taken with the 20717 cm^{-1} lasing line (300 mW) with the sample in the Γ_{3g} geometry at low temperature (He gas; temperature not recorded). When compared to trace (a) of Fig. I-9, it shows that the peaks at 110, 280, 305 and 930 cm^{-1} are Raman peaks (slits: 3 cm^{-1} ; scan: $50 \text{ cm}^{-1}/\text{min}$; time constant: 4.7 sec). The line with label "p" are plasma lines.

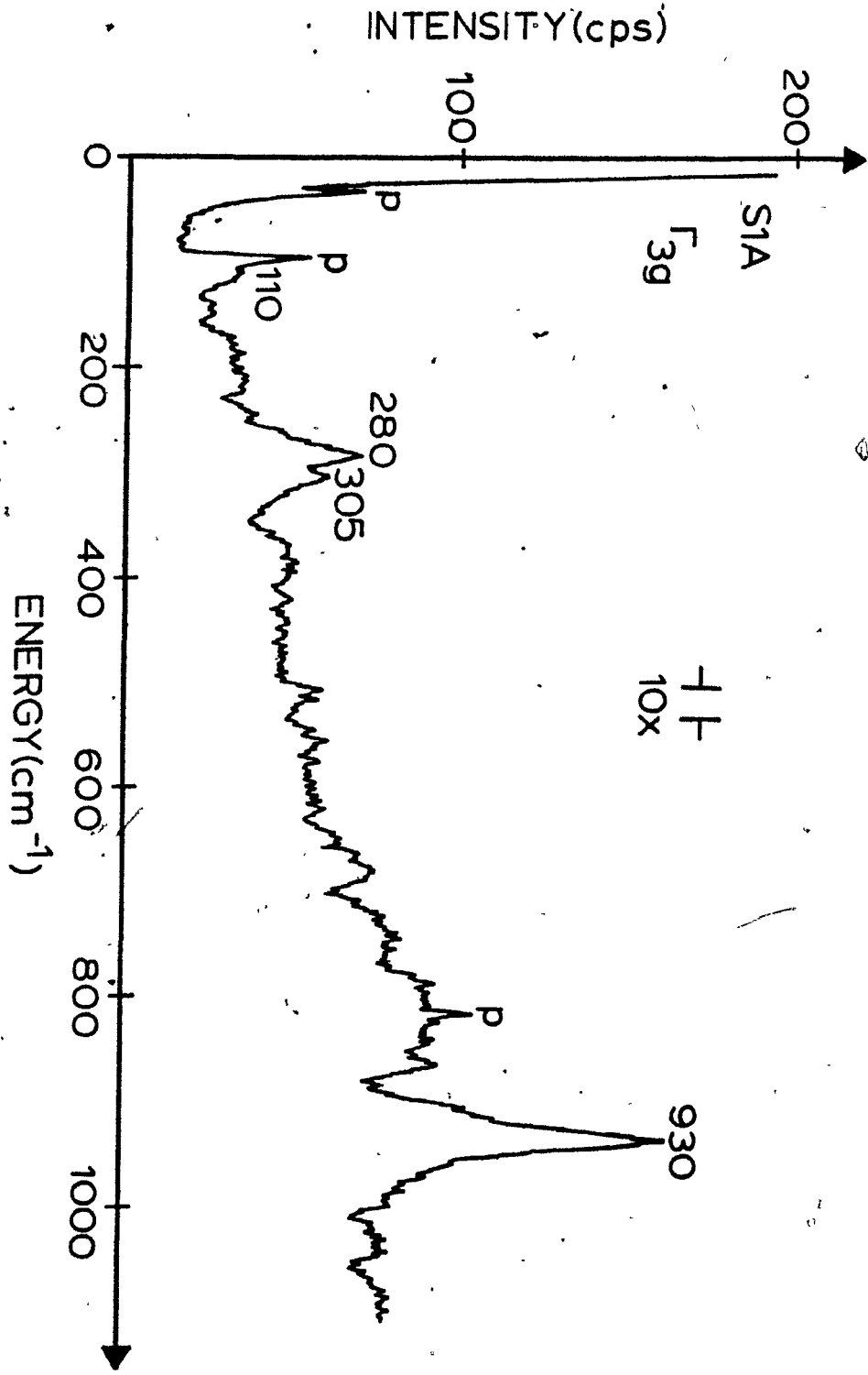


Fig. I-11. Stokes Raman spectrum of S3B (Γ_{5g}).
We used the 18836 cm^{-1} line (190 mW) of the Kr^+
laser with the sample at 10°K (slits: 2 cm^{-1} ;
error: $\pm 1 \text{ cm}^{-1}$; scan; $20 \text{ cm}^{-1}/\text{min}$; time constant:
4.7 sec).

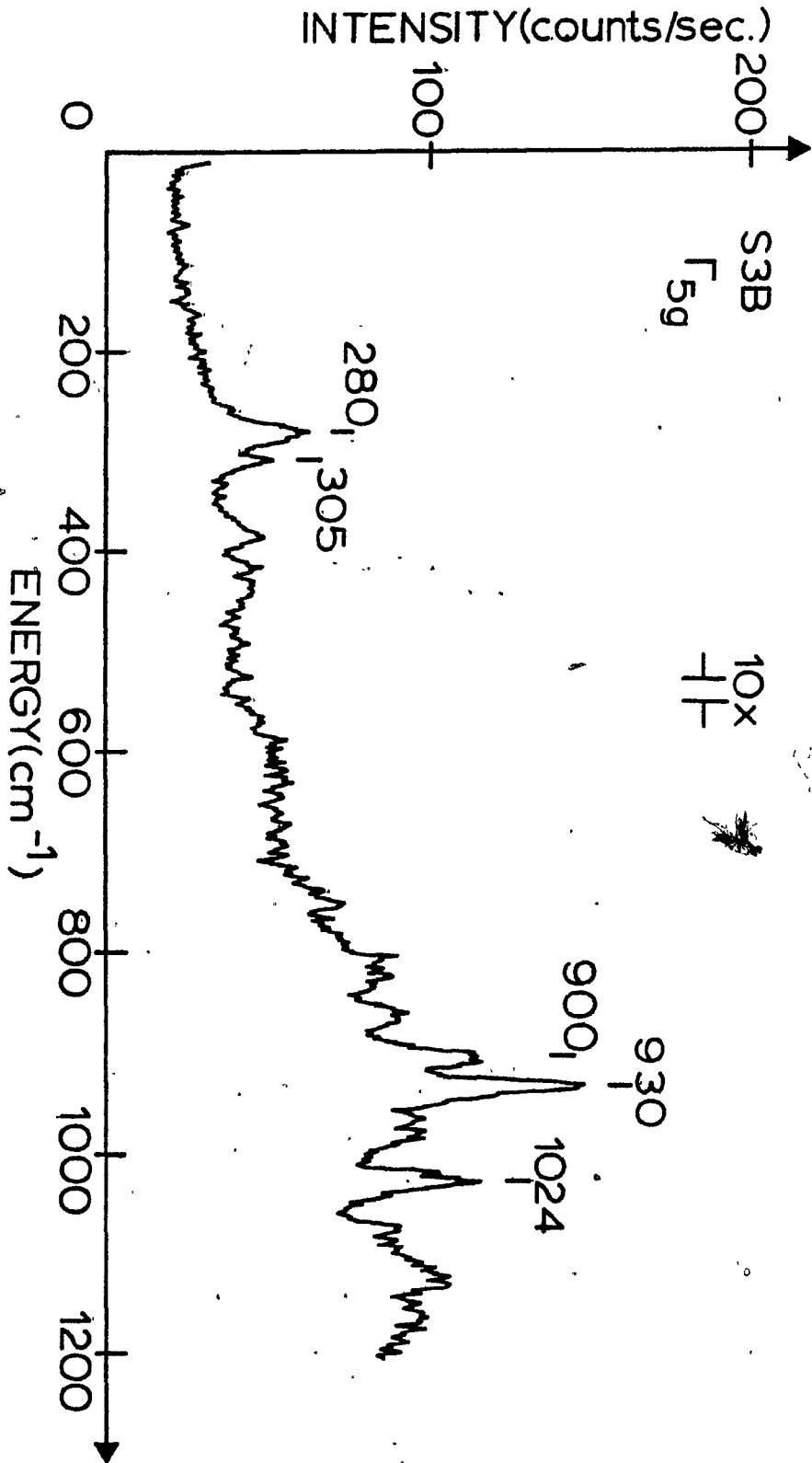


Fig. I-12. Stokes Raman spectrum of S3B

($\Gamma_{1g} + \Gamma_{3g}$).

We used 180 mW of the 18836 cm^{-1} laser line
with the sample at 8°K (slits: 2 cm^{-1} ; error:
 $\pm 1 \text{ cm}^{-1}$; scan: $20 \text{ cm}^{-1}/\text{min}$; time constant: 4.7 sec).

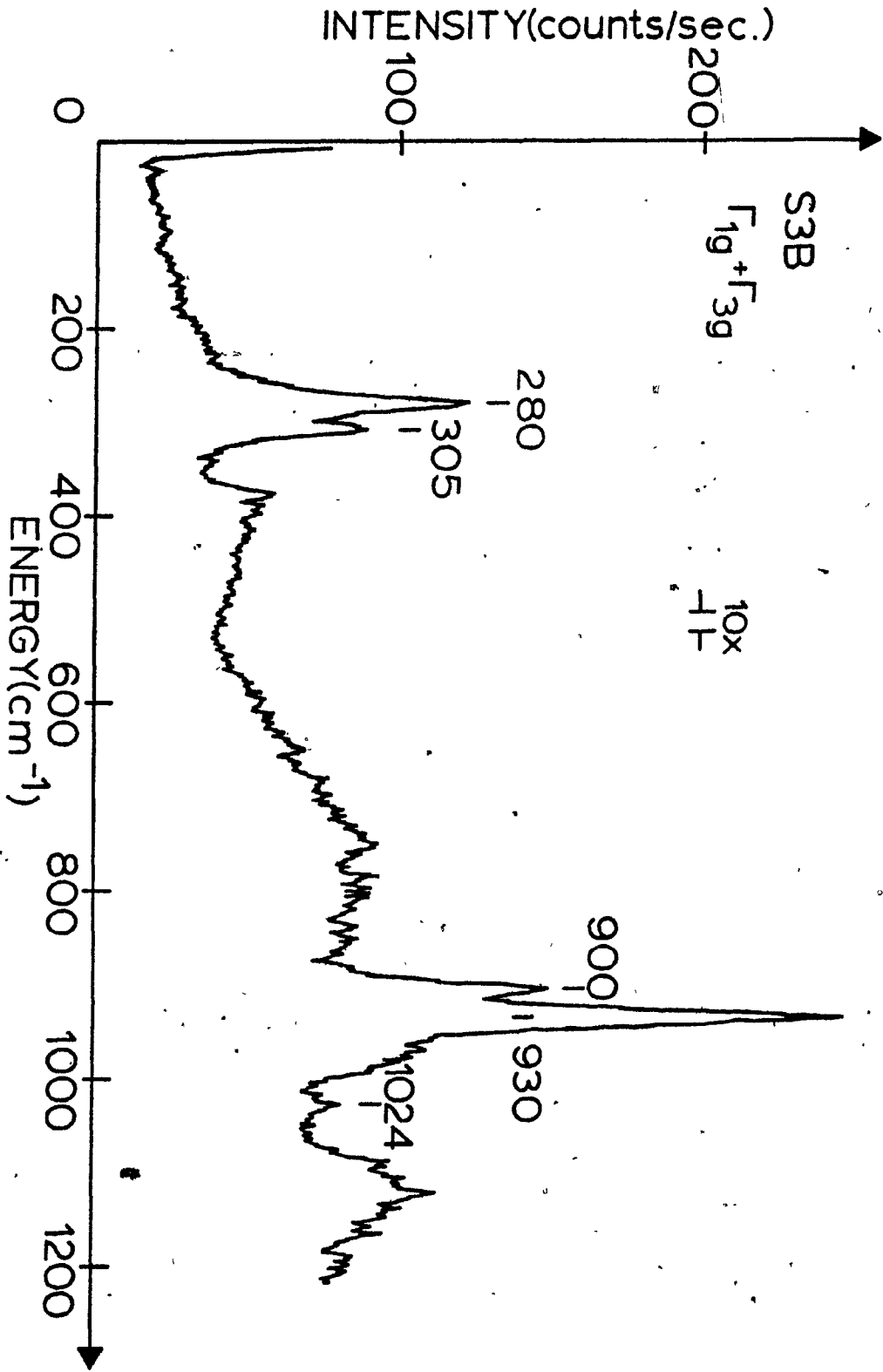
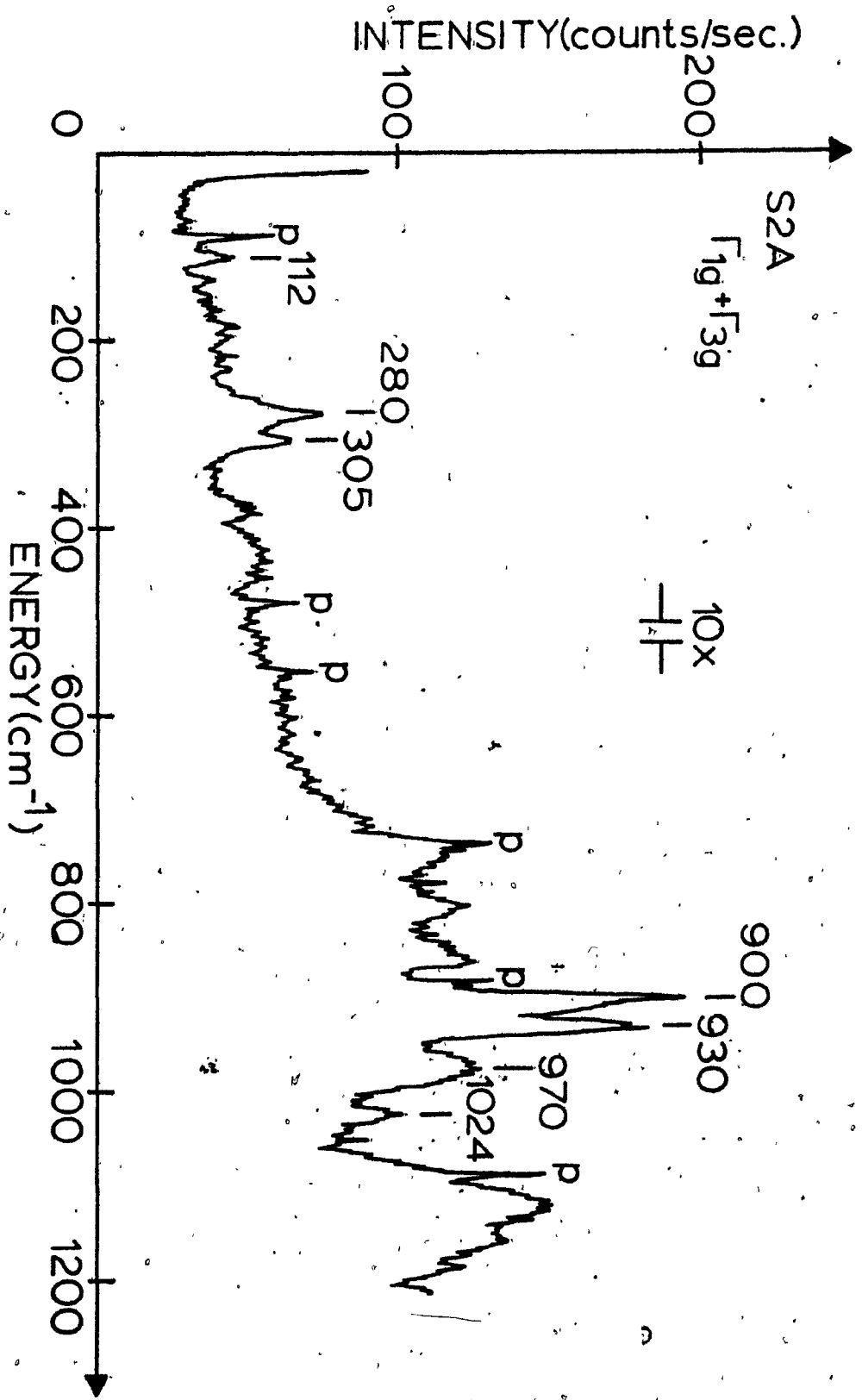


Fig. I-13. Stokes Raman spectrum of S2A ($\Gamma_{1g} + \Gamma_{3g}$).

The laser line was 18836 cm^{-1} (160 mW) and the sample was at 8°K ("p": plasma lines; slits: 2 cm^{-1} ; error: $\pm 1 \text{ cm}^{-1}$; scan: $20 \text{ cm}^{-1}/\text{min}$; time constant: 4.7 sec).



sample has the entrance and exit faces cleaved and the face on the 90° scattering direction polished. The length of the sample (along the beam) is such that the image of the sample exceeds the length of the spectrometer slit; for this reason and the fact that it is a crystal of good quality (no microbubble), no plasma lines appeared in the spectra.

In Fig. I-14 we show the spectra obtained at different temperatures between 6 and 292°K ; we notice that the 280 cm^{-1} peak is seen at low and high T (Fig. 14a and k), while the 305 cm^{-1} peak is not present at room temperature (the value marked on the figures are accurate to $\pm 3\text{ cm}^{-1}$). The behavior of these peaks, as a function of temperature, is better seen if we calculate their intensity ratio $I(280\text{ cm}^{-1})/I(305)$; this method permitted us to correlate the traces that were done under different conditions (different laser power and line, different scale). This data is presented in Fig. I-15; in Appendix F we explain the method of deconvolution we used to extract the values of the intensities. If both peaks were phonon modes, the ratio of the intensities would be

$$\frac{I(\bar{\nu}_1=280)}{I(\bar{\nu}_2=305)} = \frac{A_1(1-\exp-\bar{\nu}_1/T)}{A_2(1-\exp-\bar{\nu}_2/T)} \quad (\text{I-13})$$

with T expressed in cm^{-1} ($0.695\text{cm}^{-1}/^\circ\text{K}$). The value of the ratio A_1/A_2 can be obtained from the intensity ratio at low

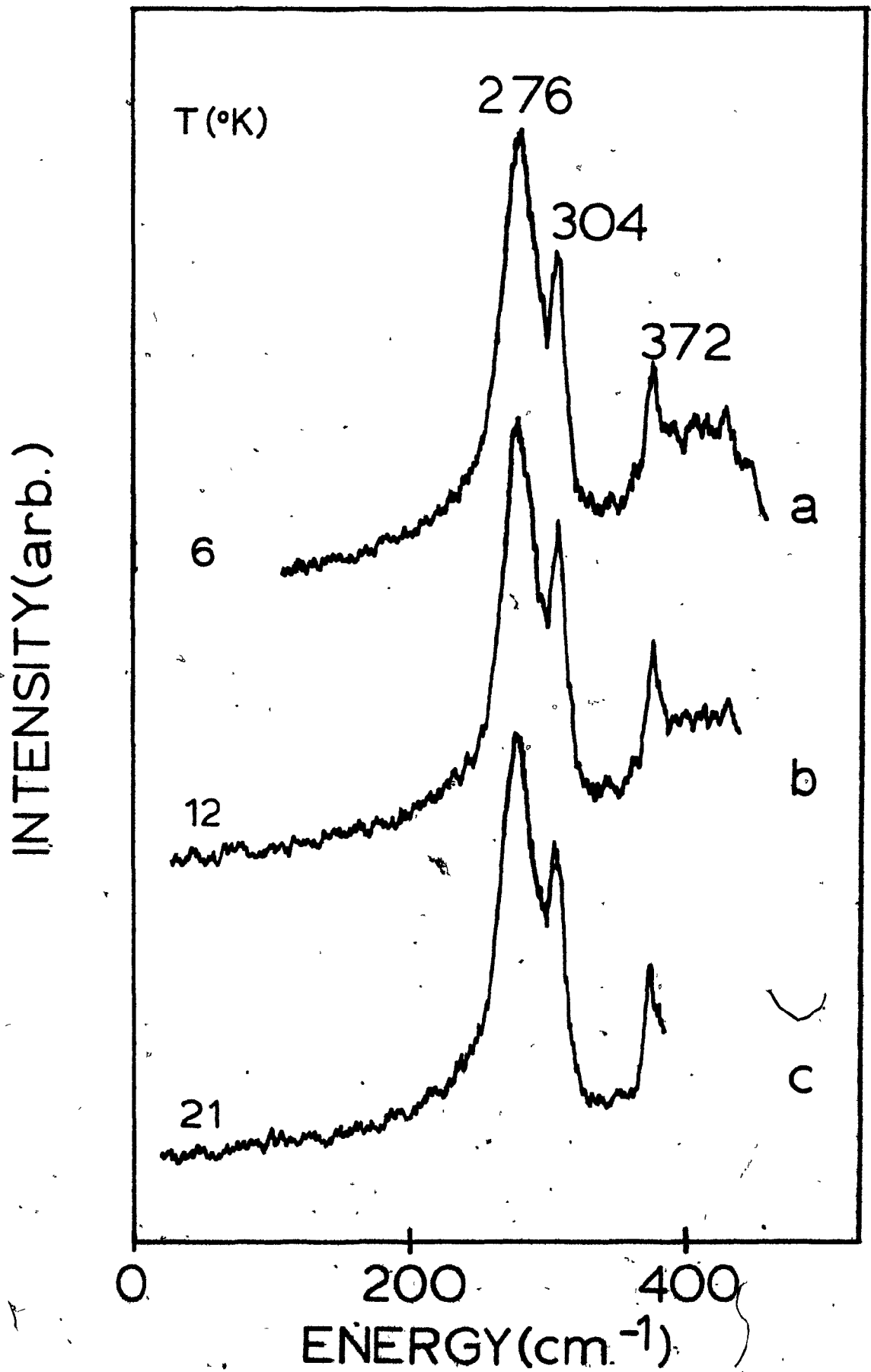
temperature; this expression (Equ. I-13) corresponds to the continuous line in Fig. I-15. Our temperature dependant spectra and its analysis show that the intensity of the 305 cm^{-1} peak decreases more rapidly than that of the 280 cm^{-1} peak; this last peak is still visible at room temperature (19°C) while the other has disappeared. We identify the 280 cm^{-1} peak as an induced mode and the 305 cm^{-1} peak as being an electronic level of Co^{2+} . The 930 cm^{-1} peak decreased rapidly with temperature and is not present at room temperature (Fig. I-14, l and m); we identify this peak to the $\Gamma_{6g} + \Gamma_{8g}^2$ electronic transition of Co^{2+} in MgO .

Fig. I-14. Stokes Raman Spectra of S4B (T = 6 to 292°K)

All traces were done at $20 \text{ cm}^{-1}/\text{min}$ with a time constant of 4.7 sec and slits of 3 cm^{-1} . The temperature is given at the left of each trace (in °K); some of the peaks value is given and when the value is not given it corresponds to the value given before $\pm 3 \text{ cm}^{-1}$. In some of the figures the baseline was shifted for convenience; this does not influence the analysis of the peaks (see Appendix F) (L = laser line; power in parenthesis; scale). All the traces are in the $\Gamma_{1g} + \Gamma_{3g}$ configuration.

Spectra of the 300 cm^{-1} region (a to k).

- a) T = 6°K; L = 18836 cm^{-1} (130 mW); 1 kcps
- b) T = 12°K; L = 18836 cm^{-1} (125 mW); 1 kcps
- c) T = 21°K; L = 18836 cm^{-1} (120 mW); 1 kcps



0
JL14
2011/11

Fig. I-14. (Cont'd)

7
0
For the next seven traces (d to j) the conditions are the same except for the temperature ($L = 20717 \text{ cm}^{-1}$; 80 mW; 300 cps).

d) $T = 90^\circ\text{K}$, e) 116, f) 133, g) 152, h) 171, i) 190, j) 210.

For trace k) the conditions are $T = 292^\circ\text{K}$, $L = 18836 \text{ cm}^{-1}$; 200 mW; 300 cps. Note the change of scale for traces d) to k) as compared with a) to c).

INTENSITY(arb.)

T(°K)

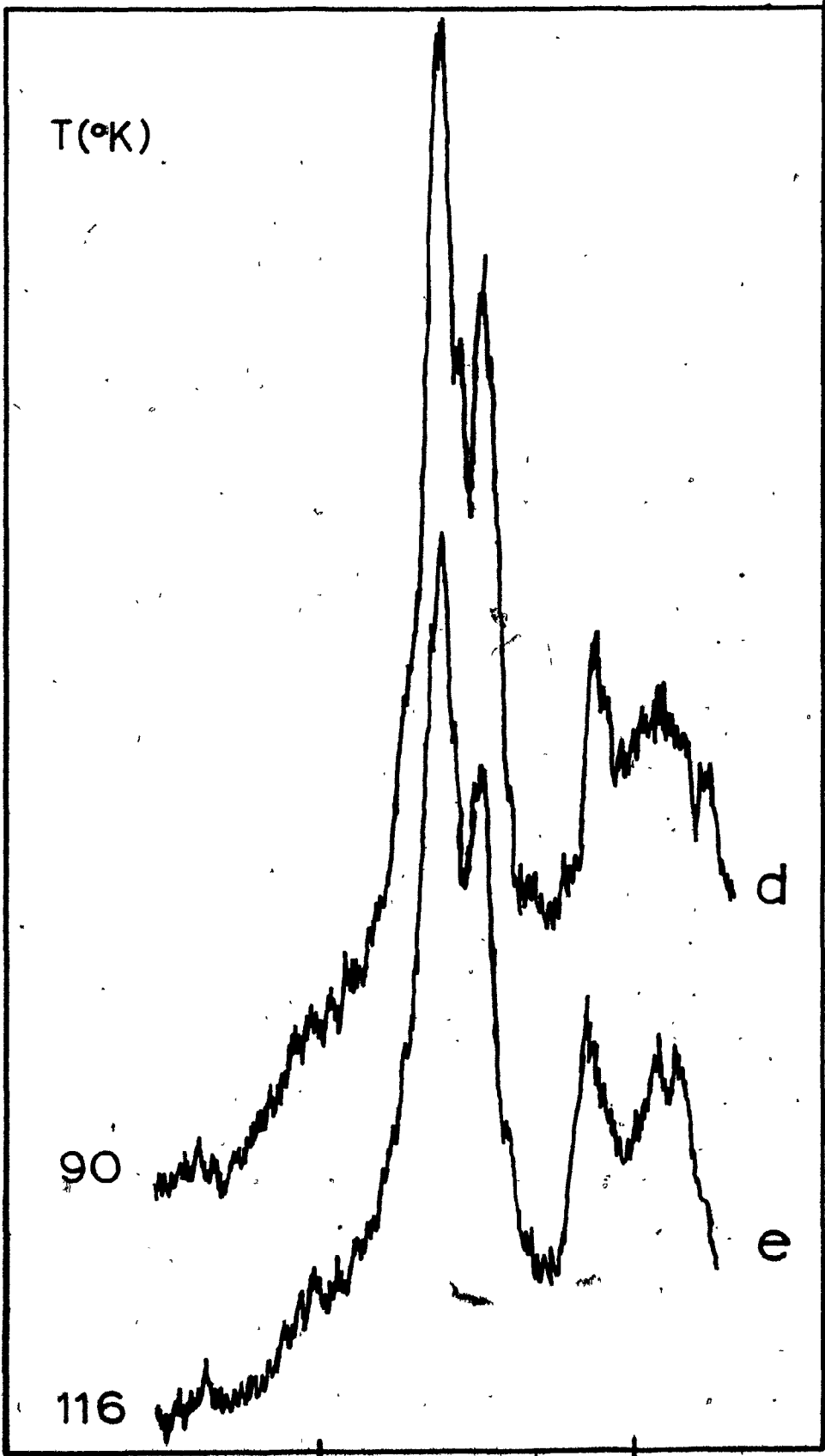
90

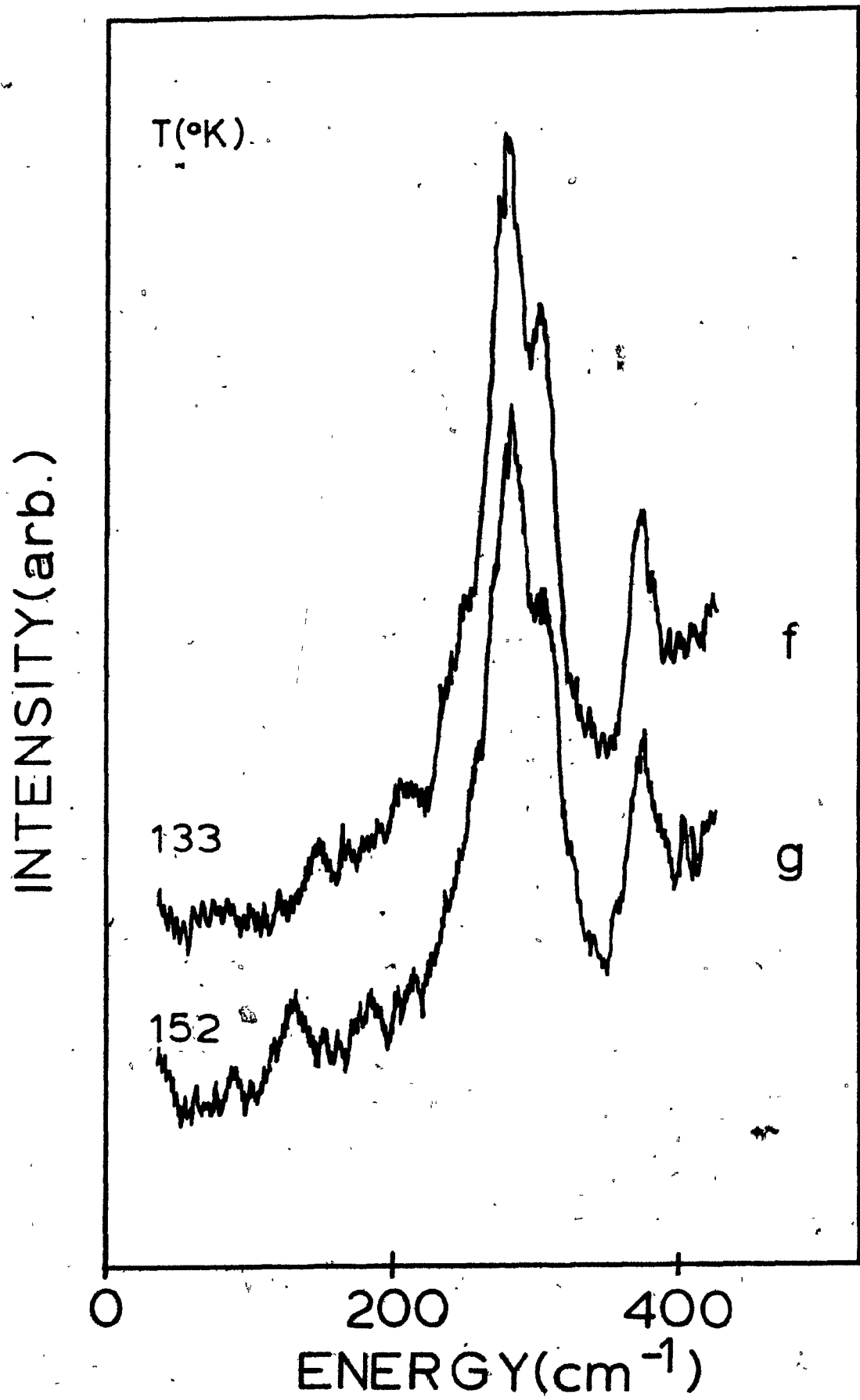
116

d

e

0 200 400
ENERGY(cm⁻¹)





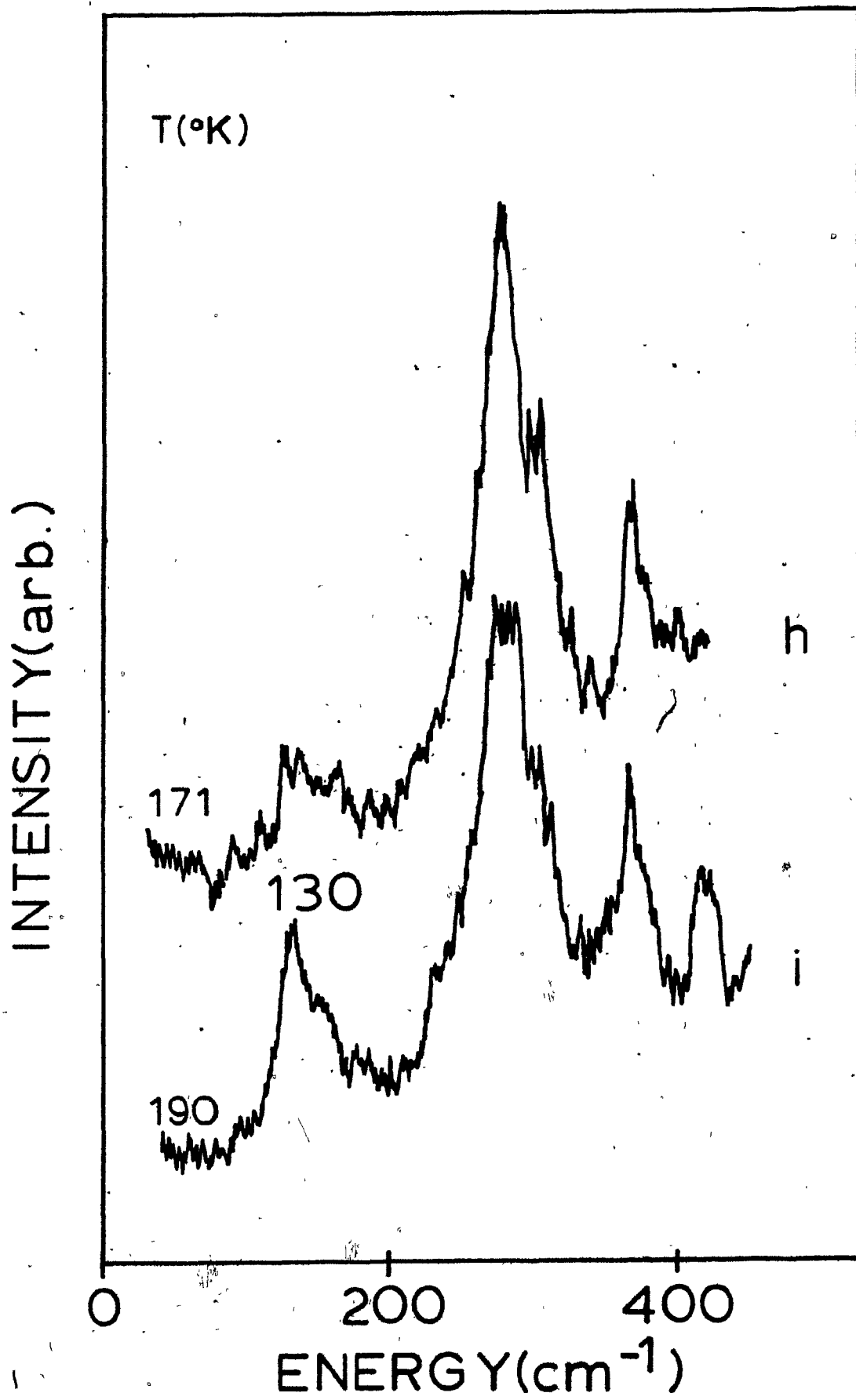


Fig I-14.

h + i

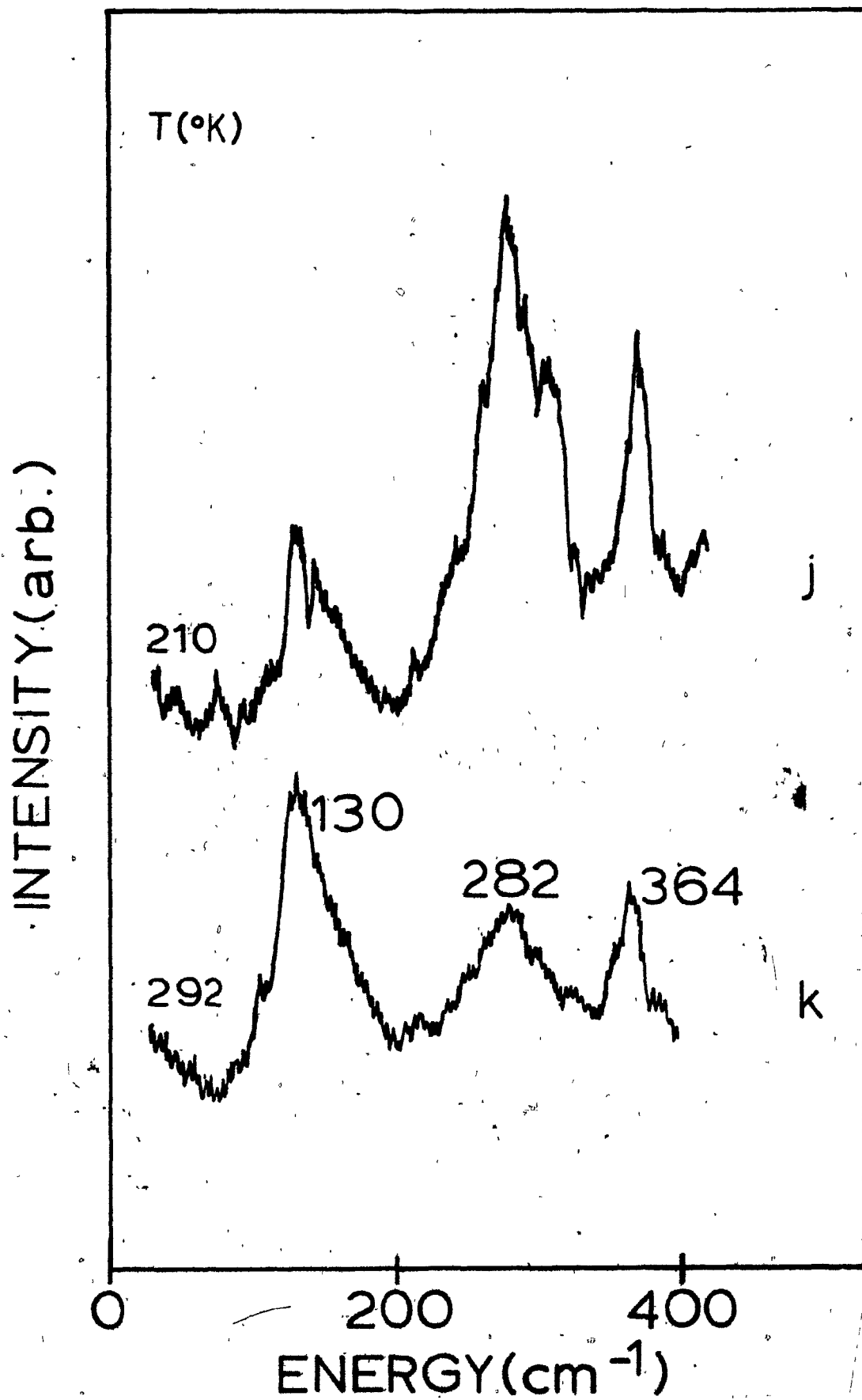
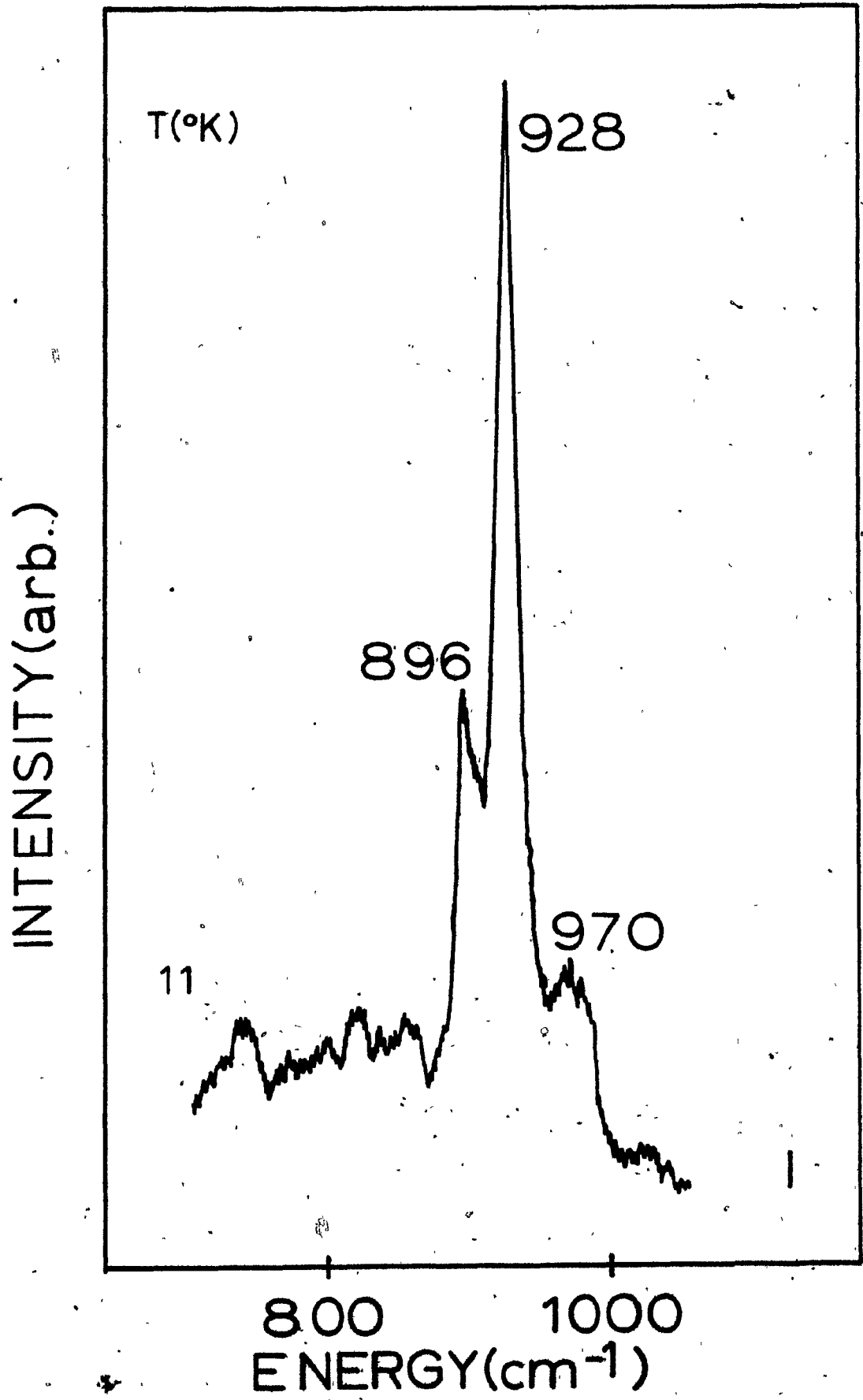


Fig. I-14. (Cont'd)

Spectra of the 900 cm^{-1} region (l to n) ($L = 18836\text{ cm}^{-1}$).

- l) $T = 11^\circ\text{K}$; Power (P) = 115 mW; 1 kcps
- m) $T = 150^\circ\text{K}$; P = 125 mW; 1 kcps
- n) $T = 292^\circ\text{K}$; P = 200 mW; 300 cps

Note the change of scale for trace n).



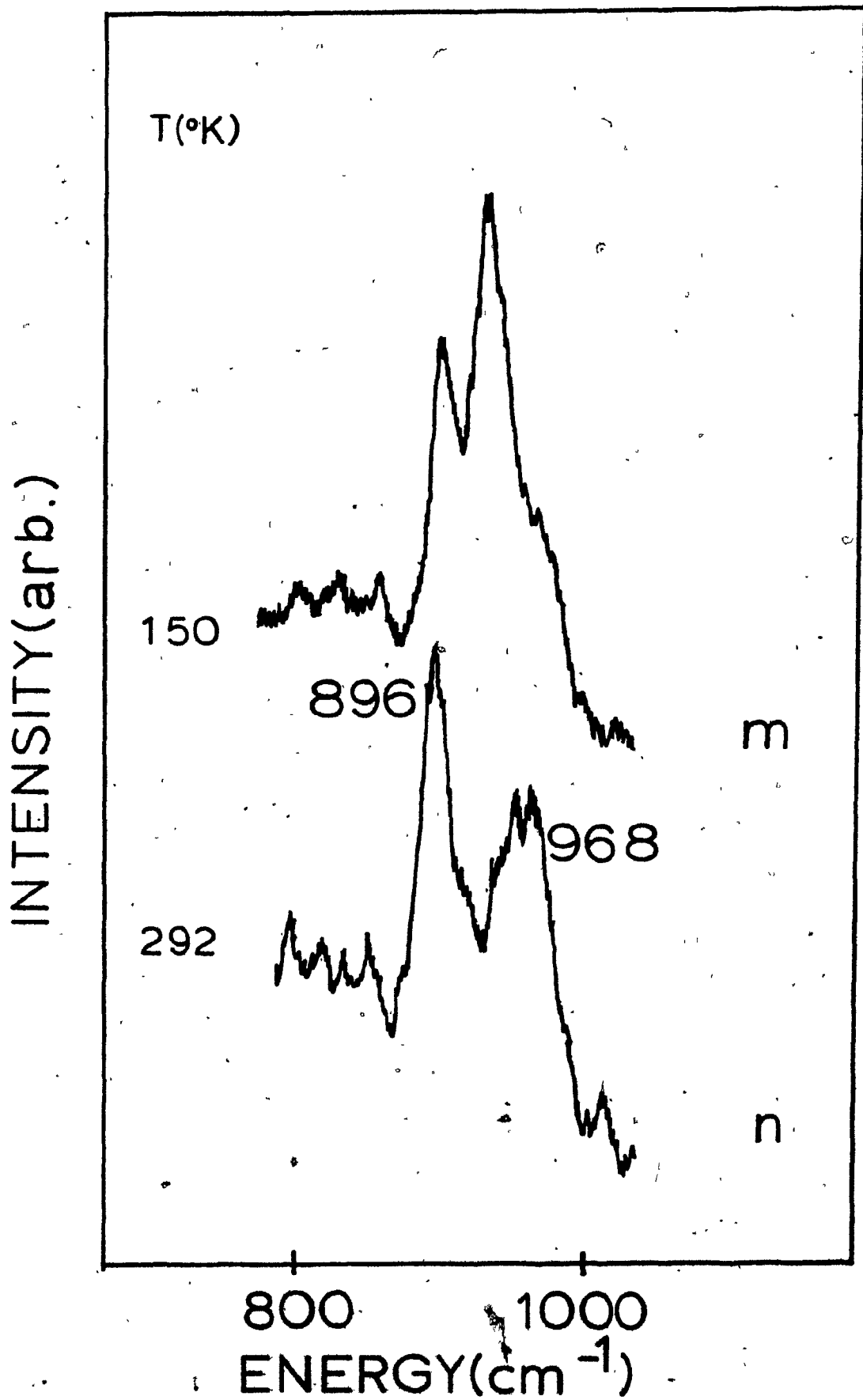


Fig. I.14
m+n

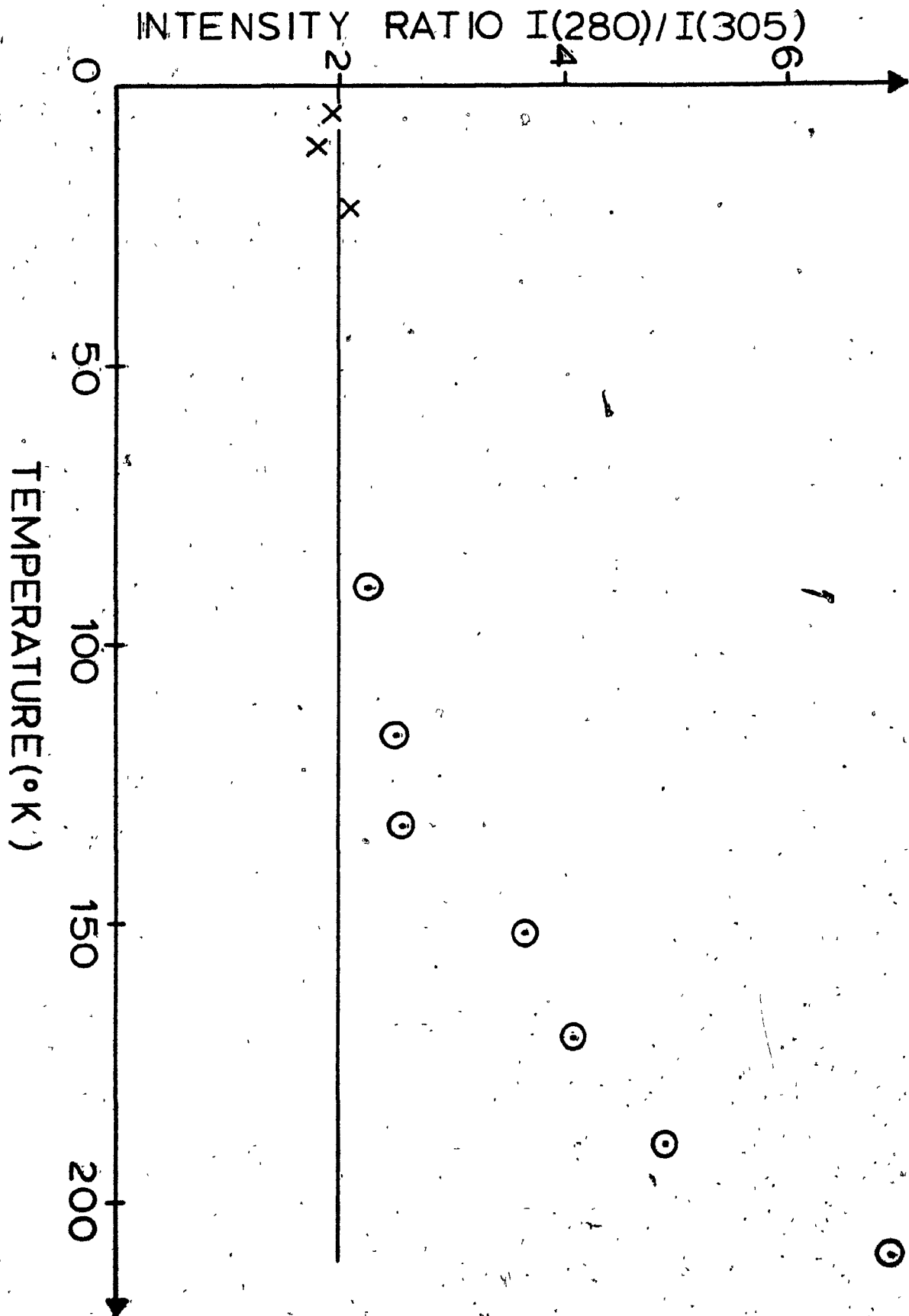
Fig. I-15. Dependence of $I(280 \text{ cm}^{-1})/I(305)$ with temperature

The data for this graph was extracted from the spectra of sample S4B using the deconvolution scheme explained in Appendix F. The symbols used are related to the experimental conditions (all the traces were done the same day):

✕ $L = 18836 \text{ cm}^{-1}$ (125 mW); slits: 3 cm^{-1} ; scan rate: $20 \text{ cm}^{-1}/\text{min}$
scale: 1 kcps; time constants 4.7 sec.

⊙ $L = 20717 \text{ cm}^{-1}$ (80 mW); slits: 3 cm^{-1} ; scan rate: $20 \text{ cm}^{-1}/\text{min}$
scale: 300 cps; time constant: 4.7 sec.

The continuous line corresponds to the theoretical expression (Equ. I-13) of the ratio if both peaks were phonons; with $A_1/A_2 = 2.0$ we find that this expression gives a ratio of 1.95 at $T = 200^\circ\text{C}$.



III. 2.3 - Identification of the Peaks

In a crystal where each atomic site is a center of symmetry (or inversion), which is the case for pure MgO, first-order vibrational Raman scattering is forbidden [41,42]; the presence of an impurity at those sites, such as the cobalt ion at the magnesium site, breaks the symmetry of translation and relaxes the $\vec{k} = 0$ phonon selection rule (see Part II Chapter I). If the impurity ion has a different charge and/or size it will distort its environment and the cluster, formed by the impurity and its first-nearest neighbours, can possess local modes of vibration which have frequencies above the maximum frequency of the host lattice; if the frequency of the mode is in the gap between the optical and acoustic branches it is called a gap mode [43].

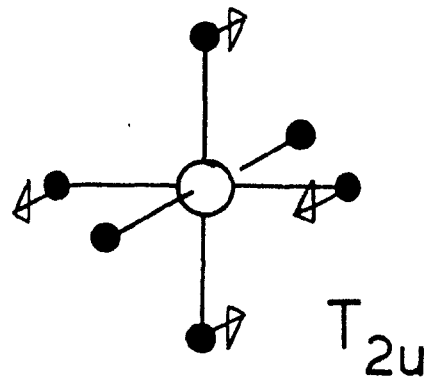
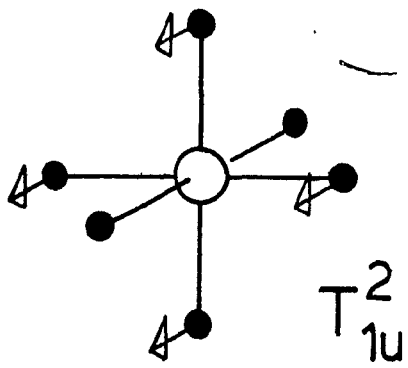
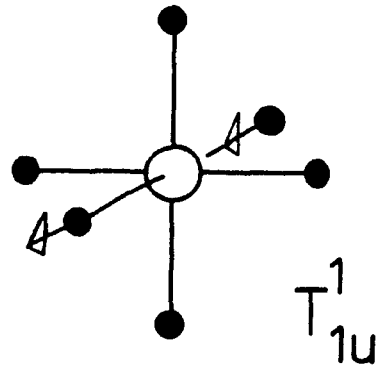
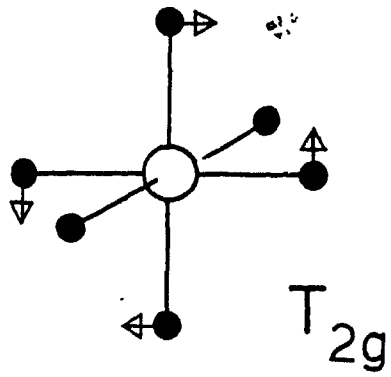
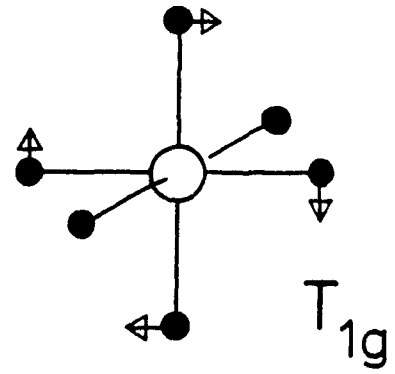
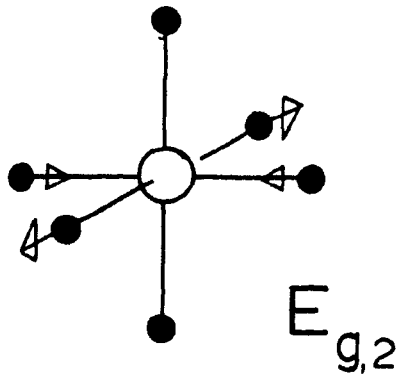
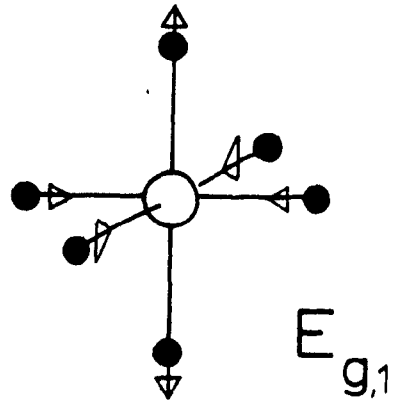
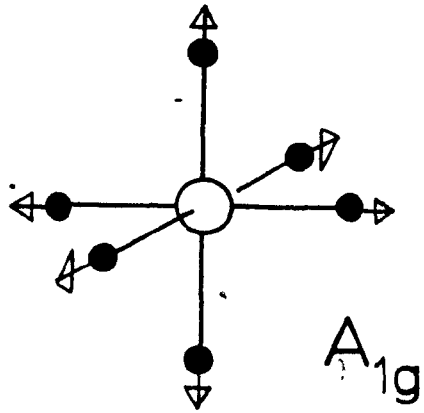
The charge of the cobalt ion (2+) is the same as the magnesium ion (+2) it replaces and its size is slightly bigger; the interatomic distance in MgO is 2.11Å while in CoO it is 2.13Å [44]. Because the cobalt impurity does not disturb much its local environment [45], its localized mode can be nearly degenerate with the lattice vibrations. The frequency of the localized mode will not depend on the mass of the impurity if the symmetry of the mode is A_{1g} , E_g , T_{1g} , T_{2g} , T_{1u}^1 and T_{1u}^2 and T_{2u} (see Fig. I-16) [46]; in these modes the impurity atom is immobile. The peak at 280 cm^{-1} is a localized E_g mode which

Fig. I-16. Local modes for an immobile impurity [20,46].

We show both partners of the E_g modes; the partners of the T modes can be obtained by a 90° rotation of the cluster about the O-Co-O axes. The irreducible representations for the movement of the cluster (ignoring translations) are

$$A_{1g} + E_g + T_{1g} + T_{2g} + 2 T_{1u} + T_{2u};$$

T_{1g} corresponds to a rotation of the cluster.



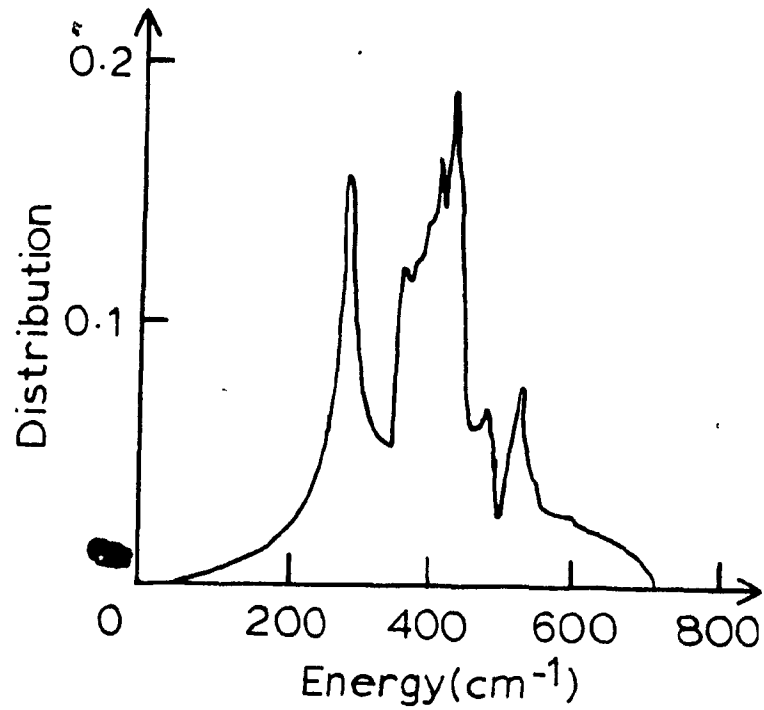


Fig. I-17. Phonon frequency distribution.
Function calculated by Sangster et al [48]
from neutron scattering experiments; notice
the first peak near 300 cm^{-1} which is the
contribution of the acoustic modes.

readily couples with the lattice modes. The transverse acoustic modes at the high symmetry $X(1\ 0\ 0)$ and $L(\frac{1}{2}\ \frac{1}{2}\ \frac{1}{2})$ points on the boundary of the Brillouin zone contribute to form the first peak ($\sim 280\text{ cm}^{-1}$) in the unperturbed lattice phonon frequency distribution function (Fig. I-17) calculated by Peckham [47] and Sangster et al. [48] from their neutron scattering data. Then, the localized mode is called a resonance mode.

Cossee [49] has estimated indirectly from magnetic susceptibility a value of 306 cm^{-1} for the electronic transition $\Gamma_{6g} \rightarrow \Gamma_{8g}^1$ of the ${}^4T_{1g}({}^4F)$ manifold of cobalt in MgO while Liehr [50] has predicted it at 315 cm^{-1} from ligand field calculations. From their near infrared fluorescence and absorption measurements, Ralph et al. [51] deduced a value of 300 cm^{-1} for the transition. We interpret the 305 cm^{-1} peak as being this $\Gamma_{6g} \rightarrow \Gamma_{8g}^1$ transition.

Beyond these features, a complex series of bands and peaks extends from 650 to 1250 cm^{-1} which is best seen in Fig. I-13 ($S2A, \Gamma_{1g} + \Gamma_{3g}$). This structure can be compared with the spectrum of the pure sample SP (Fig. I-18) under the same geometry; a laser filter monochromator (Anaspec 300S) was used to eliminate the plasma lines in the spectrum of SP. The trace of SP, done at 10°K , correlates well with the two phonons Raman data of Manson et al. [8] and most of the structure in this region for the doped samples behaves the same way under similar polarization configurations (Fig. I-19).

Fig. I-18. Stoke Raman spectrum of SP ($\Gamma_{1g} + \Gamma_{3g}$).
We used 300 mW of the 18836 cm^{-1} laser line
while the sample was at 10°K (slits: 2 cm^{-1} ;
error: $\pm 1 \text{ cm}^{-1}$; scan: $50 \text{ cm}^{-1}/\text{min}$; time constant:
4.7 sec). Only the peaks near 1000 cm^{-1} are identified.

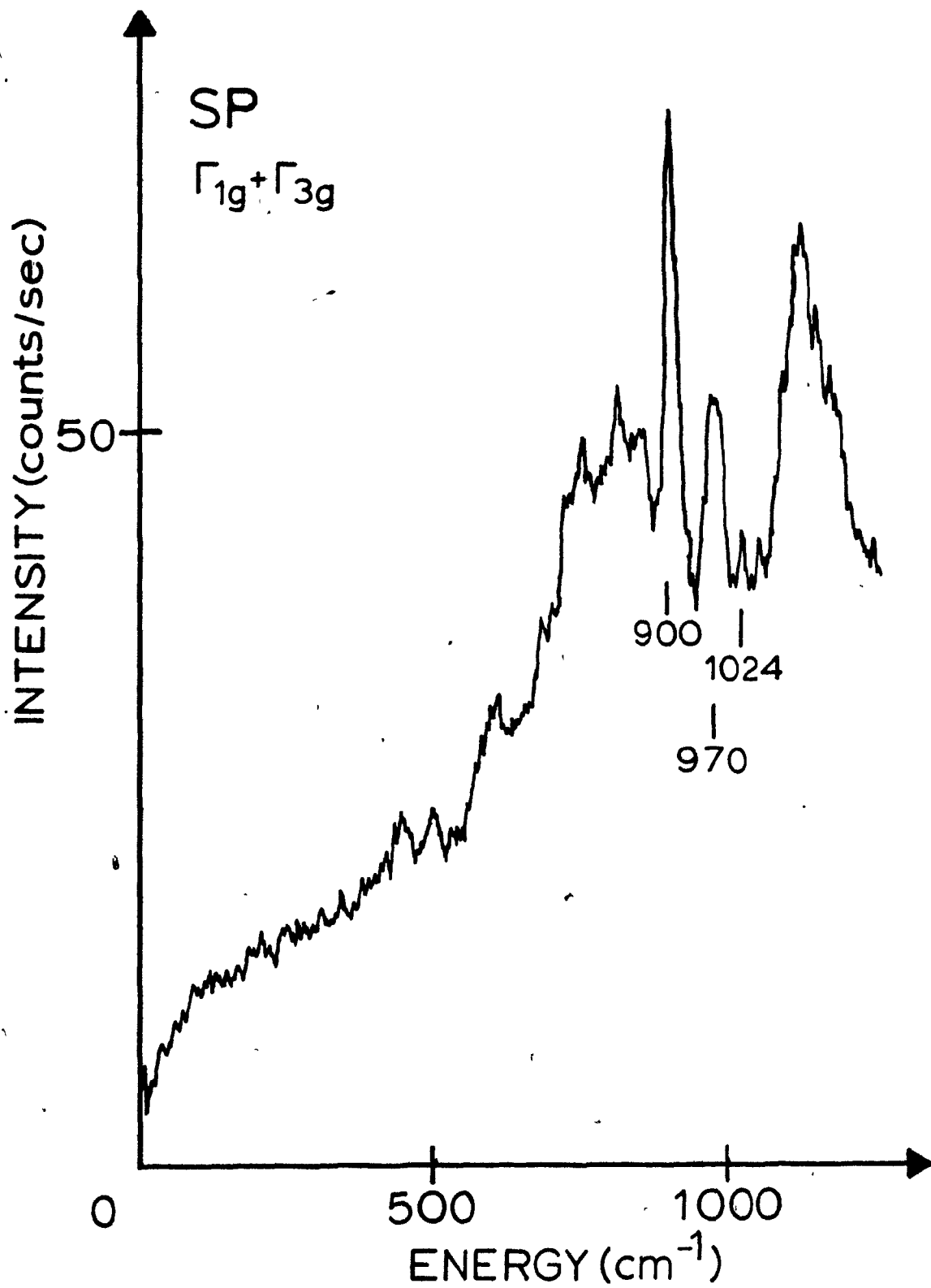
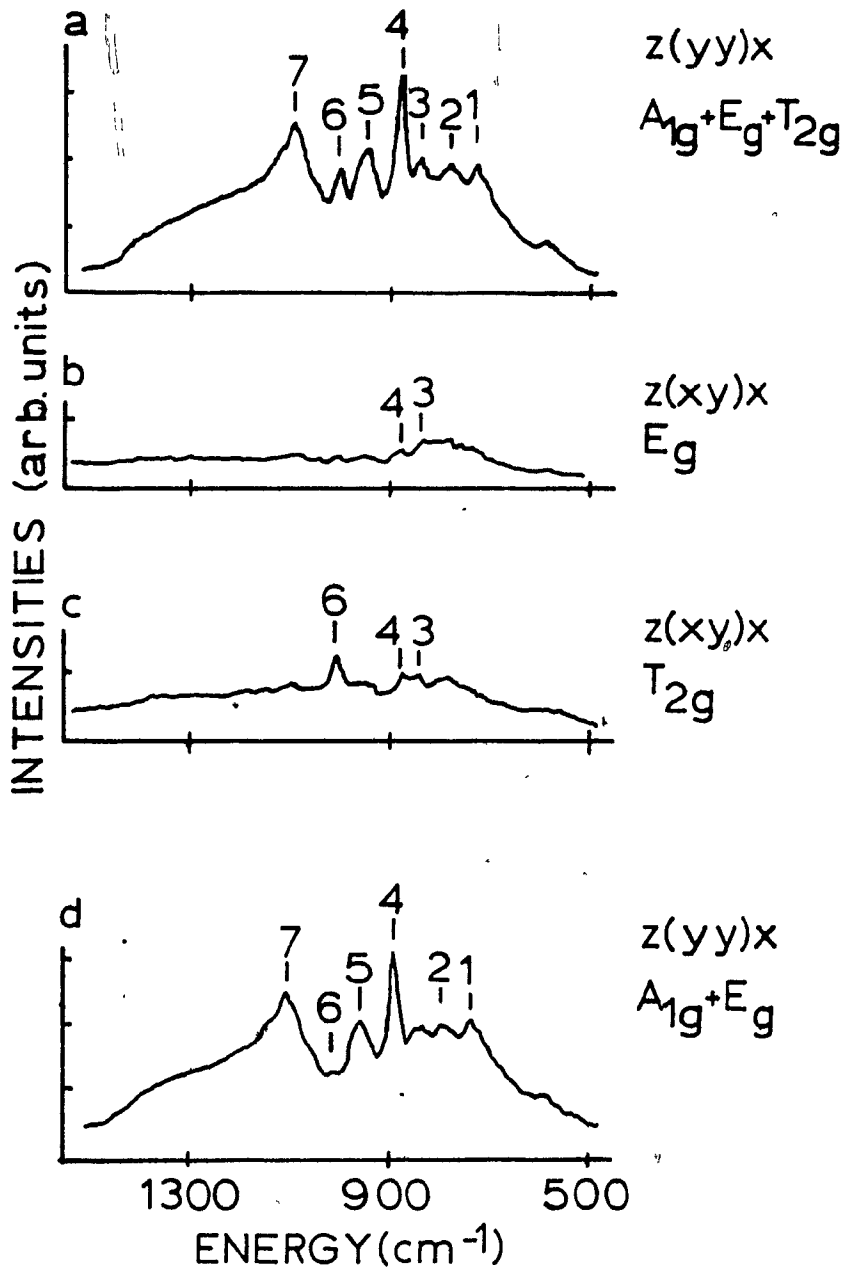


Fig. I-19. Second-order Raman spectra of pure MgO [8].

Room temperature measurements under different geometry using the 20492 cm^{-1} (488.0 nm) of an argon ion laser; the incident beam was in the same direction ($\vec{q}_i // [001]$) for all traces but the scattered beam was $\vec{q}_s // [110]$ for a and b traces, and $\vec{q}_s // [100]$ for c and d; note that the wavenumber increases to the left.



$$1 = 742 \text{ cm}^{-1}$$

$$5 = 975 \text{ cm}^{-1}$$

$$2 = 801$$

$$6 = 1019$$

$$3 = 858$$

$$7 = 1098$$

$$4 = 895$$

The peak at 930 cm^{-1} does not correspond to any structure in the two phonons spectrum of the pure sample; this line was identified by Guha [23] as the $\Gamma_{6g} \rightarrow \Gamma_{8g}^2$ transition. When comparing the spectra of S3B (Fig. I-12) and S2A (Fig. I-13), the more doped sample S3B has this line more intense by a factor of two while the structure around it has decreased in intensity; the 930 cm^{-1} line is interpreted as the electronic transition $\Gamma_{6g} \rightarrow \Gamma_{8g}^2$ of the cobalt ion.

Based on group theory alone, under the Γ_{5g} configuration we should see the $\Gamma_{6g} \rightarrow \Gamma_{7g}$ transition; the peaks that appear in this geometry are related to the two-phonon spectrum. This transition in a similar cubic structure ($\text{KZnF}_3:\text{Co}^{2+}$) is also absent from the Raman data of Lockwood et al. [18]. We say that this transition is quantum mechanically weak.

The small peak at 112 cm^{-1} is an electronic Raman transition of iron (Fe^{2+}) at a cubic site [52] (see Fig. I-9 and I-13). The structure at 130 cm^{-1} ($T > 150^\circ\text{K}$; Fig. I-14 g to k) corresponds to a two-phonon difference band as identified by Manson et al. [8]. Other features appear in this region which are impurity induced vibrational modes but their nature and behaviour is of no concern to us; suffice it to say that the 370 cm^{-1} peak shifts toward the laser line as the temperature increases.

III. 3 Results of Calculations

III. 3.1 - Spin-Orbit Interaction

Before calculating the energy separations of the levels, let us see if our measurements of the cobalt ion levels follow the Lande interval rule [53]. With the energy of the levels labeled by their representation we have for the first transition:

$$\Gamma_{8g}^1(j = 3/2) - \Gamma_{6g}(j = 1/2) = \frac{3}{2}\zeta(\gamma S \ell) \quad (\text{I-14a})$$

and between the two excited states:

$$\Gamma_{8g}^2(j = 5/2) - \Gamma_{8g}^1(j = 3/2) = \frac{5}{2}\zeta(\gamma S \ell) \quad (\text{I-14b})$$

with ζ being the term interval parameter. Manipulating these equations and comparing with our experimental values we get

$$\frac{\Gamma_{8g}^2(5/2) - \Gamma_{6g}(1/2)}{\Gamma_{8g}^1(3/2) - \Gamma_{6g}(1/2)} = \frac{8}{3} \quad ; \quad \frac{930}{305} \sim \frac{9}{3} \quad (\text{I-15})$$

The agreement is fairly good considering the fact that in this system an additional interaction (Jahn-Teller effect) is present and can depress each level differently; that aspect will be analysed at the end of this section.

We have calculated (Appendix A) the energies of the levels using the spin-orbit Hamiltonian of Ray et al. [33] and diagonalizing the interaction matrix. The energy separations are (from Eq. A-7):

$$E (\Gamma_{6g} \rightarrow \Gamma_{8g}^1) = -\frac{9}{4} ak\lambda_0 - \frac{99}{16} \frac{akk'\lambda_0^2}{\Delta} \quad (I-16a)$$

$$E (\Gamma_{6g} \rightarrow \Gamma_{8g}^2) = -6 ak\lambda_0 - \frac{27}{2} \frac{akk'\lambda_0^2}{\Delta} \quad (I-16b)$$

$$E (\Gamma_{6g} \rightarrow \Gamma_{7g}) = -6 ak\lambda_0 \quad (I-16c)$$

with "a" the term mixing parameter and k, k' the covalency parameters of the ${}^4T_{1g}$ and ${}^4T_{2g}$ states respectively; the energy separation between these two states is Δ . We have neglected the $\Gamma_8^1 - \Gamma_8^2$ mixing interaction (Appendix B). All the energies are positive because the spin-orbit coupling parameter λ_0 for the free cobalt ion is negative ($\lambda_0 = -180 \text{ cm}^{-1}$) and the first term of equations 16a and 16b is larger than the second.

III. 3.2 - Comparison With Our Data

As given in Appendix A (Eq. A-4 and A-5) the mixing parameter "a" is a function of the crystal field parameter Dq

and of Racah's B parameter; using $Dq = 960 \text{ cm}^{-1}$ [32] and $B = 840 \text{ cm}^{-1}$ [33] we find $a = 0.935$. With this value of "a", we adjusted the parameters k and k' so that the energy separation agrees with either the 305 cm^{-1} (Table I-4a) or the 930 cm^{-1} (Table I-4b) peaks for the corresponding $\Gamma_{6g} \rightarrow \Gamma_{8g}^1$ and $\Gamma_{6g} \rightarrow \Gamma_{8g}^2$ transitions. As can be seen, no values of the fitting parameters simultaneously give a good fit for both peaks. The g-factor of the Γ_{6g} level is known to be 4.278 [32] and is related to a , k and k' by

$$g = \frac{10}{3} + ak\left(1 - \frac{15}{2} \frac{k'\lambda_0}{\Delta}\right) \quad (\text{I-17})$$

For $a = 0.935$, the value of k' ranges from 0.06 to 0.84 while k varies from 1.00 to 0.88; in our analysis, k and k' are pure covalency reduction parameters and to explain the g-factor, we have to include in these parameters an additional factor that takes account of the dynamic Jahn-Teller effect.

III. 3.3 - Dynamic Jahn-Teller Interaction

The cobalt ion in MgO is known to be a weak Jahn-Teller system [33]; we calculated (Appendix C) the influence of a first excited vibronic level having one E_g phonon quantum

TABLE I-4

Values of the covalency parameters ($k' \leq k < 1.00$) that either fit the 305 cm^{-1} peak(a) or the 930 cm^{-1} peak(b) ($a = 0.935$; $\Delta = 8Dq = 7680 \text{ cm}^{-1}$; $B = 840 \text{ cm}^{-1}$).

	k	k'	$\Gamma_6 \rightarrow \Gamma_8^1$ (cm^{-1})	$\Gamma_6 \rightarrow \Gamma_8^2$ (cm^{-1})	$\Gamma_6 \rightarrow \Gamma_7$ (cm^{-1})
(a)	0.86	0.86	307.6	829.0	868.4
	0.85	0.81	305.1	821.7	858.3
	0.84	0.64	305.0	819.6	848.2
	0.83	0.46	305.0	817.8	838.1
	0.82	0.27	305.1	816.2	828.0
	0.81	0.08	305.1	814.5	817.9
(b)	0.98	0.98	347.7	938.5	989.6
	0.97	0.95	344.8	930.4	979.5
	0.96	0.77	345.5	930.0	969.4
	0.95	0.58	346.3	930.0	959.3
	0.94	0.38	347.2	930.2	949.2
	0.93	0.18	348.1	930.2	939.1

of energy. We found identical energy shifts for both Γ_{8g} levels [54]. We then included the effect of one T_{2g} phonon and found a differential shift for these two levels. The total shifts $\delta(\Gamma)$ due to the interaction with one E_g and one T_{2g} phonons are:

$$\delta(\Gamma_{8g}^1) = -\frac{81}{50} E_{jt}(E) - \frac{243}{100} E_{jt}(T) \quad (I-18a)$$

$$\delta(\Gamma_{8g}^2) = -\frac{81}{50} E_{jt}(E) - \frac{243}{1600} E_{jt}(T) \quad (I-18b)$$

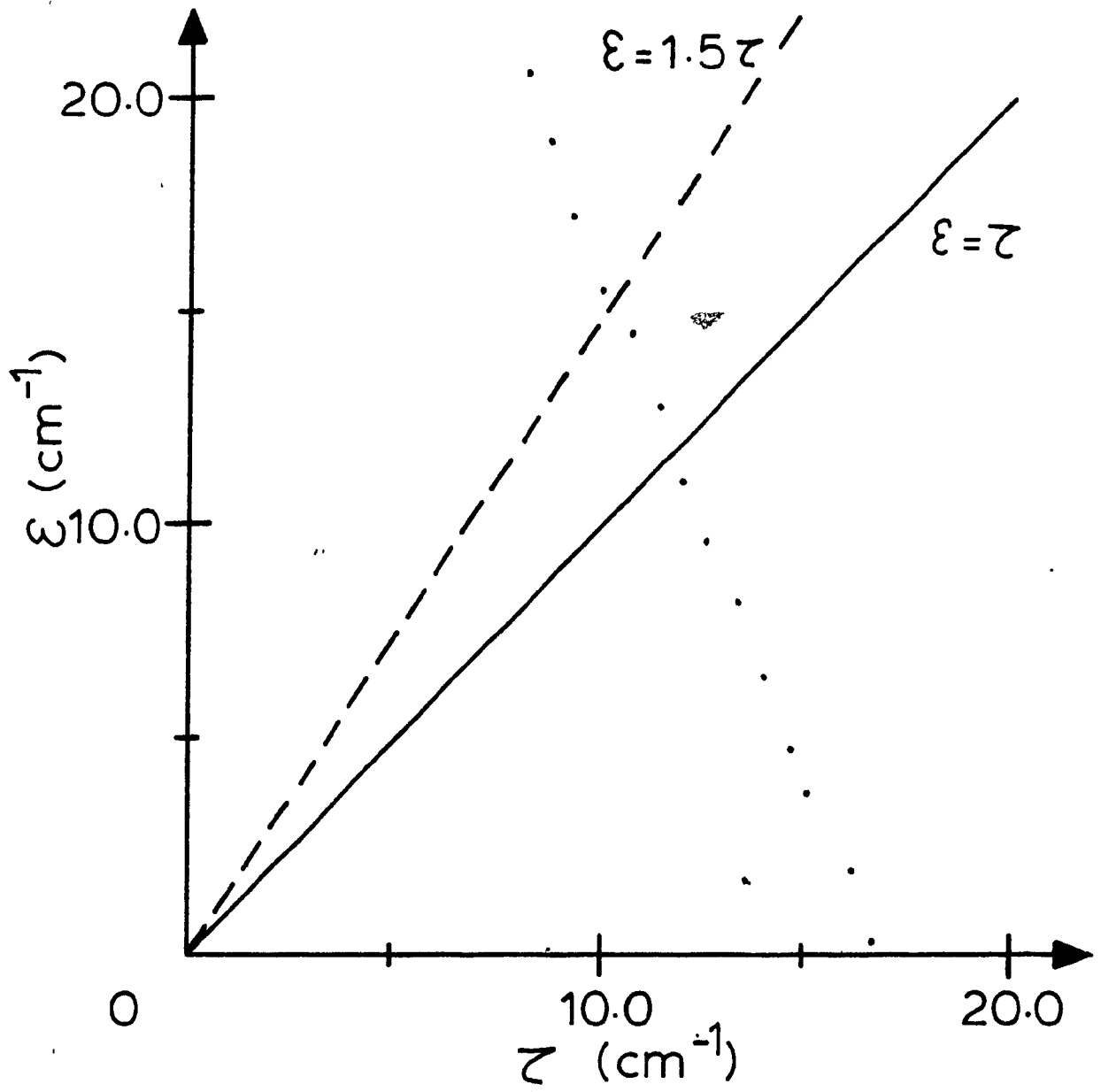
with $E_{jt}(E) = V_e^2/2\mu\omega_e^2$ and $E_{jt}(T) = 2V_t^2/3\mu\omega_t^2$.

Using our experimental values for the position of the Γ_{8g}^1 and Γ_{8g}^2 levels and equations I-16 and I-18 we found the values of $E_{jt}(E) = \epsilon$ and $E_{jt}(T) = \tau$ for a number of (k, k') values (Fig. I-20); the discontinuous line at $(\epsilon/\tau) = 1.5$ corresponds to the values of ϵ and τ for which the two contributions to the shift of Γ_{8g}^1 are equal. In our approximation we have supposed that the one-phonon vibronic levels are exactly $\hbar\omega$ higher than the no-phonon levels and so we cannot evaluate the values of V_e , V_t and ω_e , ω_t .

From this graph, using reasonable values of $k = 0.97$ and $k' = 0.90$, we get $E_{jt}(T) = 16.7 \text{ cm}^{-1}$, if we suppose a negligible contribution from the E_g mode coupling ($\epsilon = 0.3 \text{ cm}^{-1}$).

Fig. I-20. The Jahn-Teller energies.

The values of $E_{jt}(E) = \epsilon$ and $E_{jt}(T) = \tau$, that fit our experimental results are given for different values of the covalency parameters ($0.85 \leq k' \leq k$; $0.97 \leq k \leq 1.00$; $a = 0.935$). The series of dots crosses the $\epsilon = \tau$ line near $\tau = 12 \text{ cm}^{-1}$ and the $\epsilon = 1.5\tau$ line near 10 cm^{-1} .



III. 4. Uniaxial Stress and Other Treatments

We took several Raman spectra of a doped sample under uniaxial pressure along the [100] direction with the apparatus illustrated in Fig. I-6a. The reduction in symmetry from O_h to D_{4h} , is expected to split a Γ_{8g} level into two Kramers doublets, while a Γ_{6g} and Γ_{7g} being already Kramers doublets will not split (only a magnetic field can split these doublets). We did not detect any splitting or shift of the lines up to a maximum stress of 28 kg/mm^2 . With a slightly modified equation for the tetragonal static stress [34] and with the value of the maximum stress used, we calculated the energy separation of the splitting of the Γ_{8g} levels to be approximately 5 cm^{-1} . The width of our lines, at half the intensity, is about 20 cm^{-1} and is produced by the presence of random static strain in our samples. The simple observation of our samples, between crossed polarizers in monochromatic light, showed the presence of non uniformed static strain.

In order to render a sample strain-free, we annealed it in a vacuum for 24 hours at 1200°C . At the end of the treatment, the ampoule was quenched in cold water to permit the condensation of the water vapor, liberated by the crystal surfaces, on the inner wall of the ampoule (when a magnesium oxide crystal is exposed to the humidity in the air, a powder of magnesium hydroxide forms on its surfaces).

The surfaces of the samples had to be repolished because this treatment also damaged the surfaces by releasing the oxygen (reducing effect). The spectra of this sample, with no uniaxial stress applied, showed no improvement of the width of the Raman lines.

We also irradiated another sample with an unfocused X-ray beam for 12 hours in the hope of changing the divalent cobalt into trivalent ions [56]. The spectra observed for this sample did not show any additional lines.

III. 5. - Other Systems Studied

In the progress of the present work, we searched, in other cobalt-doped systems, the electronic lines of the impurity ion in an octahedral site. We first looked at $\text{NaCl}:\text{Co}^{2+}$ (0.05%) and found that its Raman spectra is identical to that of a pure NaCl sample; it showed the two-phonon spectrum as seen by Krauzman [7] under the same polarisation geometries. No sharp peaks can be seen at low temperature (He λ point, 77°K) that are not visible at room temperature.

We decided to look at cobalt substituting for tantalum in the KTaO_3 perovskite; the impurity site in this compound is also octahedral. We measured the spectra of a lightly doped ($\sim 0.01\%$) sample and two more doped samples (0.04g and 0.08g of CoO in the melt of 20g Ta_2O_3 + 9.4g K_2CO_3);

the color density for these samples is proportional to the concentration. The two-phonon spectrum signal at low temperature ($\sim 15^\circ\text{K}$) is fairly large (1-10kcps) and covers the region from the laser to 1100 cm^{-1} . We did not observe any peak that could be related to the cobalt impurity. All the features in our spectra could be identified with the peak and bands of the Raman spectrum of Uwe et al. [86] for an undoped, unstrained sample of KTaO_3 in the same polarisation configuration.

III. - 6. Discussion

By comparing the spectrum of S2A (Fig. I-12) to that of S3B (Fig. I-13) under the same polarization conditions ($\Gamma_{1g} + \Gamma_{3g}$), we notice that the 280, 305 and 930 cm^{-1} peaks are related to the concentration of cobalt, being more intense in the more doped sample (S3B); these are the only peaks of concern to us. The intensities of the 280 and 305 cm^{-1} peaks decrease as the temperature increases (Fig. I-14 a to k); the intensity ratio of these two peaks would be slowly decreasing with increasing temperature if both were vibrational modes. Instead this ratio increases rapidly with T, showing that the 305 cm^{-1} peak intensity decreases more rapidly than that of the 280 cm^{-1} peak (Fig. I-15), the former disappearing entirely at room temperature (Fig. I-14k). The polarization measurements (Fig. 19a,b) show that the 280 cm^{-1} peak has predominantly the E_g symmetry and is induced by the Co^{2+} impurity, as stated by Wagner et al. [58]. In most systems, like $\text{MgO}:\text{Fe}^{2+}$ [93], the local modes are rarely observed and they only appear if they are in resonance with the lattice modes [18]. In MgO, the unperturbed phonon density of states has a tall peak at 280 cm^{-1} [48] which is the contribution of the acoustic modes from the Brillouin zone boundary; the 280 cm^{-1} impurity induced Raman mode could be such a resonance.

The behaviour of the 305 cm^{-1} peak with temperature and its disappearance before room temperature confirms that it is an electronic transition (Fig. I-14 a to k) coupled to phonons. Its polarization and energy demonstrate that it belongs to the ${}^4T_{1g}$ multiplet of Co^{2+} and we identify it as being the $\Gamma_{6g} \rightarrow \Gamma_{8g}^1$ electronic transition which agree also with Ralph et al. [51] who estimated that this transition is near 300 cm^{-1} from luminescence measurements.

Guha [23] identified both the 280 and 305 cm^{-1} peaks as vibrational modes despite his knowledge of the expected electronic levels of Co^{2+} in MgO . His incorrect temperature dependence for both these Raman peaks (he only showed one spectrum at 18°K) appears to be due to the inclusion of the two-phonon background in the measurement of the intensity. The subtraction of this contribution is essential so that the intensity variation of these peaks with temperature is more indicative of their nature; also the intensity of the 305 cm^{-1} as measured by him includes the overlapping contribution of the 280 cm^{-1} peak at that wavenumber.

Our temperature measurements also show that the 930 cm^{-1} peak is an electronic transition (Fig. I-14, l to m) and we assign this peak to the $\Gamma_{6g} \rightarrow \Gamma_{8g}^2$ transition of Co^{2+} . Guha [23] surmised correctly that this peak must belong to Co^{2+} ; this peak intensity exceeds considerably the two-phonon background and the behaviour of the intensity of this peak (in

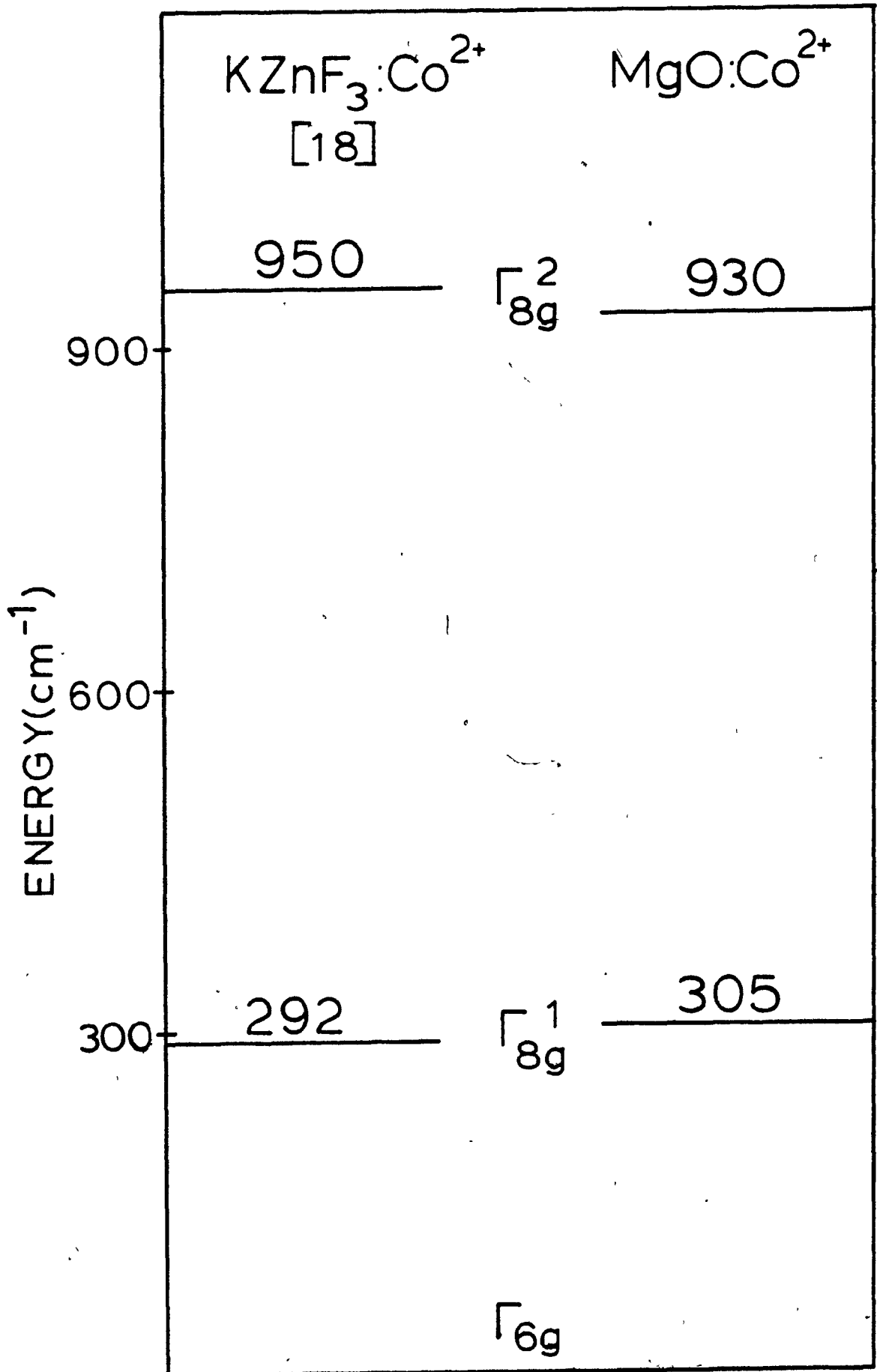
his analysis) was indicative of its electronic origin.

For divalent cobalt at an octahedral site in a comparable crystal, the position of the electronic levels will be close to our experimental values, slight differences being due to the difference in the value of the crystal field. We searched for these electronic levels in $\text{NaCl}:\text{Co}^{2+}$ and $\text{KTaO}_3:\text{Co}^{2+}$ but the expected regions were masked by the two-phonon spectra. Lockwood et al.[18] observed by Raman spectroscopy the electronic levels of cobalt in $\text{KZnF}_3:\text{Co}^{2+}$ and found the $\Gamma_{6g} \rightarrow \Gamma_{8g}^1$ at 292 cm^{-1} and the $\Gamma_{6g} \rightarrow \Gamma_{8g}^2$ transition at 950 cm^{-1} . Like us, they have not found the $\Gamma_{6g} \rightarrow \Gamma_{7g}$ transition which is obviously a weak transition. In agreement with theory, the position of the Co^{2+} levels in these two compound (KZnF_3 and MgO ; see Fig.I-21) are similar which supports our analysis.

We calculated the theoretical position of the Co^{2+} spin-orbit levels (to second-order) and found excellent agreement with our experimental values when the dynamical Jahn-Teller interaction includes the coupling to E_g and T_{2g} modes. We note that the T_{2g} mode coupling is essential in the analysis. Ray et al[33] neglected this coupling on the basis of the value of the coupling constant ratio $|V_e|/|V_t|$ calculated using the free-ion values of the radial integrals ($\langle r^D \rangle$); this ratio is a function of $\langle r^2 \rangle / \langle r^4 \rangle$. It is known [33] that the expansion of the 3d radial functions in a crystal will decrease the value of $\langle r^2 \rangle / \langle r^4 \rangle$ (compared to the free-

Fig. I-21. Energy levels of Co^{2+} at an octahedral site

We present the observed electronic transitions of the divalent cobalt impurity at an octahedral site measured by Raman spectroscopy. On the left are the results of Lockwood et al. [18] for $\text{KZnF}_3:\text{Co}^{2+}$ and on the right are our experimental results for $\text{MgO}:\text{Co}^{2+}$.



ion value) and thus decrease the estimated $|V_e|/|V_t|$. In addition their analysis tried to explain the position of only the Γ_{8g}^1 level (deduced from magnetic susceptibility measurements [49]) and did not predict the position of the Γ_{8g}^2 and Γ_{7g} levels (positions unknown at the time). We estimate that the $\Gamma_{6g} \rightarrow \Gamma_{7g}$ transition will be in the 980 to 1010 cm^{-1} region for values of $a = 0.935$ and $0.97 \leq k \leq 1.00$. Its energy is independent of k' (covalency parameter of the $^4T_{2g}$ state) and the Jahn-Teller interaction (the Γ_{6g} and Γ_{7g} levels are Kramers' doublets); its experimental position would fix the value of k (Equ. I-16c) and its separation from the Γ_{8g}^2 would be indicative of the influence of the upper levels.

IV.- CONCLUSION

We observed, for the first time, the electronic transitions within the $4T_{1g}$ crystal field ground manifold of divalent cobalt in MgO by Raman spectroscopy. First-order Raman scattering is forbidden in a crystal for which each site is a center of inversion and this fact enhances the second-order (two-phonon) scattering; the substitution of an impurity at those sites breaks the translation symmetry and can induce local vibrations that can be observed by Raman spectroscopy. In addition, the electronic transitions of the impurity can also be present in the spectrum. In the case of $MgO:Co^{2+}$, the two-phonon structure is very extended and covers the region from the laser line to beyond 1200 cm^{-1} ; in certain polarisations, the electronic transitions have similar intensities to the phonon-related peaks (Fig. I-9b and I-13) and are thus lost in the phonon spectrum or the peaks are misinterpreted. [21].

Our polarisation and temperature spectra clearly show that the 280 cm^{-1} peak is an E_g local vibrational mode in accordance with Wagner et al. [58] neutron diffraction results. This mode could be resonant with the acoustic lattice modes at the surface of the Brillouin zone, which form the first peak (near 280 cm^{-1}) in the phonon distribution function [48]. The disappearance of the 305 and 930 peaks at room temperature (19°C) confirms their electronic nature.

These peaks are the $\Gamma_{6g} \rightarrow \Gamma_{8g}^1$ transition at 305 cm^{-1} and the $\Gamma_{6g} \rightarrow \Gamma_{8g}^2$ transition at 930 cm^{-1} ; these values correspond fairly well to results of our calculation of the position of the electronic levels of a $3d^7(\text{Co}^{2+})$ impurity in an octahedral site with spin-orbit to second-order included. They are also in agreement with the values measured by Lockwood et al. [18] for Co^{2+} in a similar system ($\text{KZnF}_3:\text{Co}^{2+}$). Neither they nor we, have seen the $\Gamma_{6g} \rightarrow \Gamma_{7g}$ transition because it is lost in the two-phonon bands and presumably is weak. The knowledge of its position with respect to the Γ_{6g} ground state would fix the value of k (covalency parameter of $^4T_{1g}$) and its separation from the Γ_{8g}^2 would inform us of the influence of the upper excited states. Using a suitable dye laser, it might be possible to observe this transition ($\Gamma_{6g} \rightarrow \Gamma_{7g}$) by resonant Raman spectroscopy.

To account for the difference between the calculated spin-orbit levels (to second-order) and the observed electronic levels of Co^{2+} in MgO , we calculated the dynamical Jahn-Teller interaction with coupling to both E_g and T_{2g} modes, the coupling to the latter being essential for complete agreement. The Co^{2+} in MgO is a relatively weak Jahn-Teller ion; its Jahn-Teller stabilization energy for equal coupling to the E_g and T_{2g} modes is 12 cm^{-1} .

PART IIVIBRATIONAL RAMAN
SPECTROSCOPY OF β -In₂Se₂

INTRODUCTION

Indium selenide (In_2Se_2) is a semiconductor, member of the large family of layer structure compounds. They have highly anisotropic bonding forces. The intralayer forces are mainly covalent but sometimes are ionic while the inter-layer forces are van der Waals. The individual layers can easily slide over each other to produce different relative arrangements of the successive layers which lead to the existence of a number of polytypes for a single compound and also to stacking faults.

The knowledge of the phonon frequencies and their species is important for analysing phase transition, two phonon spectra and many transport properties especially for an anisotropic semiconductor. Jandl and Carlone reported a Raman spectrum showing most of the vibrational peaks in addition to unexpected high frequency peaks. Upon their request we studied this compound using the red lines (14781 and 15454 cm^{-1}) of the Kr^+ laser in the hope of observing the layer to layer shear mode which they did not observe and to see if the transitions in the 400 cm^{-1} region were Raman active.

CHAPTER I - THEORY

I. 1 - Probability of Transition

The transition probability for the Stokes spectrum when only one phonon participates is proportional to six terms differing in the order of the interactions. The following expression is the term where the electron-phonon interaction (H_{ep}) operates between two intermediate states [4]:

$$P \propto I_0 \left| \sum_{a,b} \frac{\langle n_0+1; 0 | H_{er} | a \rangle \langle a | H_{ep} | b \rangle \langle b | H_{er} | n_0; 0 \rangle}{(\omega_1 - \omega_a)(\omega_1 - \omega_b)} \right|^2 \delta(\omega_1 - \omega_s - \Omega) \quad (II-1)$$

with I_0 the intensity of the laser beam of frequency ω_1 , $\pi\omega_a$ and $\pi\omega_b$ the energies of the intermediate states; the initial and final electronic parts are the ground state and n_0 is the occupation number of the phonon. The other matrix elements are for the electron-radiation interaction (H_{er}) for absorption (left) and emission (right). The delta function ensures the conservation of energy with $\Omega = \omega_1 - \omega_s$ being the frequency of the phonon emitted. The correspondence with Fig. I-1 (in part I) is $E_0 = |n_0; 0\rangle$, $E_1 = |n_0+1; 0\rangle$ and E_2 to E_n are the a and b intermediate states.

The transitions (absorption and emission) are mostly electric-dipole; the other types of multipole transitions are many orders of magnitude weaker. One important selection rule is the conservation of crystal momentum (Stokes):

$$\pi \vec{q}_1 = \pi \vec{q}_s + \pi \vec{k} + \pi \vec{G} \quad (II-2)$$

with \vec{q} the wave-vector of the incident (i) and scattered (s) photons, \vec{k} the wave-vector of the phonon and \vec{G} the reciprocal lattice vector. The energies of the incident and scattered photons do not differ by much (the phonon frequencies are small compared with the incident photon frequency), then their wave-vectors are almost equal in magnitude and are much smaller than the dimension of the first Brillouin zone. For relation II-2 to be satisfied, we need $\vec{G} = 0$ and the phonons participating in the scattering are limited to optical modes near the center of the zone ($\vec{k} \approx 0$).

Two phonons can contribute to Raman scattering with the following selection rule:

$$\vec{k}_1 + \vec{k}_2 \approx N\vec{G} \quad (N \geq 0; \text{integer}) \quad (\text{II-3})$$

In this case, the phonons are not restricted to the center of the zone and will mostly come from points of high symmetry in the zone; acoustic modes can now participate in the scattering. We call this the second-order Raman effect because it needs an additional transition and is less probable than the first-order effect; an example of this effect appeared in the spectra of $\text{MgO}:\text{Co}^{2+}$ (Part I).

I. 2 - Crystal Structure of the In₂Se₂ Polytypes

Before giving the modes that are active in the first-order Raman scattering, we need to know the crystal structure of indium selenide (In₂Se₂). Each layer of the compound is formed by the superposition of four monoatomic sheets in the sequence Se-In-In-Se. An indium atom is covalently bonded to another indium and three selenium atoms each of which is bonded to three indium atoms (Fig. II-1) forming an hexagonal unit cell of space group D_{3h}^1 ($P\bar{6}m2$).

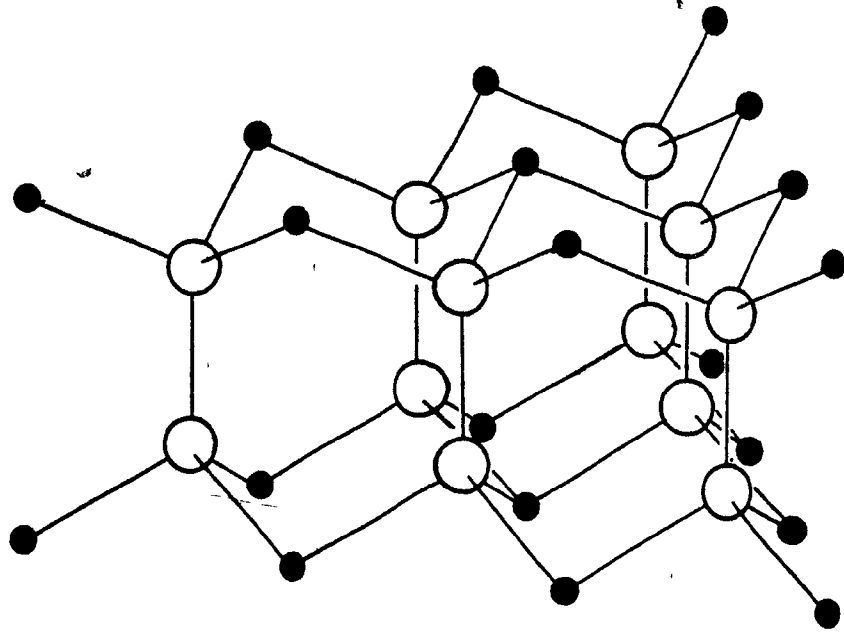
In addition, each layer is weakly bonded by Van der Waals forces to an adjacent identical layer and the ordered stacking is called a polytype. Indium selenide is known to present itself in three polytypes identified as β , ϵ and γ .

The stacking sequence for the β -type is formed by two identical layers (Fig. II-2), one being rotated about the In-In bond axis of one layer, and slightly shifted so that the In-In bond of one layer is in line with the selenium atoms of the other layer. We can also represent the stacking sequence as one layer being translated along the edge of the unit cell from A to B or B to A (Fig. II-2) and then rotated by 60° about the edge axis: these operations correspond to the screw axis. That structure has a center of inversion between the layers and the space group is D_{6h}^4 ($P6_3/mmc$).

The ϵ -type is formed by stacking two identical layers, one being slightly shifted so the In-In bond of the top layer

Fig. II-1. Structure of one layer of indium selenide [59].

The space group of the layer is given in Schoenflies notation with the International symbol in parenthesis.



O - In

● - Se

Space group: D_{3h}^1 ($P\bar{6}m2$)

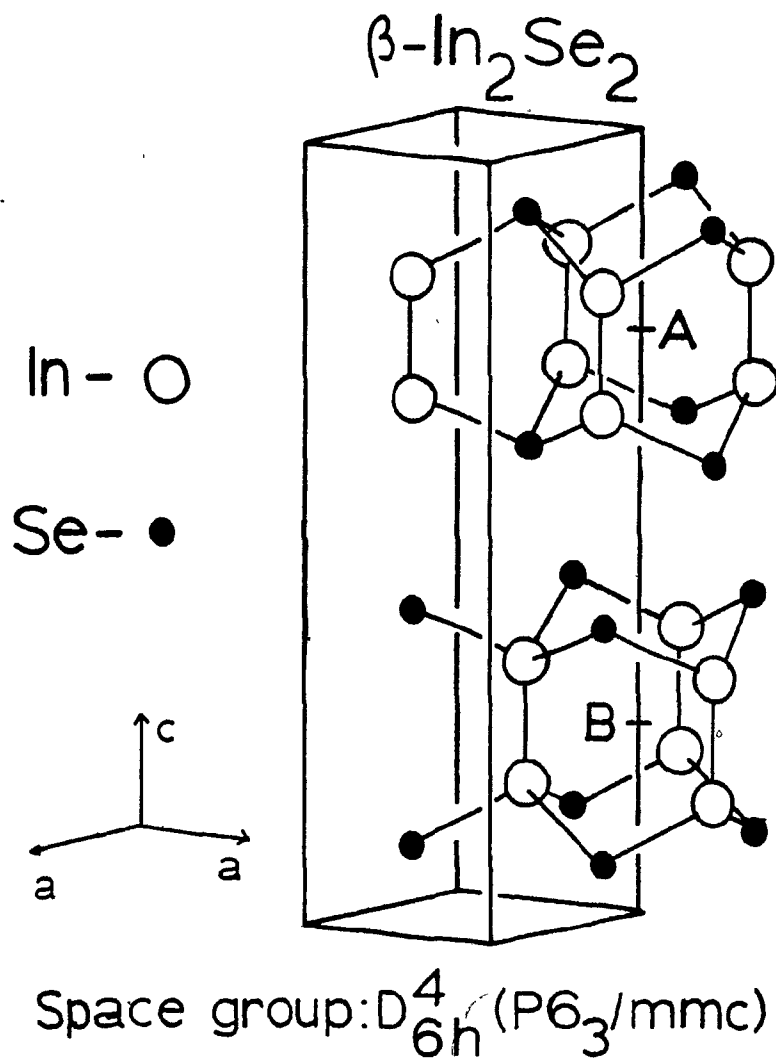


Fig. II-2. Stacking sequence of $\beta\text{-In}_2\text{Se}_2$ [60].

The unit cell contains two molecules of In_2Se_2 and has the dimensions $a = 4.0 \text{ \AA}$ and $c = 16.8 \text{ \AA}$.

The A and B points are explained in the text.

of the unit cell is aligned with the selenium atoms of the next layer while the selenium atoms of the first layer and the indium atoms of the second layer are aligned with empty spaces in the unit cell (Fig. II-3a). The space group of this structure is $D_{3h}^1(P\bar{6}m2)$. The γ -type spans three layers with the first and second, and the second and third layers positioned like the ϵ -type (Fig. II-3b); its space group is $C_{3v}^5(R3m)$. The unit cell for each polytype contains one formula (In_2Se_2) per layer; the space groups were given in the Schoenflies notation with the International notation in parenthesis (see Appendix E).

I. 3 - Group Theory of the Phonon Modes

For the β polytype, the unit cell spans two layers and includes eight atoms; with three degrees of freedom for each atom, there will be 24 normal modes of vibration at the center $\Gamma(\vec{k} = 0)$ of the Brillouin zone. These modes decompose into irreducible representations of the point group D_{6h} [39,62]

$$\Gamma \equiv 2A_{1g} + 2B_{2g} + 2E_{1g} + 2E_{2g} + 2A_{2u} + 2B_{1u} + 2E_{1u} + 2E_{2u} \quad (II-4)$$

The B_{2g} , B_{1u} and E_{2u} modes are optically inactive, the A_{2u}^1 and E_{1u}^1 are acoustic vibrations while the A_{2u}^2 and E_{1u}^2 are infrared active. The remaining six non-degenerate modes (A_{1g} , E_{1g} , E_{2g})

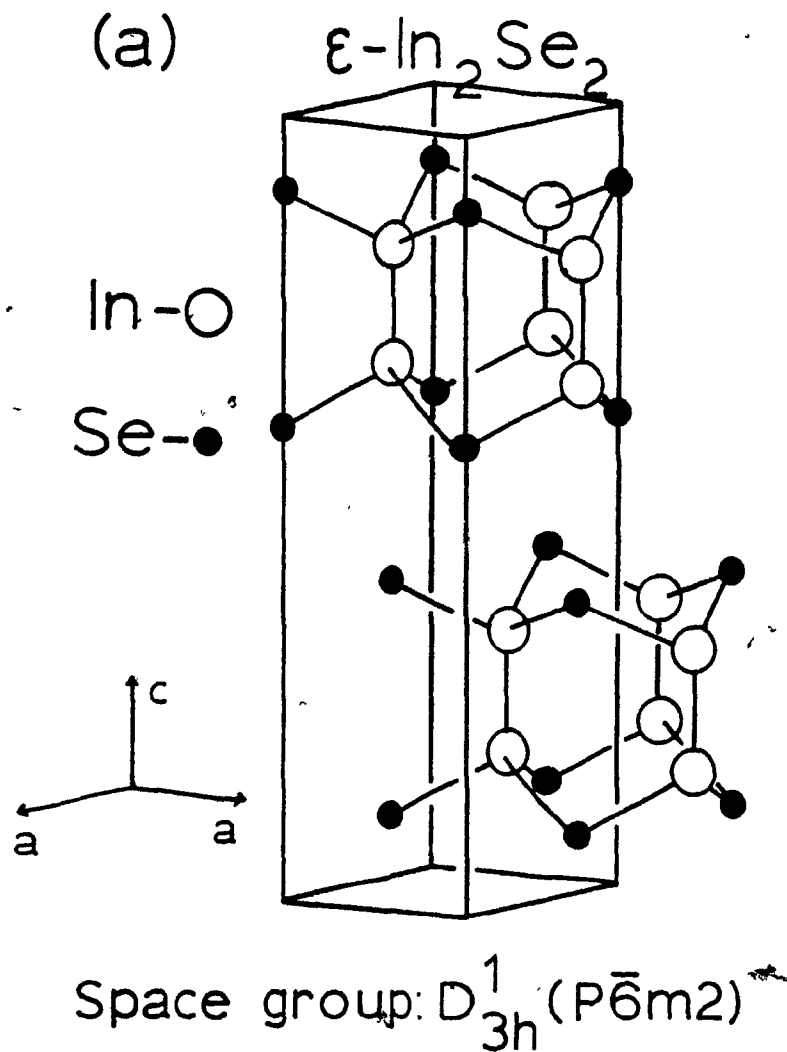
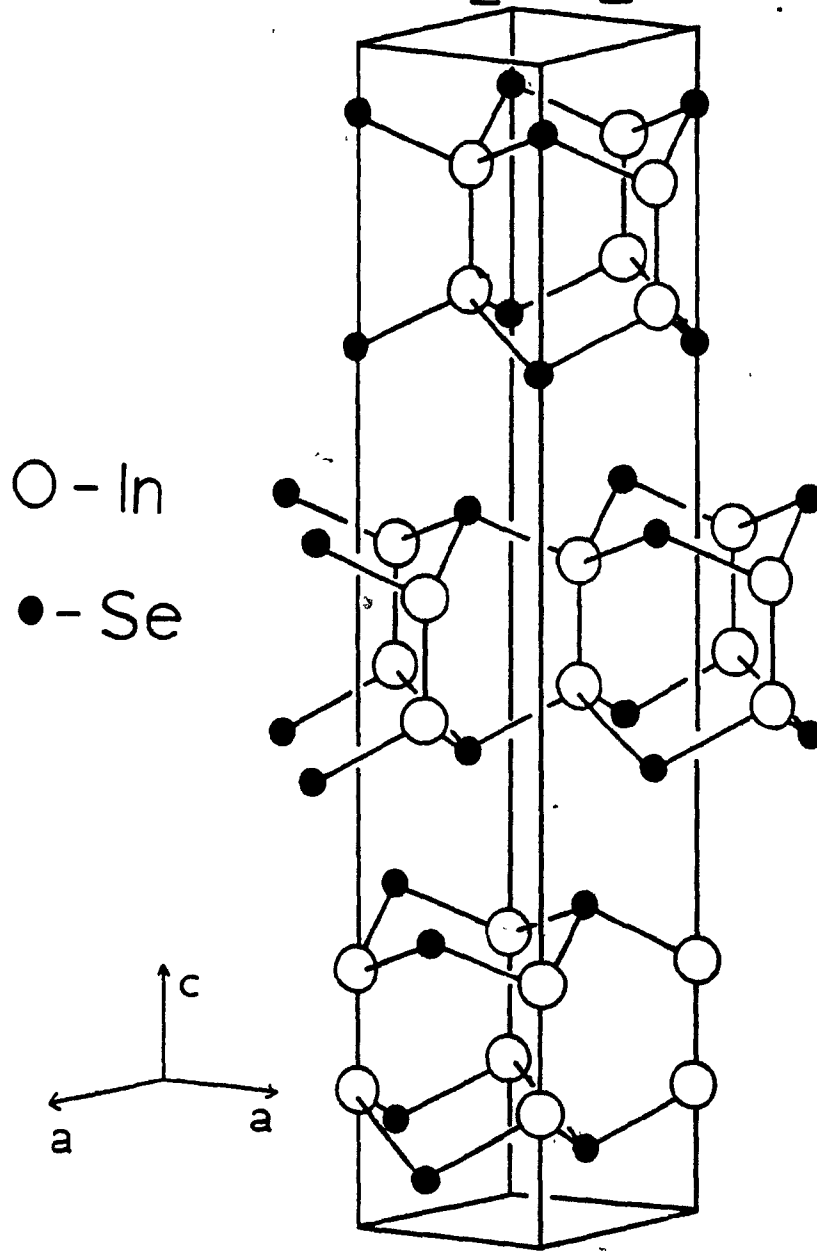


Fig. II-3. Stacking sequence of ϵ - and γ - In_2Se_2 .

- a) The unit cell of $\epsilon\text{-In}_2\text{Se}_2$ contains two molecules of In_2Se_2 ($a = 4.0 \text{ \AA}$; $c = 16.9 \text{ \AA}$).
- b) The unit cell of $\gamma\text{-In}_2\text{Se}_2$ contains three molecules of In_2Se_2 ($a = 4.0 \text{ \AA}$; $c = 25.32 \text{ \AA}$).

(b) $\gamma\text{-In}_2\text{Se}_2$ Space group: C_{3v}^5 (R3m)

are Raman active. The basis functions for the last three representations are (x^2+y^2) or z^2 for A_{1g} , yz and xz for E_{1g} and, (x^2-y^2) and xy for E_{2g} . This structure contains an inversion center and the Raman and infrared modes are mutually exclusive.

For completeness we present a similar treatment for the other polytypes. The ϵ polytype also spans two layers with eight atoms but now the 24 normal modes decompose into the irreducible representations of the point group D_{3h} [61].

$$\Gamma \equiv 4A_1' + 4A_2'' + 4E' + 4E'' \quad (\text{II-5})$$

of which 3 are strictly infrared active ($3A_2''$), 8 are only Raman active ($4A_1'$ and $4E''$) while 3 are both infrared and Raman active; this gives a total of 11 non-degenerate Raman modes. The functional basis for the Raman modes are (x^2+y^2) or z^2 for A_1' , (x^2-y^2) and xy for E' and, yz and xz for E'' .

The γ polytype is composed of three layers but the rhombohedral primitive cell only contains four atoms (all members of the same layer); the 12 normal modes decompose into the irreducible representation of the point group C_{3v} [84a,61].

$$\Gamma \equiv 4A_1 + 4E$$

All the optical modes are both infrared and Raman active, and there are 6 non-degenerate Raman modes ($3A_1$ and $3E$). The functional basis for these modes are (x^2+y^2) or z^2 for A_1 and

either $(x^2 - y^2)$ and xy or yz and xz for E.

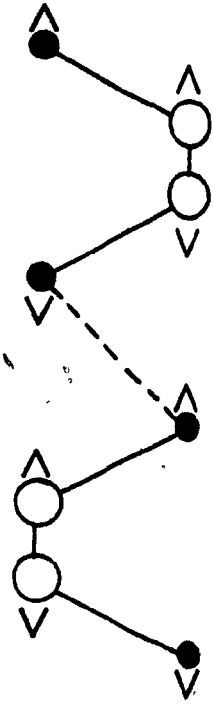
In Fig. II-4 we present the atomic displacements in the unit cell, for the Raman active modes of the β polytype (for ϵ - and γ - types see Ref. 61). The functional basis for the irreducible representations of the Raman modes for the different structures can be related to the direction of the electric field of the incident and the scattered photons, if x , y and z correspond to the crystallographic axes. In Eq. II-1, the matrix elements can be analysed using group theory; to render this more simple we can reduce the three matrix elements into one by using the fact that the electronic part of the initial and final states is the ground state and supposing that the vibrational part of the initial state is the zero-phonon ground $|n_0 = 0\rangle$ which is a reasonable assumption when the experiment is performed at low temperature. We can also neglect the intermediate electronic states which can be any representations of the group that satisfy the electric dipole selection rule. The electron-phonon interaction representation is dependent on the phonon created and so is included in the final phonon state; the representation of the electron-radiation interaction is the electric dipole operator (\vec{r}) and will appear twice for the process [63]. The matrix element is now given in terms of the following direct product:

$$\langle n_0 = 1 | (\vec{E}_i \cdot \vec{r}) (\vec{E}_s \cdot \vec{r}) | n_0 = 0 \rangle \equiv \Gamma_p \times \Gamma_u \times \Gamma_u \times \Gamma_1 \quad (\text{II-7})$$

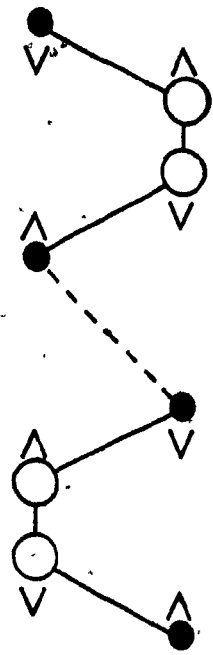
()

Fig. II-4. Raman active modes of β -In₂Se₂ [62].
The dashed line corresponds to the Van der Waals
bond between layers; the arrows indicate the
direction of the displacement for each atom.

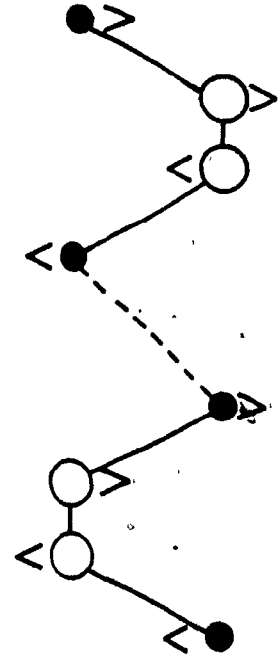
O



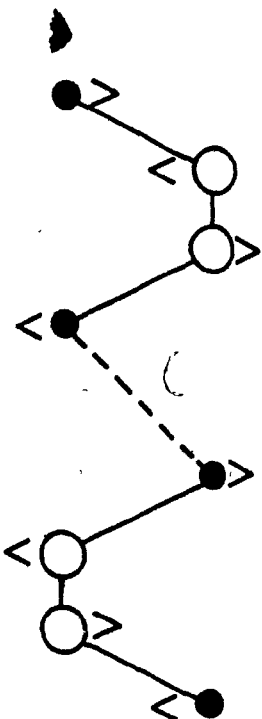
A_{1g}^1



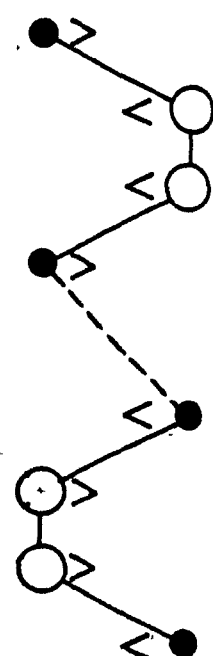
A_{1g}^2



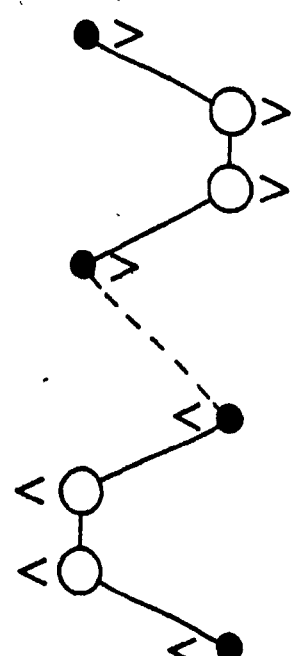
E_{1g}^1



E_{1g}^2



E_{2g}^1



E_{2g}^2

where \vec{E}_ν is the electric field of the light ($\nu = i, s$). The phonon ground state is the totally symmetric representation Γ_1 and Γ_u is the electric dipole representation; because $\Gamma_j \times \Gamma_1 = \Gamma_j$ we will look at the product of the first three terms. For this matrix element to be non-zero, we need to have the Γ_1 representation included in the reduction of the triple direct product. For any representation Γ_j , the representation Γ_1 is included in the symmetrical product $[\Gamma_j \times \Gamma_j]$ and, if Γ_p is included in the reduction of $[\Gamma_u \times \Gamma_u]$, then the matrix element is non-zero. The symmetrical product of the representations Γ_u of the electric dipole gives the polarisability representations which are by definition Raman active; the polarisability behaves like the electric quadrupole moment. This analysis permits one to find the polarisation of the incident and scattered light for specific types of phonons.

CHAPTER II - RESULTS AND ANALYSIS

II. 1 - Information on the Samples

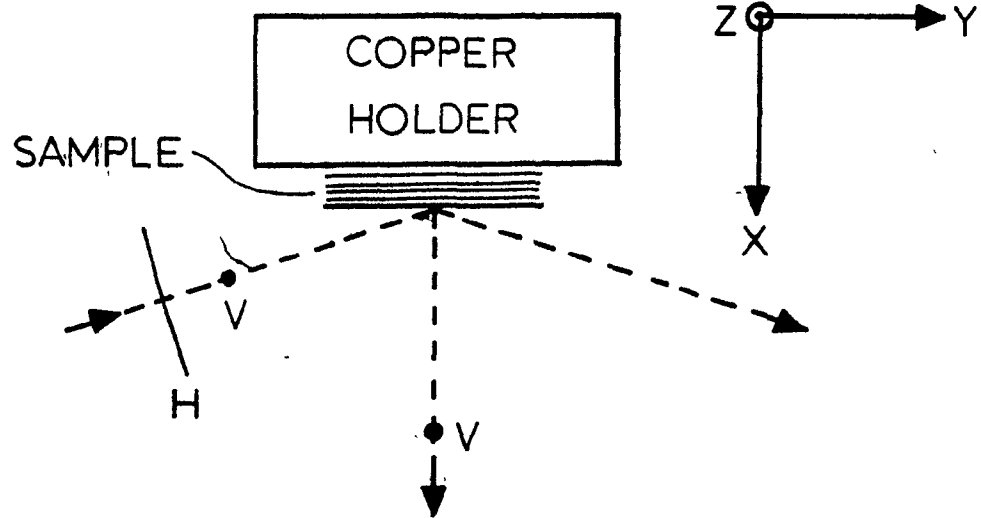
Our sample of indium selenide was grown by the Bridgman technique by Dr. S. Jandl, Département de Physique, Université de Sherbrooke. With the aid of a 20X microscope, the scattering surface was prepared by lifting thin cleavage flakes. The sample used in the Raman measurement was also studied with an X-Ray precession camera by Dr. Gabrielle Donnay, Department of Geological Sciences, McGill University. The sample was identified as the β -polytype of In_2Se_2 [64] and showed some twinning. A backscattering von Laue picture of our sample showed a hexagonal pattern made up of a multitude of slightly shifted points: the c axis of each layer is pointing in slightly different directions and so the sample is non-uniform.

The sample was oriented (Fig. II-5) with its long dimension at approximately 45° with respect to the horizontal laboratory direction; in this orientation we obtained good spectra. The incident laser beam hits the sample at a grazing incidence with the vertical polarisation inside the crystal in the plane of the layers, while the horizontal polarisation within the crystal being mainly parallel to the z (c) axis. The scattered light was analysed in the vertical polarisation using 50 to 1 sensitivity of the double-monochromator for this polarisation direction. Because our sample has twinning and is non-uniform (not a single crystal) we could

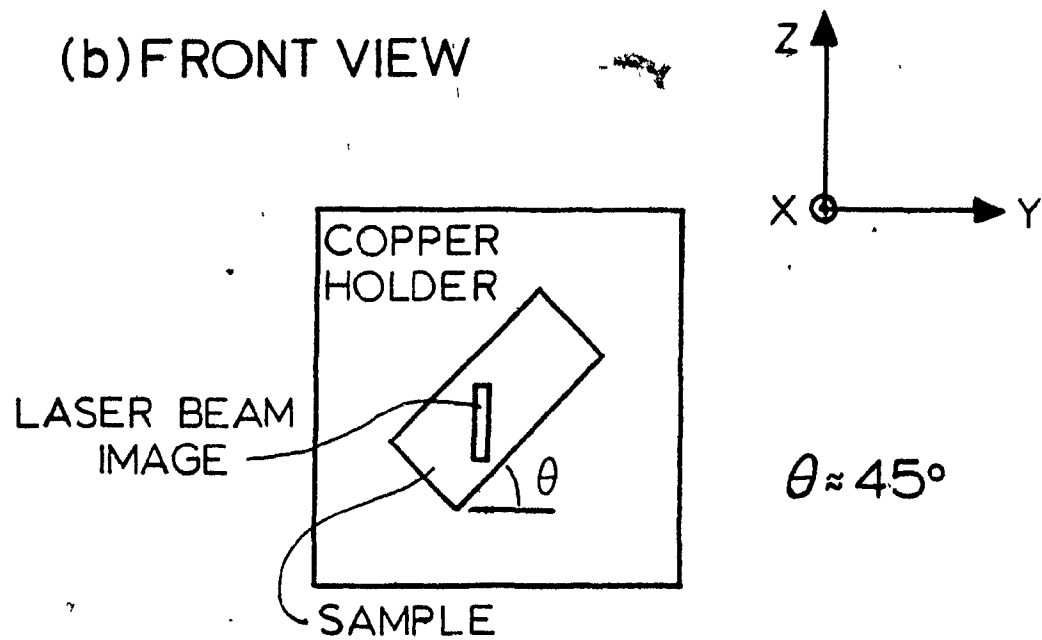
Fig. II-5. Orientation and polarisation of the sample.

The orientation of the $\beta\text{-In}_2\text{Se}_2$ sample with respect to the laboratory axes in the top view (a) and in the front view (b); the different polarisations permissible are given in (a). (V: vertical; H: horizontal). The room temperature spectra (Fig. II-9) were done with the long dimension of the sample, vertical.

(a) TOP VIEW



(b) FRONT VIEW



not make any group theoretical analysis of the symmetry of the phonons. With this in mind, we looked in the literature for other systems having the same structure.

II. 2 Comparison with Equivalent Systems

We present in Figs. II-6 and II-7 the Raman spectra of Irwin et al. [65] for the isostructural compounds Ga_2S_2 and Ga_2Se_2 ; the irreducible representation and Raman shift are given for each peak. The z axis corresponds to the c axis of their samples; for the upper trace of Ga_2S_2 (Fig. II-6), the incident beam is in the x direction with the y polarisation while the scattered light is in the z direction with the y polarisation (Porto's notation). Analysing the features of their spectra (see Table II-1) we find that the E_{2g}^2 modes are almost equal (Ga_2S_2 : 22.0cm^{-1} ; Ga_2Se_2 : 19.5cm^{-1}); that mode corresponds to the out of phase vibration of two consecutive layers in a plane perpendicular to the c axis and would only depend on the van der Waals forces between the layers, then we can expect the value for indium selenide to be close to 20cm^{-1} . Because the mass of the selenium atom is larger than the mass of the sulphur atom, the frequencies of all the modes are lower; then using a similar argument for the mass of the indium atom as compared to the mass of the gallium atom we can expect the frequencies of the modes to be lower than those of gallium selenide. Another important

Fig. II-6. Raman spectra of β -Ga₂S₂.
Irwin et al [65] used the 19436 cm⁻¹ line
(514.5 nm) of an argon ion laser to make
these spectra at room temperature (293°K);
the Z axis is parallel to the c axis of the
crystal. A filter was used to remove the
plasma lines.

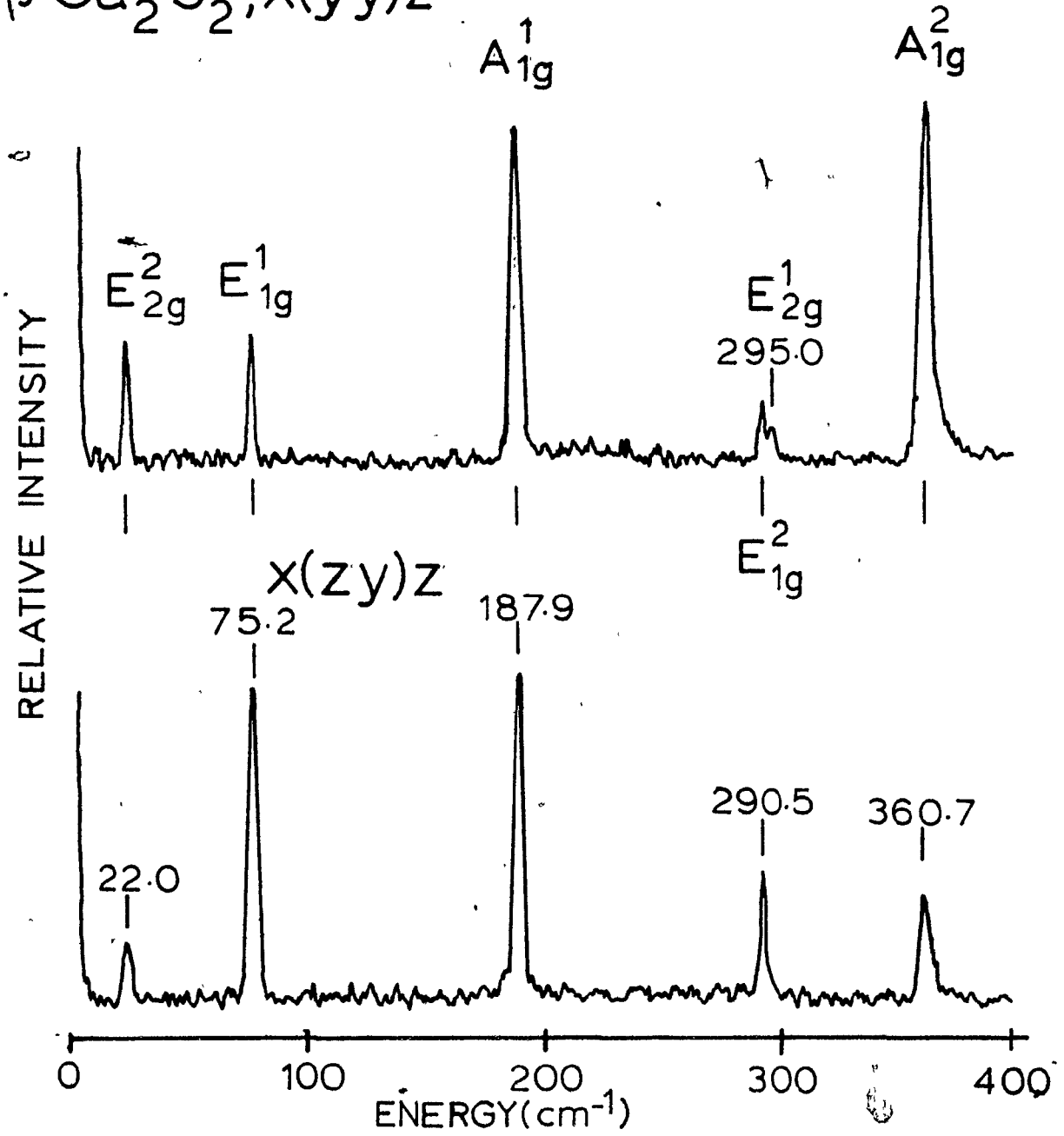
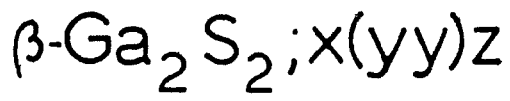


Fig. II-7. Raman spectra of β -Ga₂Se₂.

Irwin et al [65] used the 16119 cm⁻¹ (620.4 nm) line of an helium-neon laser with the crystal at 77°K and no filter. The Z axis is parallel to the c axis of the crystal. The peak at 252.1 cm⁻¹ is due to the presence of the ϵ -polytype.

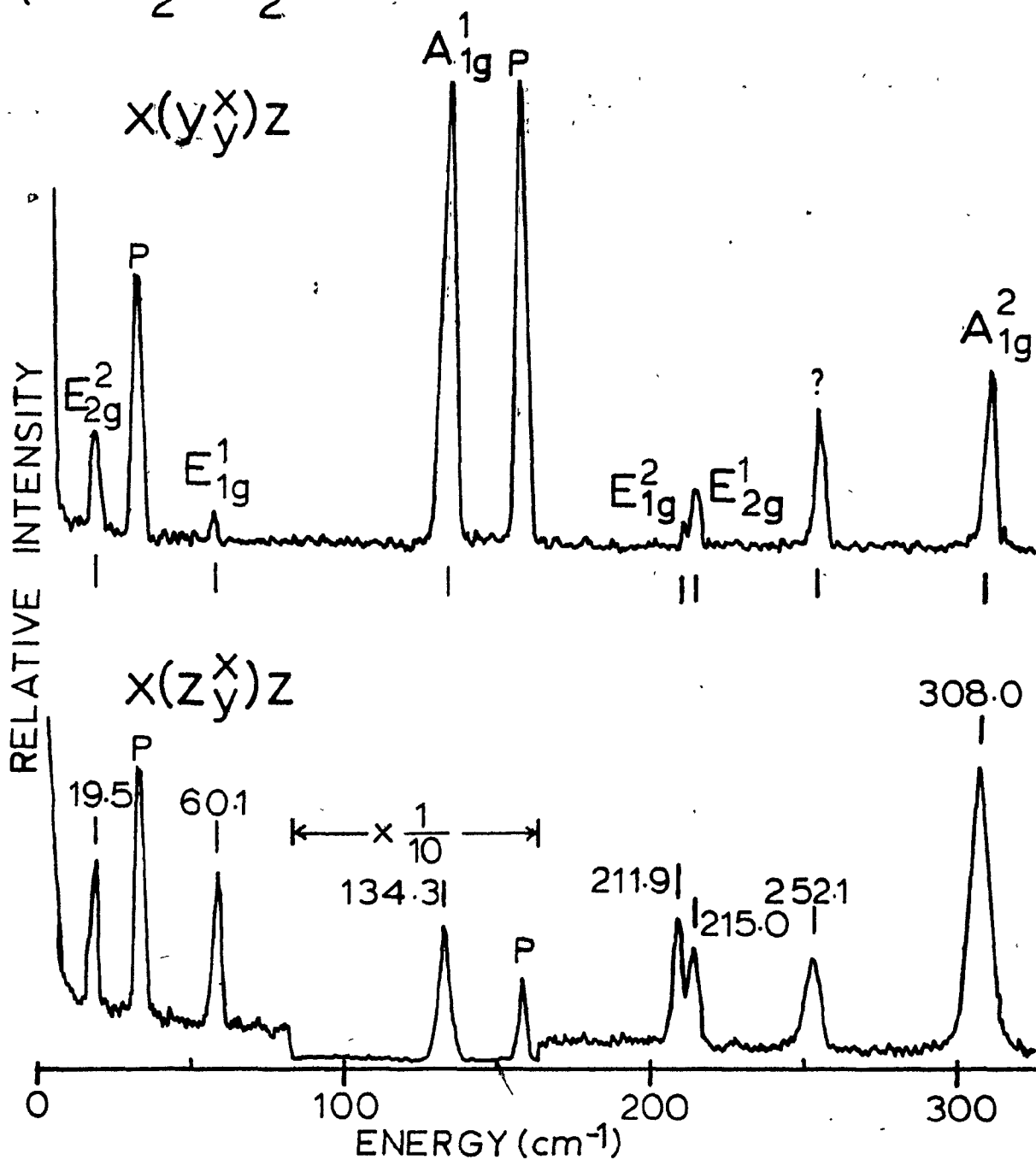
$\beta\text{-Ga}_2\text{Se}_2$ 

Table II-1. Vibrational modes of $\beta\text{-Ga}_2\text{S}_2$
and $\beta\text{-Ga}_2\text{Se}_2$.

Values of the vibrational peaks taken from figures II-6 and II-7 with their respective i.r. in D_{6h} (for notation of the i.r. see Table E-II.B).

TABLE II-1

ir.	$\beta\text{-Ga}_2\text{S}_2$	$\beta\text{-Ga}_2\text{Se}_2$
E_{2g}^2	22.0 cm^{-1}	19.5 cm^{-1}
E_{1g}^1	75.2	60.1
A_{1g}^1	187.9	134.2
E_{1g}^2	290.5	211.9
E_{2g}^1	295.0	215.0
A_{1g}^2	360.7	308.0

feature in their spectra is the presence of a doublet around 290 cm^{-1} (215) for $\text{Ga}_2\text{S}_2(\text{Ga}_2\text{Se}_2)$; the separation between the partners of the doublet gets smaller as the mass of one constituent gets larger ($\text{Ga}_2\text{S}_2: 4.5 \text{ cm}^{-1}$; $\text{Ga}_2\text{Se}_2: 3.1 \text{ cm}^{-1}$). We should expect to find a similar doublet at a comparatively equivalent position in our spectra, with a small separation.

Most of these features can be seen in Fig. II-8 (a and b). The doublet feature can be inferred from the fact that the full width at half-maximum of the 180 cm^{-1} band is larger than that of the other peaks (plasma lines excluded); the measured separation follows the trend of the preceding compounds. With this interpretation, the total number of lines seen is six, which is consistent with the β -type. The irreducible representation (i.r.) of the peaks is based on the data of Irwin et al. [65] for the isotypic $\beta\text{-Ga}_2\text{S}_2$ and the result of the next section. P

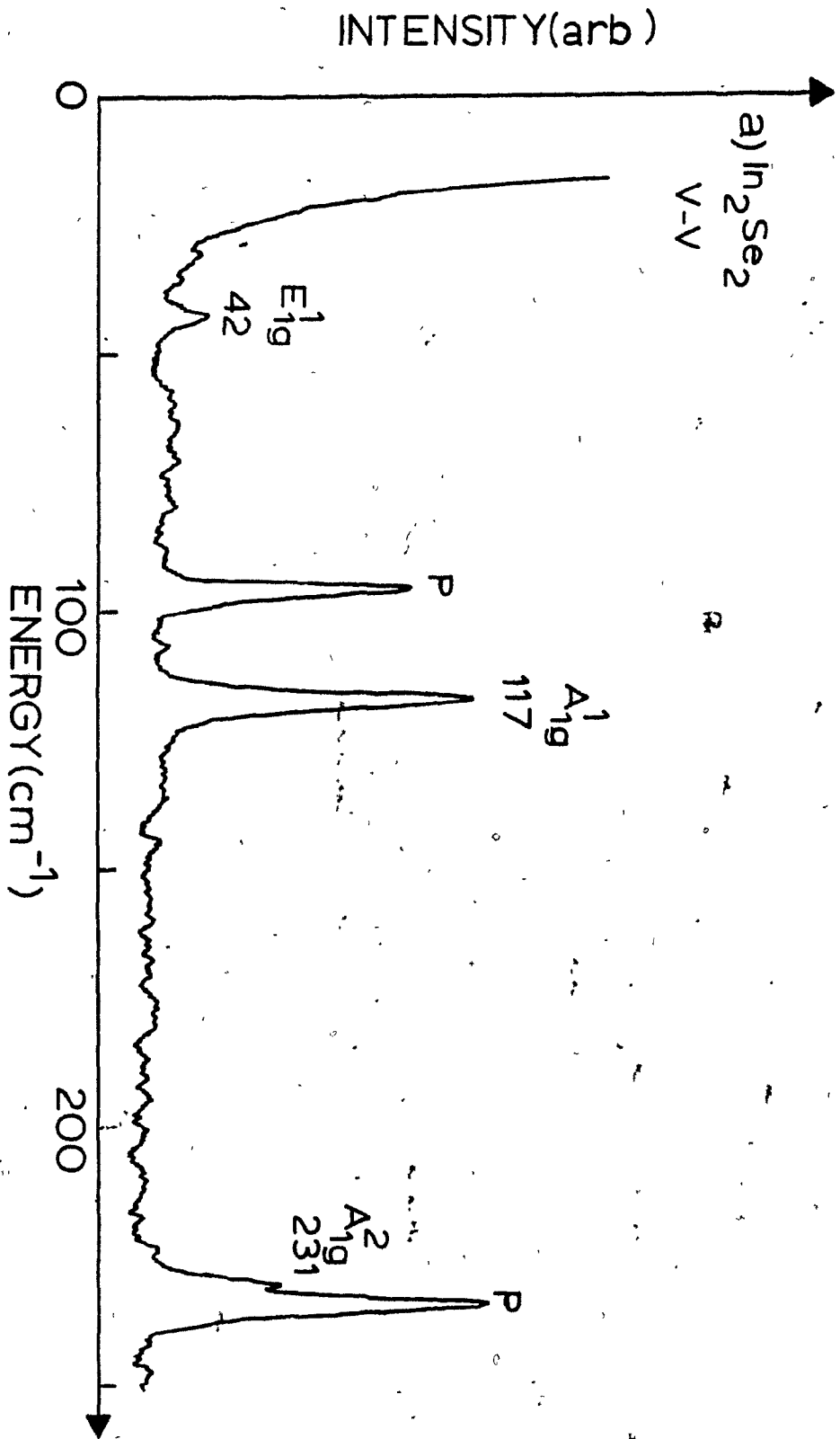
The spectra of $\beta\text{-In}_2\text{Se}_2$ (Fig. II-9) at room temperature with a different laser line (14781 cm^{-1}) proves that the peaks seen at low T are vibrational Raman peaks; within the accuracy of the position of the peaks ($\pm 2 \text{ cm}^{-1}$), the doublet is unresolved.

Fig. II-8. Stokes Raman spectra of β -In₂Se₂.

We used 200 mW of power from the 15456 cm⁻¹ line of the krypton ion laser. The slit width is 2.5 cm⁻¹ and the error on the value of the shifts is ± 1 cm⁻¹. The sensitivity of the photon counter was 100 counts/sec. (full scale) with a time constant of 4.7 sec and a scan rate of 10 cm⁻¹/min were in superfluid helium and the scattering surface was deduced to be near 100°K.

a) Stokes Raman spectrum with the incident and scattered light polarized vertically (V); a neutral density filter of 0.3 was present in the incident beam.

b) Stokes Raman spectrum with the incident light polarized horizontally (H) and the scattered light polarized vertically (V).



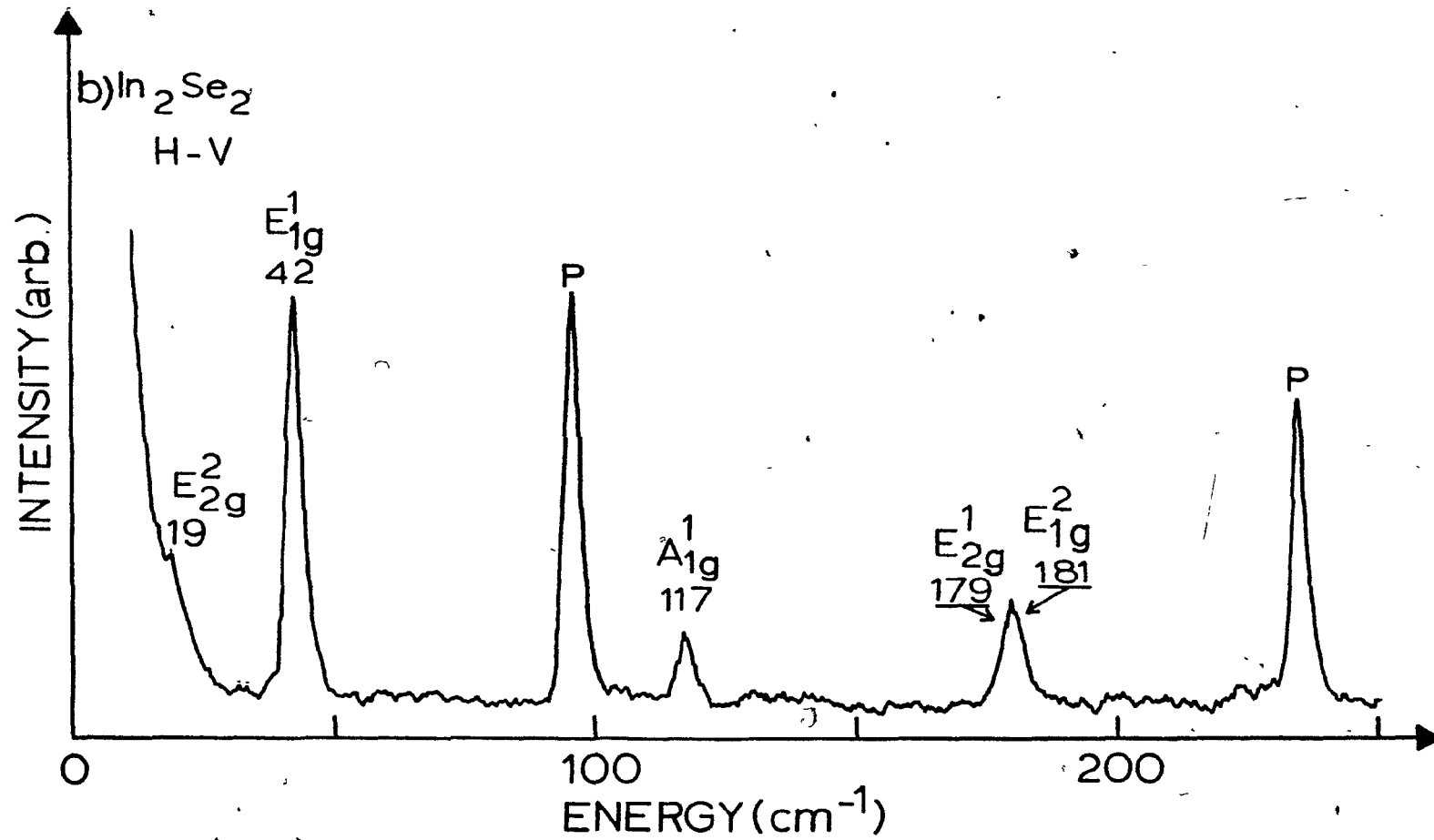
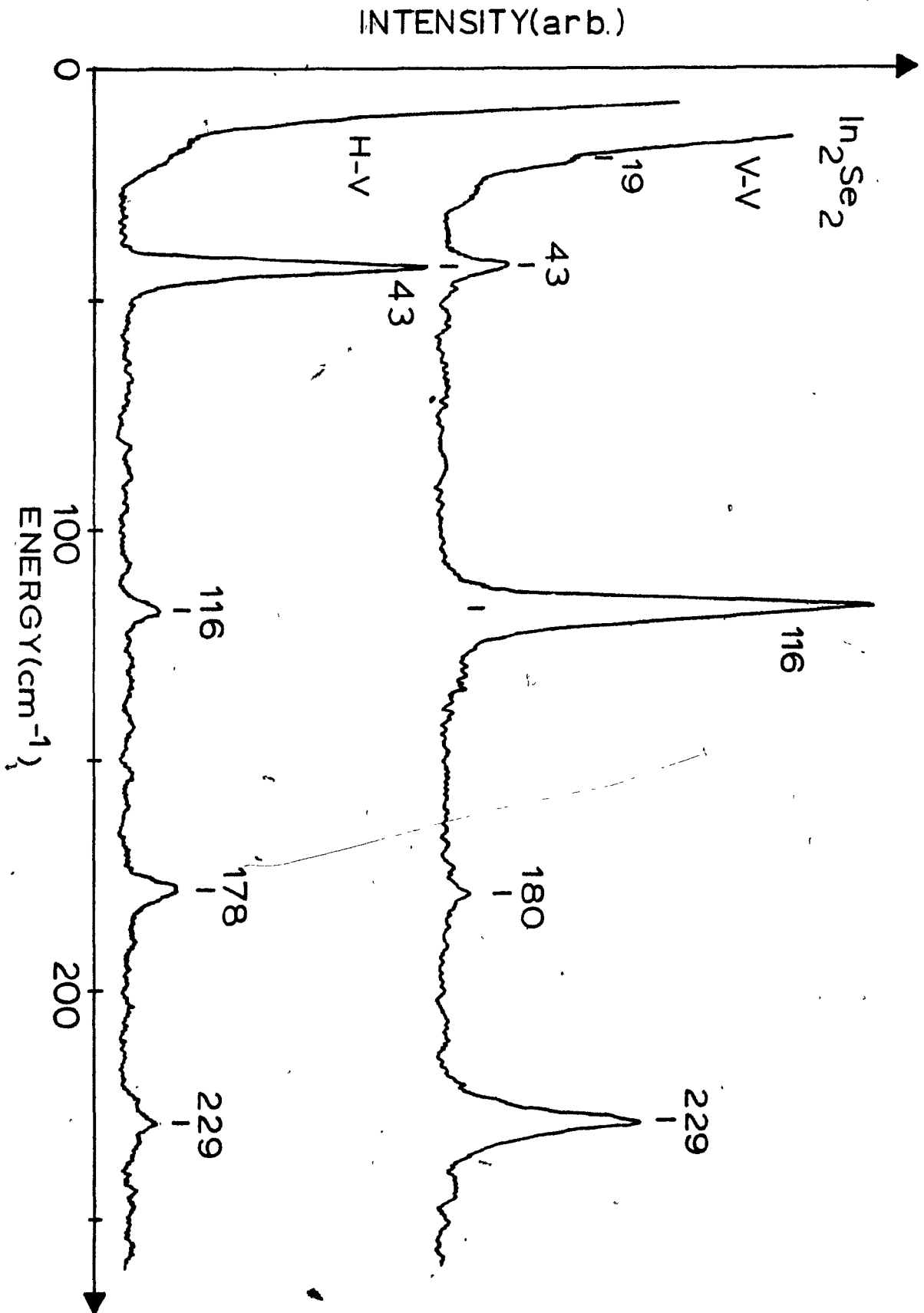


Fig. II-9. Spectra of $\beta\text{-In}_2\text{Se}_2$ with $L = 14781\text{cm}^{-1}$. The sample was at room temperature. The sample was oriented with its long dimension vertical with respect to the laboratory axes; the horizontal (H) and vertical (V) polarisation are also with respect to the lab. Because of the good quality of the scattering face, the plasma lines are absent (laser power: 200 mW; scan: $10\text{ cm}^{-1}/\text{min}$; scale: 100 cps; time constant: 4.7 sec; slits: 3 cm^{-1}). The baseline is shifted for clarity and the values are precise to $\pm 2\text{ cm}^{-1}$.



II.3 - Linear Chain Model

II.3.1 - Calculations of Belenkii

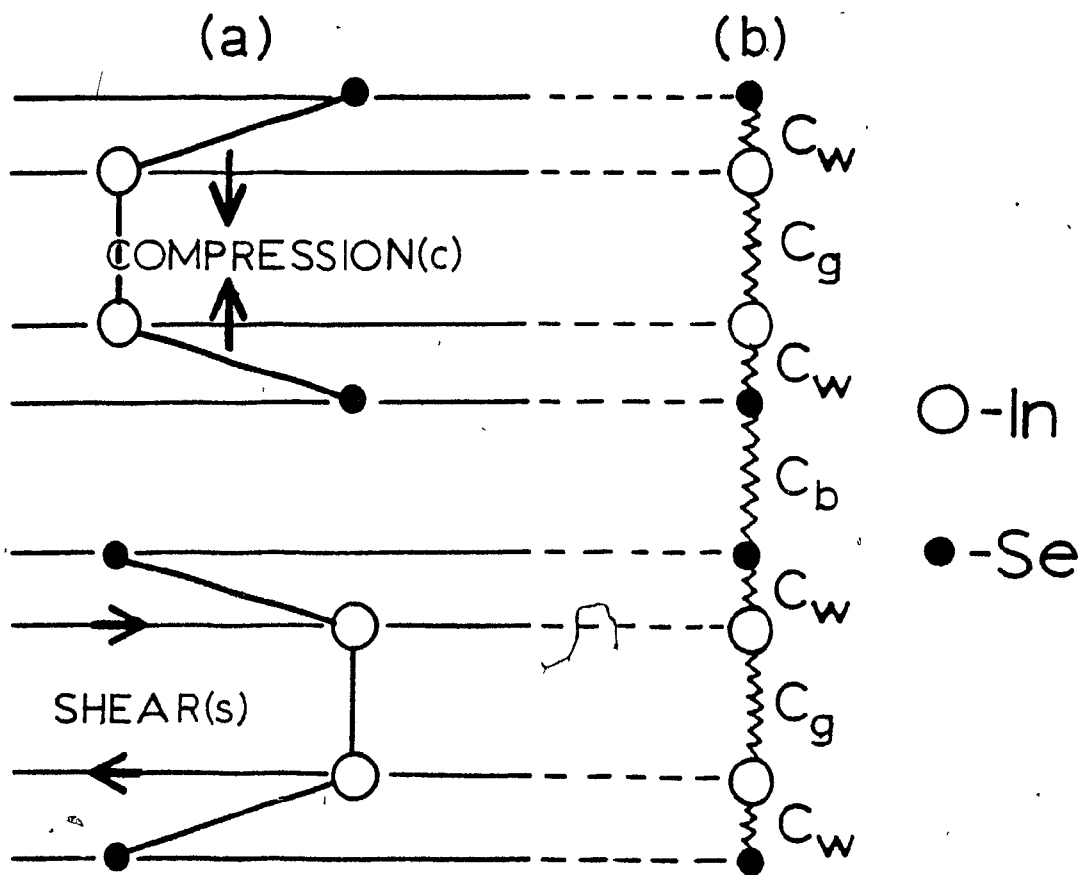
Belenkii et al. [66] have calculated the mode frequencies at the center of the Brillouin zone ($\vec{k} = 0$) for β - In_2Se_2 using the linear chain model (LCM); this model considers only the interaction between adjacent identical atomic planes (Fig. II-10) and not the true force constants between the atoms in the unit cell. The force constants for the compressional modes (superscript c; A i.r.) are larger than those for the shear modes (s; E i.r.) as should be expected in the small displacement limit of the harmonic approximation. For their model they used the values $C_{b,w,g}^c$ and $C_{b,g}^s$ of gallium selenide [67] and deduced C_w^s from the 178 cm^{-1} peak of their infrared measurements. We present in Table II-2 their theoretical results and our experimental values with the corresponding i.r. of each peak. In his article, Belenkii [66] uses the Herring (H) notation for the D_{6h} point group and the corresponding i.r. in the Koster (K) and Mulliken (M) notations are as follow:

$$\Gamma_5(\text{H}) = \Gamma_6(\text{K}) = E_2(\text{M}) \quad \text{and} \quad \Gamma_6(\text{H}) = \Gamma_5(\text{K}) = E_1(\text{M})$$

for both g and u representations [80]. The agreement between the theoretical and experimental values is fairly good for such a crude model that is independent of the polytype and which excludes long-range Coulomb forces.

Fig. II-10. Linear chain model.

Each plane (a) is composed of only one kind of atom. There are two types of modes: compression (c) and shear (s) modes. For the compression modes, the distance between the atomic planes varies; we have a stretching of the In-In bond and mostly a bending (with some stretching of the In-Se bond. In the shear modes the interplane distance is fixed and we have a mixture of stretching and bending of the bonds. The structure is replaced by a system of masses and springs (b); the values of the force constants used by Belenkii et al [66] are given in (c).



(c) Force Constants

(in units of kilodynes/cm)

$$C_w^c = 123. \quad C_w^s = 87.5$$

$$C_g^c = 108. \quad C_g^s = 15.3$$

$$C_b^c = 9.24 \quad C_b^s = 1.63$$

Table II-2. Comparison of our results with the
linear chain model for $\beta\text{-In}_2\text{Se}_2$.

The first column under each heading gives the
irreducible representation of the modes.

TABLE II-2

Linear Chain Model [66]		Our Data	
E_{2g}	16 cm^{-1}	E_{2g}^2	19 cm^{-1}
E_{1g}	53	E_{1g}^1	42
A_{1g}	126	A_{1g}^1	117
E_{2g}	178	E_{2g}^1	179
E_{1g}	184	E_{1g}^2	181
A_{1g}	253	A_{1g}^2	231

II.3.2 - Force Constants Calculations

Using the linear chain model equations of Wieting [67], we calculated the force constants for the shear modes (Appendix D and Table II-3). With these constants, we predicted the values of the E_{1g}^2 and E_{2g}^1 Raman modes and the optically inactive E_{2u}^1 and E_{2u}^2 modes; the concordance with the Raman modes is very good.

For the compression modes, with the A_{2u}^2 infrared active longitudinal mode (LO) at 214 cm^{-1} [66], the LCM calculations do not give physical (real and positive) values for the force constants. The LO mode induces a long-range electric field that shifts the LCM mode frequency to a higher value [81a]. For a three-dimensional crystal possessing two types of atom, the LO and TO modes are degenerate at $\vec{k} = 0$ if this long-range interaction was absent. In a layered compound, the intrinsic anisotropy of the structure prevents the degeneracy of the LO and TO modes at $\vec{k} = 0$ even if the long range electrostatic interaction is neglected; this can be found by calculating the LO and TO frequencies using the valence force model and estimating the force constants. For $\beta\text{-In}_2\text{Se}_2$, the In-In bond length (3.16\AA) is greater than the expected covalent bond (2.88\AA) which indicates a partly ionic bond and some charge transfer to the Se atom [85]. Even if the primitive cell does not have a dipole moment (it has a center of symmetry), the In-Se bond is partly ionic and can contribute

Table II-3. Shear modes frequencies. Values of the calculated (LCM) and experimental phonon modes (*infrared data of Belen'kii [66]) and the force constants (Appendix D).

Mode	Calculated (cm^{-1})		Measured (cm^{-1})	
$\bar{\nu}_0(E_{1u}^1)$	0		—	
$\bar{\nu}_1(E_{1u}^2)$	178.0	matched	178*	T0
$\bar{\nu}_2(E_{2g}^1)$	179.5		179	
$\bar{\nu}_3(E_{2g}^2)$	19.0	matched	19	
$\bar{\nu}_4(E_{1g}^1)$	42.0	matched	42	
$\bar{\nu}_5(E_{1g}^2)$	182.2		181	
$\bar{\nu}_6(E_{2u}^1)$	37.0		—	
$\bar{\nu}_7(E_{2u}^2)$	180.8		—	

Force Constants
(in units of kdynes/cm)

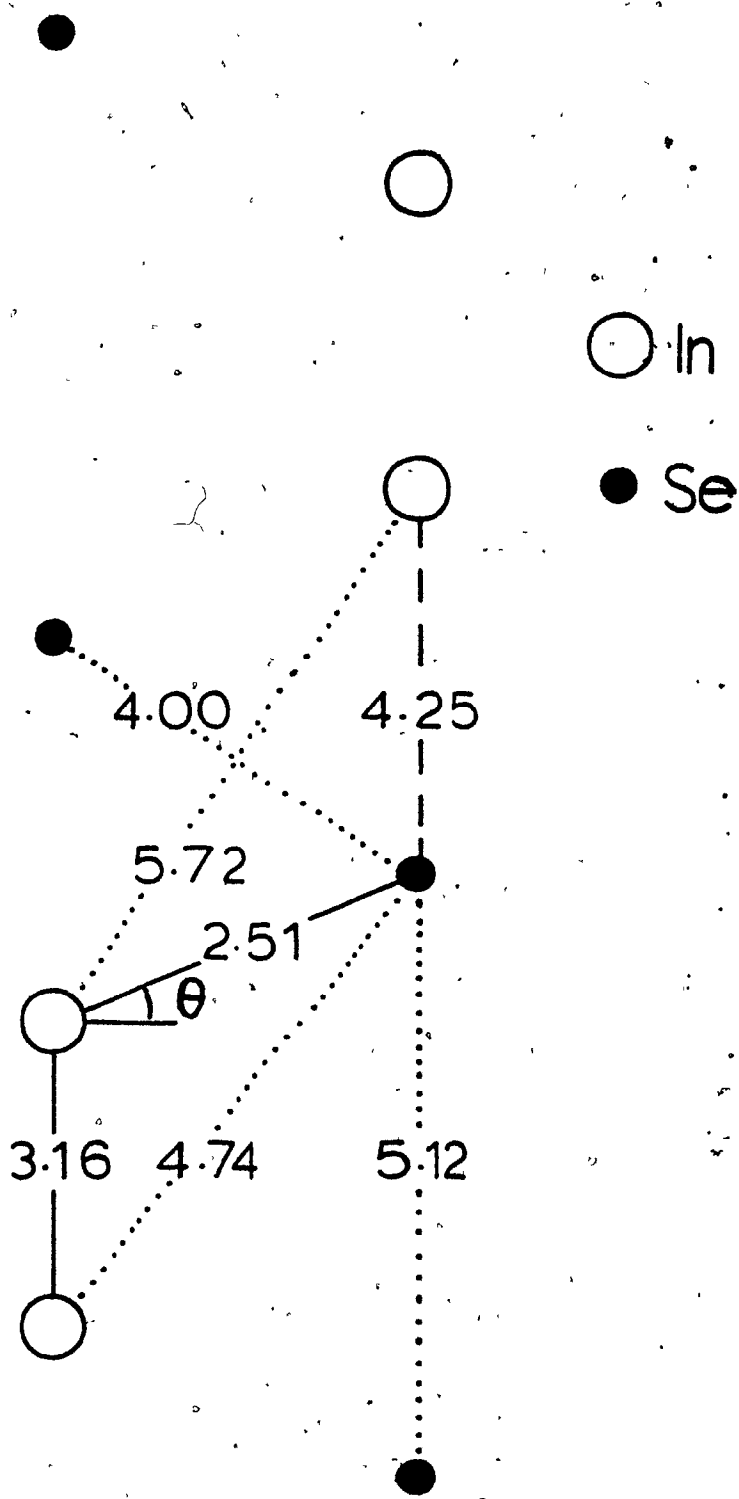
$$C_w^S = 87.3 \quad ; \quad C_b^S = 2.10 \quad ; \quad C_g^S = 8.07$$

an additional electrostatic term in the LO mode frequency calculations.

A more appropriate treatment should use the valence force model to evaluate the frequencies of the longitudinal modes, but unfortunately it needs 5 force constants if we only consider the nearest neighbour interaction, or 8 force constants for the second-nearest neighbour (Fig. II-11); only three experimental values of the mode frequencies are available and this treatment will have to wait the measurements of the optically inactive modes by neutron diffraction.

This approach (valence force model) for the shear modes needs 5 force constants for atom-pair distances smaller or equal to 4.25 \AA ; this model cannot be tested because we also know five mode frequencies. If we neglect the inter-layer Se-Se interaction we are back to the LCM; in this case the In-Se bond force constants (stretching, bending) are transformed into longitudinal and transverse components (C_W^C, C_W^S) .

Fig. II-11. Atomic distances and valence force constants
of $\beta\text{-In}_2\text{Se}_2$. The distance between the different
atoms in the primitive unit cell are given in Å and $\theta = 23.1^\circ$.
The continuous (ionic, covalent) and dashed (van der Waals)
lines represent the stretching and bending force constants for
the bonded atoms; the dotted line corresponds to the radial
force constant of the non-bonded pairs. This valence force
model (longitudinal modes: compression) contains 8 force
constants if we neglect the interactions between atoms that are
distant by more than 5.72 Å; for distances equal and smaller
than 4.25 Å there are 5 force constants. For clarity, only
one type of each kind of pair-interaction is shown (not drawn
to scale).



III. - CONCLUSION

We observed the vibrational modes of $\beta\text{-In}_2\text{Se}_2$ by Raman spectroscopy at low T ($\sim 100^\circ\text{K}$). We identified, for the first time, the interlayer shear mode (E_{2g}^2) of this polytype at 19 cm^{-1} ; it was predicted at 17 cm^{-1} by Jandl et al. [25]. We identified five other peaks at $42(E_{1g}^1)$, $117(A_{1g}^1)$, $179(E_{2g}^1)$, $181(E_{1g}^2)$ and $231\text{ cm}^{-1}(A_{1g}^2)$; the β -polytype is characterized by six vibrational Raman peaks. The irreducible representations of the peaks are based on the labelling of the Raman spectra of $\beta\text{-Ga}_2\text{S}_2$ [65] and the results of the linear chain model (LCM) calculations of Belenkii [66]. The position of the peaks of $\beta\text{-In}_2\text{Se}_2$ follows the trend of $\beta\text{-Ga}_2\text{S}_2$ and $\beta\text{-Ga}_2\text{Se}_2$ when the mass of the different atoms is taken into account.

We also calculated the force constants for the shear modes within the LCM and predicted, with very good agreement, the values for the components of the 180 cm^{-1} doublet (theory: 179.5 and 182.2 ; experiment: 179 and 181 cm^{-1}). We also found the expected optically inactive shear modes calculated within LCM. This model cannot permit us to find the force constants for the compression modes because it does not take into account the ionicity of this compound; the valence force model for the longitudinal (compression) modes is inadequate containing more parameters than the number of known mode frequencies.

We made our measurements with the sample immersed in

superfluid helium and our laser beam focused with a cylindrical lens, while Carlone et al. [68] did their measurements at room temperature with the laser beam focused to a spot; we did not observe the additional peaks in the 400 cm^{-1} region seen in their spectra which are probably due to either a high temperature phase or to two-phonon scattering.

The growth of good quality $\beta\text{-In}_2\text{Se}_2$ crystals (no twinning), although difficult, would permit the investigation of the optically inactive modes by neutron scattering and thus complement the present work.

APPENDICES

APPENDIX ASpin-Orbit Interaction

The separation of the orbital states of cobalt by the octahedron of oxygen in MgO is shown in Fig. 1-2; the wavefunctions of the ground ${}^4T_{1g}$ of 4F in the representation of an effective orbital angular momentum of $\ell = 1$ are [69,70]:

$$|-1\rangle_0 = -\sqrt{5/8} \psi_{3+3} - \sqrt{3/8} \psi_{3-1} \quad (\text{A-1a})$$

$$|0\rangle_0 = \psi_{30} \quad (\text{A-1b})$$

$$|+1\rangle_0 = -\sqrt{5/8} \psi_{3-3} - \sqrt{3/8} \psi_{3+1} \quad (\text{A-1c})$$

The matrix elements of L with respect to these functions are:

$$L_z = -\frac{3}{2} \begin{bmatrix} -1 \\ 0 \\ 1 \end{bmatrix}; \quad L_+ = -\frac{3}{2} \begin{bmatrix} 0 & 0 & 0 \\ \sqrt{2} & 0 & 0 \\ 0 & \sqrt{2} & 0 \end{bmatrix}; \quad L_- = (L_+)^{\dagger} \quad (\text{A-2})$$

which can be translated as $\vec{L} = -3/2 \vec{\ell}$. Because the 4p state contributes a ${}^4T_{1g}$, it will interact with the preceding state and reduce the orbital angular momentum; the new states for the ground will be:

$$|-1\rangle = |-1\rangle_0 \cos\theta - \Pi_{1-1} \sin\theta \quad (\text{A-3a})$$

$$|0\rangle = |0\rangle_0 \cos\theta - \Pi_{10} \sin\theta \quad (\text{A-3b})$$

$$|+1\rangle = |+1\rangle_0 \cos\theta - \Pi_{1+1} \sin\theta \quad (\text{A-3c})$$

where Π_{1m} are the wavefunctions of the 4p state. Then:

$$\begin{aligned} \vec{L} &= -3/2(\cos^2\theta - 2/3\sin^2\theta)\vec{\ell} \\ &= -3/2 a \vec{\ell} \quad (0 < a \leq 1) \end{aligned} \quad (\text{A-4})$$

and we can still treat ℓ as equal to 1. The mixing angle " θ " is a function of the crystal field parameter Dq and Racah's B parameter [33]:

$$\tan\theta = -\{[(15B+6Dq)-[(15B+6Dq)^2 + (8Dq)^2]^{1/2}]/(8Dq)\} \quad (A-5)$$

The ion has a spin $S = 3/2$ with the projections $|-3/2\rangle$, $|-1/2\rangle$, $|+1/2\rangle$ and $|+3/2\rangle$; in this ordered basis the spin-operators are:

$$S_z = \begin{bmatrix} -3/2 & 0 & 0 & 0 \\ 0 & -1/2 & 0 & 0 \\ 0 & 0 & 1/2 & 0 \\ 0 & 0 & 0 & 3/2 \end{bmatrix}; S_+ = \begin{bmatrix} 0 & 0 & 0 & 0 \\ \sqrt{3} & 0 & 0 & 0 \\ 0 & 2 & 0 & 0 \\ 0 & 0 & \sqrt{3} & 0 \end{bmatrix}; S_- = (S_+)^{\dagger} \quad (A-6)$$

With the 3 orbitals and the 4 spin states, there will be 12 spin-orbit states; the first-order Hamiltonian (Eq. I-5a) applied between the $|m_\ell m_s\rangle$ states gives the matrix elements for Table A-I; all the other combinations of the states are zero. The first block being diagonal, the energy of the $j = 5/2$ level ($\Gamma_{7g} + \Gamma_{8g}^2$) is $3/2\lambda'$. Diagonalizing the sub-matrix of the second block, we find the additional value of $-\lambda'$ and, from the third block, we have $-5/2\lambda'$ ($\lambda' = -3/2 ak\lambda_0$); k is the covalency reduction factor of the orbital angular momentum of the ${}^4T_{1g}$ state. The wavefunctions that diagonalize this matrix are in Table A-II.

In a cubic crystal of O_h symmetry there are no representations of dimension superior to 4 and then the level

$j = 5/2$ (dimension 6) will be partially split by the second-order spin-orbit interaction (Eq. I-5b); the corresponding matrix elements are in Table A-III. From the three diagonal blocks we have:

$$E(\Gamma_{6g}) = -5/2 \lambda' - 45/16 \lambda^2/\Delta \quad (\text{A-7a})$$

$$E(\Gamma_{8g}^1) = -\lambda' - 9 \lambda^2/\Delta \quad (\text{A-7b})$$

$$E(\Gamma_{8g}^2) = 3/2 \lambda' - 261/16 \lambda^2/\Delta \quad (\text{A-7c})$$

$$E(\Gamma_{7g}) = 3/2 \lambda' - 45/16 \lambda^2/\Delta \quad (\text{A-7d})$$

with $\lambda' = -3/2 ak\lambda_0$ and $\lambda^2 = akk'\lambda_0^2$ and the condition $0 < k' \leq k \leq 1.0$; k' is the covalency reduction factor of the ${}^4T_{2g}$ state which mixes to the ground ${}^4T_{1g}$. The new wavefunctions are related to those of Table A-II; they are:

$$|a \Gamma_7 \rangle = -\sqrt{5/6} |\Gamma_{7,8}^{+3/2}\rangle + \sqrt{1/6} |\Gamma_{7,8}^{-5/2}\rangle \quad (\text{A-8a})$$

$$|b \Gamma_7 \rangle = -\sqrt{5/6} |\Gamma_{7,8}^{-3/2}\rangle + \sqrt{1/6} |\Gamma_{7,8}^{+5/2}\rangle \quad (\text{A-8b})$$

$$|a \Gamma_8^2 \rangle = \sqrt{1/6} |\Gamma_{7,8}^{+3/2}\rangle + \sqrt{5/6} |\Gamma_{7,8}^{-5/2}\rangle \quad (\text{A-8c})$$

$$|b \Gamma_8^2 \rangle = |\Gamma_{7,8}^{+1/2}\rangle \quad (\text{A-8d})$$

$$|c \Gamma_8^2 \rangle = |\Gamma_{7,8}^{-1/2}\rangle \quad (\text{A-8e})$$

$$|d \Gamma_8^2 \rangle = \sqrt{1/6} |\Gamma_{7,8}^{-3/2}\rangle + \sqrt{5/6} |\Gamma_{7,8}^{+5/2}\rangle \quad (\text{A-8f})$$

The diagonal matrix within these bases is in Table A-IV.

We neglected the contribution of the Γ_{8g}^1 and Γ_{8g}^2 interaction; this approximation is justified in Appendix B.

The ground orbital ${}^4T_{1g}$ composed of $t_{2g}^5 e_g^2$ orbitals [71] with some mixing of ${}^4T_{2g}(t_{2g}^4 e_g^3)$ is not connected to the ${}^2E(t_{2g}^6 e_g)$ by the spin-orbit interaction [33] (see Fig. 1-2): the vibronic interaction (Jahn-Teller effect) would further reduce the effect of the upper excited states on the ground ${}^4T_{1g}$ state.

TABLE A-I

Matrix elements of the first-order spin-orbit interaction (Eq. I-5a) in the $|m_\ell m_s\rangle$ bases ($\lambda' = -3/2$ to $3/2$).

		$3/2$		$x\lambda'$	
		$3/2$	$3/2$		
	$ -1-3/2\rangle$		$ +1\ 3/2\rangle$		
	$ -1-1/2\rangle$	$ 0-3/2\rangle$	$ 1\ 1/2\rangle$	$ 0\ 3/2\rangle$	
	$1/2$	$\sqrt{3/2}$			
	$\sqrt{3/2}$	0			$x\lambda'$
			$1/2$	$\sqrt{3/2}$	
			$\sqrt{3/2}$	0	
	$ -1\ 1/2\rangle$	$ 0-1/2\rangle$	$ 1-3/2\rangle$	$ +1-1/2\rangle$	$ 0+1/2\rangle$
	$-1/2$	$\sqrt{2}$	0		
	$\sqrt{2}$	0	$\sqrt{3/2}$		
	0	$\sqrt{3/2}$	$-3/2$		
				$-1/2$	2
				$\sqrt{2}$	0
				0	$\sqrt{3/2}$
					$-3/2$
					$x\lambda'$

TABLE A-II

Wavefunctions of the first-order spin-orbit levels [70] in the $|\Gamma m_j\rangle$ representation as a function of the $|m_l m_s\rangle$; all the levels being of even parity, the subscript g is removed.

(a)

$$|\Gamma_6^{+1/2}\rangle = \sqrt{1/2} |-1+3/2\rangle - \sqrt{1/3} |0+1/2\rangle + \sqrt{1/6} |+1-1/2\rangle$$

$$|\Gamma_6^{-1/2}\rangle = \sqrt{1/2} |+1-3/2\rangle - \sqrt{1/3} |0-1/2\rangle + \sqrt{1/6} |-1+1/2\rangle$$

$$|\Gamma_8^1 +3/2\rangle = -\sqrt{3/5} |0+3/2\rangle + \sqrt{2/5} |+1+1/2\rangle$$

$$|\Gamma_8^1 +1/2\rangle = \sqrt{2/5} |-1+3/2\rangle + \sqrt{1/15} |0+1/2\rangle - 2\sqrt{2/15} |+1-1/2\rangle$$

$$|\Gamma_8^1 -1/2\rangle = \sqrt{2/5} |+1-3/2\rangle + \sqrt{1/15} |0-1/2\rangle - 2\sqrt{2/15} |-1+1/2\rangle$$

$$|\Gamma_8^1 -3/2\rangle = -\sqrt{3/5} |0-3/2\rangle + \sqrt{2/5} |-1-1/2\rangle$$

(b)

$$|\Gamma_{7,8}^{+5/2}\rangle = |+1+3/2\rangle$$

$$|\Gamma_{7,8}^{+3/2}\rangle = \sqrt{2/5} |0+3/2\rangle + \sqrt{3/5} |+1+1/2\rangle$$

$$|\Gamma_{7,8}^{+1/2}\rangle = \sqrt{1/10} |-1+3/2\rangle + \sqrt{3/5} |0+1/2\rangle + \sqrt{3/10} |+1-1/2\rangle$$

$$|\Gamma_{7,8}^{-1/2}\rangle = \sqrt{1/10} |+1-3/2\rangle + \sqrt{3/5} |0-1/2\rangle + \sqrt{3/10} |-1+1/2\rangle$$

$$|\Gamma_{7,8}^{-3/2}\rangle = \sqrt{2/5} |0-3/2\rangle + \sqrt{3/5} |-1-1/2\rangle$$

$$|\Gamma_{7,8}^{-5/2}\rangle = |-1-3/2\rangle$$

TABLE A-III

Matrix elements of the second-order spin-orbit term (Eq. I-5b);
the bases are from Table A-II ($\Lambda = 15\lambda^2/4\Delta$).

a) Diagonal blocks

	$ \Gamma_6^{+1/2}\rangle$	$ \Gamma_6^{-1/2}\rangle$			
	-3/4	0		$x\Lambda$	
	0	-3/4			
$ \Gamma_8^1+3/2\rangle$	$ \Gamma_8^1+1/2\rangle$	$ \Gamma_8^1-1/2\rangle$	$ \Gamma_8^1-3/2\rangle$		
-12/5					
	-12/5			$x\Lambda$	
		-12/5			
			-12/5		
$ \Gamma_{7,8}^{+5/2}\rangle$	$ \Gamma_{7,8}^{+3/2}\rangle$	$ \Gamma_{7,8}^{+1/2}\rangle$	$ \Gamma_{7,8}^{-1/2}\rangle$	$ \Gamma_{7,8}^{-3/2}\rangle$	$ \Gamma_{7,8}^{-5/2}\rangle$
-15/4				-3/√5	
	-27/20				-3/√5
		-87/20			
			-87/20		$-x\Lambda$
-3/√5				-27/20	
	-3/√5				-15/4

TABLE A-III Cont'db) Non-diagonal block

	$ \Gamma_{7,8}^{+5/2}\rangle$	$ \Gamma_{7,8}^{+3/2}\rangle$	$ \Gamma_{7,8}^{+1/2}\rangle$	$ \Gamma_{7,8}^{-1/2}\rangle$	$ \Gamma_{7,8}^{-3/2}\rangle$	$ \Gamma_{7,8}^{-5/2}\rangle$
$\langle\Gamma_8^1 +3/2 $		$-\sqrt{6/5}$				$-\sqrt{6/5}$
$\langle\Gamma_8^1 +1/2 $			$-6/5$			
$\langle\Gamma_8^1 -1/2 $				$-6/5$		
$\langle\Gamma_8^1 -3/2 $	$-\sqrt{6/5}$				$-\sqrt{6/5}$	

x Λ

TABLE A-IV

Matrix elements with bases of Eq. A-8 ($\Lambda = 15\lambda^2/4\Delta$) of the second-order term of the spin-orbit interaction.

a) Diagonal blocks

	$ a\Gamma_7\rangle$		$ b\Gamma_7\rangle$	
	-3/4			x Λ
			-3/4	
	$ a\Gamma_8^2\rangle$	$ b\Gamma_8^2\rangle$	$ c\Gamma_8^2\rangle$	$ d\Gamma_8^2\rangle$
	-87/20			
		-87/20		x Λ
			-87/20	
				-87/20

b) Non-diagonal block with Γ_8^1

	$ \Gamma_8^1+3/2\rangle$	$ \Gamma_8^1+1/2\rangle$	$ \Gamma_8^1-1/2\rangle$	$ \Gamma_8^1-3/2\rangle$
$\langle a\Gamma_8^2 $	-6/5			
$\langle b\Gamma_8^2 $		-6/5		
$\langle c\Gamma_8^2 $			-6/5	
$\langle d\Gamma_8^2 $				-6/5

APPENDIX B

Second-Order Correction to Spin-Orbit

The second order correction to the second-order spin-orbit energy from the $\Gamma_{8g}^1 - \Gamma_{8g}^2$ interaction is:

$$C_2(\Gamma_n) = \sum_{k \neq n} \frac{|\langle \psi_k | H_{SO}^{(2)} | \psi_n \rangle|^2}{E_n^{(0)} - E_k^{(0)}} \quad (\text{B-1})$$

where $E_m^{(0)}$ is the first-order energy; in our case only one term contributes (see Table A-IVb) and the correction is:

$$|C_2(\Gamma_8)| = \frac{81}{16} \frac{1}{\lambda'} \left(\frac{\lambda^2}{\Delta}\right)^2 = \frac{27}{8} \frac{ak(k')^2 |\lambda_0|^3}{\Delta^2} \quad (\text{B-2})$$

using Eq. I-6.

The maximum correction is for $a = k = k' = 1.0$; with $\Delta = 8Dq = 7680 \text{ cm}^{-1}$ and $|\lambda_0| = 180 \text{ cm}^{-1}$, at most, the error is 0.33 cm^{-1} , which is less than the resolution of our spectra.

APPENDIX CDynamical Jahn-Teller Interaction

The total vibronic Hamiltonian in the molecular cluster approximation for an orbital triplet in an octahedral symmetry is [33]:

$$H_{\text{vib}} = H_{\text{latt}} + H_{\text{O-1}} \quad (\text{C-1})$$

where the first term is the lattice energy given by:

$$H_{\text{latt}} = \frac{I}{2\mu_e} [(P_{\theta}^2 + P_{\epsilon}^2) + \mu_e^2 \omega_e^2 (Q_{\theta}^2 + Q_{\epsilon}^2)] + \\ + \frac{I}{2\mu_t} [(P_{\xi}^2 + P_{\eta}^2 + P_{\zeta}^2) + \mu_t^2 \omega_t^2 (Q_{\xi}^2 + Q_{\eta}^2 + Q_{\zeta}^2)] \quad (\text{C-2})$$

and the second term is Eq. I-7.

The first bracket represents the E_g phonons (partners θ, ϵ) of frequency ω_e and mass μ_e while the second bracket is for the T_{2g} phonons (partners ξ, η, ζ) of frequency ω_t and mass μ_t ; in our case $\mu_e = \mu_t$ and is the mass of the ligand oxygen ion. The Q's and the P's are the displacements and momenta conjugate operators and I is the unit matrix. The H_{latt} term adds a constant value for all the spin-orbit levels and does not enter in the level separations.

We have calculated the contribution of the orbital-lattice interaction on the spin-orbit levels using perturbation theory up to second-order (the first-order term is zero):

$$E(\Gamma, n=0) - E^0(\Gamma) = \sum_i \frac{|\langle \Gamma_i, n | H_{0-1} | \Gamma 0 \rangle|^2}{E^0(\Gamma) - E^0(\Gamma_i, n)} \quad (C-3)$$

The spin-orbit splitting between the Γ_{6g} and Γ_{8g}^1 levels is of the same order as the phonon energies, so we only looked at the shifting of each $|\Gamma_i, n=0\rangle$ by the interaction with $|\Gamma_i, n=1\rangle$. Rewriting the displacement operator (Eq. I-8a) as:

$$Q_\alpha = \left(\frac{\hbar}{2\mu\omega_\alpha}\right)^{1/2} q_\alpha \quad (C-4a)$$

$$q_\alpha = (b_\alpha^+ + b_\alpha) \quad (C-4b)$$

and first looking at the coupling to one E_g phonon we have:

$$[E(\Gamma 0) - E^0(\Gamma)]_{e_g} = E_{jt}(E) \sum_i |\langle \Gamma_i, n=1 | (q_{\theta E_\theta} + q_{\epsilon E_\epsilon}) | \Gamma 0 \rangle|^2 \quad (C-5)$$

and $E_{jt}(E) = v_e^2 / 2\mu\omega_e^2$ and replacing $E^0(\Gamma_i, n=1)$ by $E^0(\Gamma) + \hbar\omega_e$ in Eq. C-3.

The Γ_{8g} levels are shifted by their one-phonon levels; The irreducible representations of the vibronic $|\Gamma_{8g}, n=1\rangle$ levels are (Table C-I):

$$\Gamma_{8g} \times E_g = \Gamma_{6g}^p + \Gamma_{7g}^p + \Gamma_{8g}^p \quad (C-6)$$

The only contribution to the shift is from the one-phonon excited Γ_{8g}^p .

The matrix elements of the operators E_θ and E_ϵ are given in Table C-II and C-III and the symmetrized wavefunctions of the Γ^P are given in Table C-IV. The corresponding shifts of the $|\Gamma_8 n=0\rangle$ levels are:

$$[E(\Gamma_8^1 0) - E^0(\Gamma_8^1)]_e = [E(\Gamma_8^2 0) - E^0(\Gamma_8^2)]_e = -\frac{81}{50} E_{jt}(E) \quad (C-7)$$

In the case of the interaction with a T_{2g} phonon, group theory gives:

$$\Gamma_{8g} \times T_{2g} = \Gamma_{6g}^P + \Gamma_{7g}^P + 2 \Gamma_{8g}^P \quad (C-8)$$

and there is two contributions from the one-phonon Γ_8^P levels. The corresponding shift is obtained from:

$$[E(\Gamma_8 0) - E^0(\Gamma_8)]_t = \frac{4}{3} E_{jt}(T) \sum_i |\langle \Gamma_i | (q_\xi T_\xi + q_\eta T_\eta + q_\zeta T_\zeta) | \Gamma_8 0 \rangle|^2 \quad (C-9)$$

The matrix elements of the T_α ($\alpha = \xi, \eta, \zeta$) operators is in Table C-V to C-VII and the symmetrized wavefunctions for the Γ^P levels are in Table C-VIII. The phase of the phonon u_3 is opposite the value given in Koster Tables [72] so that the contribution of Γ_{6g}^P and Γ_{7g}^P is zero.

The calculated shifts are:

$$[E(\Gamma_8^1 0) - E^0(\Gamma_8^1)]_t = -\frac{243}{100} E_{jt}(T) \quad (C-10a)$$

$$[E(\Gamma_8^2 0) - E^0(\Gamma_8^2)]_t = -\frac{243}{1600} E_{jt}(T) \quad (C-10b)$$

and the Γ_{8g}^1 level is more shifted.

The Γ_{6g} and Γ_{7g} levels are not shifted by the Jahn-Teller interaction being Kramers doublets [73,74]. From group theory, we have non-zero matrix elements from Eq. C-3 if the irreducible representations of the initial and final states are the same; for the interaction with an E_g phonon for these states, we have (see Table C-I):

$$\Gamma_{6g} \times E_g = \Gamma_{8g}^p ; \quad \Gamma_{7g} \times E_g = \Gamma_{8g}^p \quad (C-11)$$

and for a T_{2g} mode:

$$\Gamma_{6g} \times T_{2g} = \Gamma_{7g}^p + \Gamma_{8g}^p$$

$$\Gamma_{7g} \times T_{2g} = \Gamma_{6g}^p + \Gamma_{8g}^p$$

So there is no Jahn-Teller shift for these levels.

TABLE C-I (see Ref. 72)

a) Irreducible representations (i.r.) of the double point group θ_h ; roman letters are phonon and orbital states labels while the Γ are for the spin-orbit states. (u = ungerade or odd, g = gerade or even under inversion; dim. = dimension of the i.r.)

i.r.	i.r.	dim.	i.r.	i.r.
A _{1u}	Γ_{1u}	1	Γ_{1g}	A _{1g}
A _{2u}	Γ_{2u}	1	Γ_{2g}	A _{2g}
E _u	Γ_{3u}	2	Γ_{3g}	E _g
T _{1u}	Γ_{4u}	3	Γ_{4g}	T _{1g}
T _{2u}	Γ_{5u}	3	Γ_{5g}	T _{2g}
	Γ_{6u}	2	Γ_{6g}	
	Γ_{7u}	2	Γ_{7g}	
	Γ_{8u}	4	Γ_{8g}	

TABLE C-I (Cont'd)

b) Multiplication table of the i.r.; $j = \Gamma_j$ and $2\Gamma_j = j^2$
 (u X u = g X g = g; u X g = u)

Γ_1	Γ_2	Γ_3	Γ_4	Γ_5	Γ_6	Γ_7	Γ_8	
1	2	3	4	5	6	7	8	Γ_1
	1	3	5	4	7	6	8	Γ_2
		1+2+3	4+5	4+5	8	8	6+7+8	Γ_3
			1+3+4+5	2+3+4+5	6+8	7+8	$6+7+8^2$	Γ_4
				1+3+4+5	7+8	6+8	$6+7+8^2$	Γ_5
					1+4	2+5	3+4+5	Γ_6
						1+4	3+4+5	Γ_7
							$1+2+3+4^2+5^2$	Γ_8

TABLE C-II

Matrix elements of $E_{\theta} = 1/2 (3L_z^2 - L^2)$ between the orbital parts of the spin-orbit levels (see Table A-II and Eq. A-8 for the exact form of the wavefunctions); only the non-zero sub-matrices are given.

a) Diagonal sub-matrices

$ \Gamma_8^1+3/2\rangle$	$ \Gamma_8^1+1/2\rangle$	$ \Gamma_8^1-1/2\rangle$	$ \Gamma_8^1-3/2\rangle$	
-1				
	+1			x(9/10)
		+1		
			-1	
$ a\Gamma_8^2\rangle$	$ b\Gamma_8^2\rangle$	$ c\Gamma_8^2\rangle$	$ d\Gamma_8^2\rangle$	
+1				
	-1			x(9/10)
		-1		
			+1	

b) Non-diagonal sub-matrices

	$ a\Gamma_8^2\rangle$	$ b\Gamma_8^2\rangle$	$ c\Gamma_8^2\rangle$	$ d\Gamma_8^2\rangle$
$\langle\Gamma_8^1+3/2 $	+1			
$\langle\Gamma_8^1+1/2 $		-1		x(27/40)
$\langle\Gamma_8^1-1/2 $			-1	
$\langle\Gamma_8^1-3/2 $				+1

TABLE C-II (cont'd)

	$ \Gamma_8^{1+1/2}\rangle$	$ \Gamma_8^{1-1/2}\rangle$	$ \text{b}\Gamma_8^2\rangle$	$ \text{c}\Gamma_8^2\rangle$
$\langle\Gamma_6^{+1/2} $	+1		+3	$x(9\sqrt{5}/40)$
$\langle\Gamma_6^{-1/2} $		+1		+3
	$ \Gamma_8^{1+3/2}\rangle$	$ \Gamma_8^{1-3/2}\rangle$	$ \text{a}\Gamma_8^2\rangle$	$ \text{d}\Gamma_8^2\rangle$
$\langle\text{a}\Gamma_7 $	-3		+1	$x(9\sqrt{5}/40)$
$\langle\text{b}\Gamma_7 $		-3		+1

TABLE C-III

Matrix elements of $E_E = \sqrt{3}/4(L_+^2 - L_-^2)$ between the orbital parts of the spin-orbit levels (see Table A-II and Eq. A-8 for the exact form of the wavefunctions).

a) Diagonal sub-matrices

$ \Gamma_8^1+3/2\rangle$	$ \Gamma_8^1+1/2\rangle$	$ \Gamma_8^1-1/2\rangle$	$ \Gamma_8^1-3/2\rangle$	
		-1		
			-1	x(9/10)
-1				
	-1			
$ a\Gamma_8^2\rangle$	$ b\Gamma_8^2\rangle$	$ c\Gamma_8^2\rangle$	$ d\Gamma_8^2\rangle$	
		+1		
			+1	x(9/10)
+1				
	+1			

b) Non-diagonal sub-matrices

	$ a\Gamma_8^2\rangle$	$ b\Gamma_8^2\rangle$	$ c\Gamma_8^2\rangle$	$ d\Gamma_8^2\rangle$	
$\langle\Gamma_8^1+3/2 $			+1		
$\langle\Gamma_8^1+1/2 $				+1	x(27/40)
$\langle\Gamma_8^1-1/2 $	+1				
$\langle\Gamma_8^1-3/2 $		+1			

TABLE C-III (cont'd)

	$ \Gamma_8^1+3/2\rangle$	$ \Gamma_8^1-3/2\rangle$	$ \text{a}\Gamma_8^2\rangle$	$ \text{d}\Gamma_8^2\rangle$
$\langle\Gamma_6+1/2 $		+1		+3 $\times(9\sqrt{5}/40)$
$\langle\Gamma_6-1/2 $	+1		+3	
	$ \Gamma_8^1+1/2\rangle$	$ \Gamma_8^1-1/2\rangle$	$ \text{b}\Gamma_8^2\rangle$	$ \text{c}\Gamma_8^2\rangle$
$\langle\text{a}\Gamma_7 $		+3		-1 $\times(9\sqrt{5}/40)$
$\langle\text{b}\Gamma_7 $	+3		-1	

TABLE C-IV

Symmetrized wavefunctions of the one-phonon vibronic levels obtained from the coupling between an E_g phonon and a Γ_8 spin-orbit level; u_1 transforms as $(3z^2-r^2)$ and u_2 as $\sqrt{3}(x^2-y^2)$ (Table 83 pg. 91 of Ref. 72)*

$$\psi_{+1/2}^6 = \sqrt{1/2} (-u_1 |b\Gamma_8\rangle - u_2 |d\Gamma_8\rangle)$$

$$\psi_{-1/2}^6 = \sqrt{1/2} (+u_1 |c\Gamma_8\rangle + u_2 |a\Gamma_8\rangle)$$

$$\psi_{+1/2}^7 = \sqrt{1/2} (-u_1 |d\Gamma_8\rangle + u_2 |b\Gamma_8\rangle)$$

$$\psi_{-1/2}^7 = \sqrt{1/2} (+u_1 |a\Gamma_8\rangle - u_2 |c\Gamma_8\rangle)$$

$$\psi_{+3/2}^8 = \sqrt{1/2} (+u_1 |a\Gamma_8\rangle + u_2 |c\Gamma_8\rangle)$$

$$\psi_{+1/2}^8 = \sqrt{1/2} (-u_1 |b\Gamma_8\rangle + u_2 |d\Gamma_8\rangle)$$

$$\psi_{-1/2}^8 = \sqrt{1/2} (-u_1 |c\Gamma_8\rangle + u_2 |a\Gamma_8\rangle)$$

$$\psi_{-3/2}^8 = \sqrt{1/2} (+u_1 |d\Gamma_8\rangle + u_2 |b\Gamma_8\rangle)$$

* The correspondence for the Γ_8^2 is direct but for Γ_8^1 we have $a = +3/2$, $b = +1/2$, $c = -1/2$, $d = -3/2$.

TABLE C-V

Matrix elements of $T_{\xi} = \frac{-i}{2}[(L_z L_+ + L_+ L_z) - (L_z L_- + L_- L_z)]$
between the orbital parts of the spin-orbit levels.

a) Diagonal sub-matrices

$ \Gamma_8^1+3/2\rangle$	$ \Gamma_8^1+1/2\rangle$	$ \Gamma_8^1-1/2\rangle$	$ \Gamma_8^1-3/2\rangle$	
	-i			
+i				
			+i	$\times(3\sqrt{3}/5)$
		-i		
$ a\Gamma_8^2\rangle$	$ b\Gamma_8^2\rangle$	$ c\Gamma_8^2\rangle$	$ d\Gamma_8^2\rangle$	
	-i			
+i				
			+i	$\times(3\sqrt{3}/20)$
		-i		

b) Non-diagonal sub-matrices

	$ \Gamma_6^1+1/2\rangle$	$ \Gamma_6^1-1/2\rangle$	$ a\Gamma_7\rangle$	$ b\Gamma_7\rangle$	
$\langle\Gamma_8^1+3/2 $	$-i\sqrt{3}$			$-3i$	
$\langle\Gamma_8^1+1/2 $		$-3i$	$+i\sqrt{3}$		$\times(3\sqrt{5}/40)$
$\langle\Gamma_8^1-1/2 $	$-3i$			$+i\sqrt{3}$	
$\langle\Gamma_8^1-3/2 $		$-i\sqrt{3}$	$-3i$		
$\langle a\Gamma_8^2 $	$+i\sqrt{3}$			$+3i$	
$\langle b\Gamma_8^2 $		$+3i$	$-i\sqrt{3}$		
$\langle c\Gamma_8^2 $	$+3i$			$-i\sqrt{3}$	$\times(3\sqrt{5}/20)$
$\langle d\Gamma_8^2 $		$+i\sqrt{3}$	$+3i$		

TABLE C-V (Cont'd)

	$ a\Gamma_8^2\rangle$	$ b\Gamma_8^2\rangle$	$ c\Gamma_8^2\rangle$	$ d\Gamma_8^2\rangle$	
$\langle\Gamma_8^1+3/2 $		$-9i\sqrt{3}$		$-15i$	
$\langle\Gamma_8^1+1/2 $	$-i\sqrt{3}$		$+15i$		$x(3/40)$
$\langle\Gamma_8^1-1/2 $		$+15i$		$-i\sqrt{3}$	
$\langle\Gamma_8^1-3/2 $	$-15i$		$-9i\sqrt{3}$		
		$ \Gamma_6^1+1/2\rangle$	$ \Gamma_6^1-1/2\rangle$		
$\langle a\Gamma_7 $		$-i$			$x(3\sqrt{3}/4)$
$\langle b\Gamma_7 $			$-i$		

TABLE C-VI

Matrix elements of $T_{\eta} = 1/2[(L_+L_z + L_zL_+) + (L_-L_z + L_zL_-)]$
between the orbital parts of the spin-orbit levels.

a) Diagonal sub-matrices

$ \Gamma_8^1+3/2\rangle$	$ \Gamma_8^1+1/2\rangle$	$ \Gamma_8^1-1/2\rangle$	$ \Gamma_8^1-3/2\rangle$
	+1		
+1			$x(3\sqrt{3}/5)$
			-1
		-1	
$\langle a\Gamma_8^2\rangle$	$\langle b\Gamma_8^2\rangle$	$\langle c\Gamma_8^2\rangle$	$\langle d\Gamma_8^2\rangle$
	+1		
+1			$x(3\sqrt{3}/20)$
			-1
		-1	

b) Non-diagonal sub-matrices

	$ \Gamma_6^1+1/2\rangle$	$ \Gamma_6^1-1/2\rangle$	$ a\Gamma_7\rangle$	$ b\Gamma_7\rangle$
$\langle\Gamma_8^1+3/2 $	$+\sqrt{3}$			-3
$\langle\Gamma_8^1+1/2 $		+3	$+\sqrt{3}$	
$\langle\Gamma_8^1-1/2 $	-3			$-\sqrt{3}$
$\langle\Gamma_8^1-3/2 $		$-\sqrt{3}$	+3	
$\langle a\Gamma_8^2 $	$-\sqrt{3}$			+3
$\langle b\Gamma_8^2 $		-3	$-\sqrt{3}$	
$\langle c\Gamma_8^2 $	+3			$+\sqrt{3}$
$\langle d\Gamma_8^2 $		$+\sqrt{3}$	-3	

$x(3\sqrt{5}/40)$

$x(3\sqrt{5}/20)$

TABLE C-VI (Cont'd)

	$ a\Gamma_8^2\rangle$	$ b\Gamma_8^2\rangle$	$ c\Gamma_8^2\rangle$	$ d\Gamma_8^2\rangle$
$\langle\Gamma_8^1+3/2 $		$+9\sqrt{3}$	0	-15
$\langle\Gamma_8^1+1/2 $	$-\sqrt{3}$		-15	$x(3/40)$
$\langle\Gamma_8^1-1/2 $		+15		$+\sqrt{3}$
$\langle\Gamma_8^1-3/2 $	+15		$-9\sqrt{3}$	
		$ \Gamma_6^{+1/2}\rangle$	$ \Gamma_6^{-1/2}\rangle$	
$\langle a\Gamma_7 $		+1		$x(3\sqrt{3}/4)$
$\langle b\Gamma_7 $			-1	

TABLE C-VII

Matrix elements of $T_{\zeta} = -i/2(L_{+}^2 - L_{-}^2)$ between the orbital parts of the spin-orbit levels.

a) Diagonal sub-matrices

$ \Gamma_8^1+3/2\rangle$	$ \Gamma_8^1+1/2\rangle$	$ \Gamma_8^1-1/2\rangle$	$ \Gamma_8^1-3/2\rangle$
		+i	
			+i
-i			$x(3\sqrt{3}/5)$
	-i		
$ a\Gamma_8^2\rangle$	$ b\Gamma_8^2\rangle$	$ c\Gamma_8^2\rangle$	$ d\Gamma_8^2\rangle$
		+i	
			+i
-i			$x(3\sqrt{3}/20)$
	-i		

b) Non-diagonal sub-matrices

	$ \Gamma_6^1+1/2\rangle$	$ \Gamma_6^1-1/2\rangle$	$ a\Gamma_7\rangle$	$ b\Gamma_7\rangle$
$\langle\Gamma_8^1+3/2 $		-i		
$\langle\Gamma_8^1+1/2 $				-i
$\langle\Gamma_8^1-1/2 $			+i	$x(3\sqrt{15}/20)$
$\langle\Gamma_8^1-3/2 $	+i			
$\langle a\Gamma_8^2 $		+i		
$\langle b\Gamma_8^2 $				+i
$\langle c\Gamma_8^2 $			-i	$x(3\sqrt{15}/10)$
$\langle d\Gamma_8^2 $	-i			

TABLE C-VII (Cont'd)

	$ a\Gamma_8^2\rangle$	$ b\Gamma_8^2\rangle$	$ c\Gamma_8^2\rangle$	$ d\Gamma_8^2\rangle$	
$\langle\Gamma_8^1+3/2 $			-3i		
$\langle\Gamma_8^1+1/2 $				7i	$x(3\sqrt{3}/20)$
$\langle\Gamma_8^1-1/2 $	-7i				
$\langle\Gamma_8^1-3/2 $		+3i			
		$ \Gamma_6+1/2\rangle$	$ \Gamma_6-1/2\rangle$		
$\langle a\Gamma_7 $			+i		$x(3\sqrt{3}/4)$
$\langle b\Gamma_7 $	-i				

TABLE C-VIII

Symmetrized wavefunctions of the one-phonon vibronic levels, obtained from the coupling between a T_{2g} phonon and a Γ_8 spin-orbit level; u_1 transforms as yz , u_2 as xz and u_3 as xy (ref. 72 p.95; the phase of u_3 is changed so that $\langle \Gamma_8 | H_{jt}(T) | \psi^n \rangle = 0$ for $n = 6, 7$). For the relation between our s.o. functions and the notation see Table C-IV.

$$\begin{aligned} \psi_{+3/2}^8 &= 1/\sqrt{15} [\sqrt{3}(iu_1 - u_2)|d\Gamma_8\rangle + 2(iu_1 + u_2)|b\Gamma_8\rangle + iu_3|c\Gamma_8\rangle] \\ \psi_{+1/2}^8 &= 1/\sqrt{5} [(-iu_1 - u_2)|c\Gamma_8\rangle - i\sqrt{3}u_3|d\Gamma_8\rangle] \\ \psi_{-1/2}^8 &= 1/\sqrt{5} [(-iu_1 + u_2)|b\Gamma_8\rangle + i\sqrt{3}u_3|a\Gamma_8\rangle] \\ \psi_{-3/2}^8 &= 1/\sqrt{15} [2(iu_1 - u_2)|c\Gamma_8\rangle + \sqrt{3}(iu_1 + u_2)|a\Gamma_8\rangle - iu_3|b\Gamma_8\rangle] \\ \phi_{3/2}^8 &= 1/\sqrt{20} [(iu_1 - u_2)|d\Gamma_8\rangle + \sqrt{3}(-iu_1 - u_2)|b\Gamma_8\rangle + 2iu_3\sqrt{3}|c\Gamma_8\rangle] \\ \phi_{1/2}^8 &= 1/\sqrt{60} [\sqrt{3}(-iu_1 - u_2)|c\Gamma_8\rangle + 5(iu_1 - u_2)|a\Gamma_8\rangle + 2iu_3|d\Gamma_8\rangle] \\ \phi_{-1/2}^8 &= 1/\sqrt{60} [5(iu_1 + u_2)|d\Gamma_8\rangle + \sqrt{3}(-iu_1 + u_2)|b\Gamma_8\rangle - 2iu_3|a\Gamma_8\rangle] \\ \phi_{-3/2}^8 &= 1/\sqrt{20} [\sqrt{3}(-iu_1 + u_2)|c\Gamma_8\rangle + (iu_1 + u_2)|a\Gamma_8\rangle - 2iu_3\sqrt{3}|b\Gamma_8\rangle] \\ \psi_{+1/2}^7 &= 1/\sqrt{12} [(-iu_1 + u_2)|c\Gamma_8\rangle + \sqrt{3}(iu_1 + u_2)|a\Gamma_8\rangle + 2iu_3|b\Gamma_8\rangle] \\ \psi_{-1/2}^7 &= 1/\sqrt{12} [\sqrt{3}(-iu_1 + u_2)|d\Gamma_8\rangle + (iu_1 + u_2)|b\Gamma_8\rangle + 2iu_3|c\Gamma_8\rangle] \\ \psi_{+1/2}^6 &= 1/\sqrt{12} [\sqrt{3}(-iu_1 - u_2)|c\Gamma_8\rangle + (-iu_1 + u_2)|a\Gamma_8\rangle + 2iu_3|d\Gamma_8\rangle] \\ \psi_{-1/2}^6 &= 1/\sqrt{12} [(iu_1 + u_2)|d\Gamma_8\rangle + \sqrt{3}(iu_1 - u_2)|b\Gamma_8\rangle + 2iu_3|a\Gamma_8\rangle] \end{aligned}$$

APPENDIX D

Force Constants Calculations

At the center of the Brillouin zone ($\vec{k} = 0$), the phonon frequencies for $\beta\text{-In}_2\text{Se}_2$ are [67]

$$\omega_0^2(A_{2u}^1, E_{1u}^1) = 0 \quad (\text{D-1})$$

$$\omega_1^2(A_{2u}^2, E_{1u}^2) = 2\alpha \quad (\text{D-2})$$

$$\omega_2^2(B_{2g}^1, E_{2g}^1) = \alpha + \beta + [(\alpha + \beta)^2 - \lambda\delta]^{1/2} \quad (\text{D-3})$$

$$\omega_3^2(B_{2g}^2, E_{2g}^2) = \alpha + \beta - [(\alpha + \beta)^2 - \lambda\delta]^{1/2} \quad (\text{D-4})$$

$$\omega_4^2(A_{1g}^1, E_{1g}^1) = \alpha + \beta + \gamma - [(\alpha + \beta + \gamma)^2 - \lambda(\delta + \epsilon + \zeta)]^{1/2} \quad (\text{D-5})$$

$$\omega_5^2(A_{1g}^2, E_{1g}^2) = \alpha + \beta + \gamma + [(\alpha + \beta + \gamma)^2 - \lambda(\delta + \epsilon + \zeta)]^{1/2} \quad (\text{D-6})$$

$$\omega_6^2(B_{1u}^1, E_{2u}^1) = \alpha + \gamma - [(\alpha + \gamma)^2 - \lambda\epsilon]^{1/2} \quad (\text{D-7})$$

$$\omega_7^2(B_{1u}^2, E_{2u}^2) = \alpha + \gamma + [(\alpha + \gamma)^2 - \lambda\epsilon]^{1/2} \quad (\text{D-8})$$

with $\alpha = C_W^n/2M$, $\beta = C_b^n/M_2$, $\gamma = C_g^n/M_1$, $\delta = C_W^n C_b^n$, $\epsilon = C_W^n C_g^n$, $\zeta = 2C_b^n C_g^n$, $\lambda = 2/M_1 M_2$, $M = M_1 M_2 / (M_1 + M_2)$, $\omega_i = 2\pi c \bar{\nu}_i$ and $M_1 = M(\text{In})$, $M_2 = M(\text{Se})$. The superscript n refers to the compression (c) modes (A and B i.r. in parenthesis) and to the shear (s) modes (E i.r.). The activity of the different modes is.

Acoustic modes	$A_{2u}^1 ; E_{1u}^1$
Infrared modes	$A_{2u}^2 ; E_{1u}^2$
Raman modes	$A_{1g}^1, A_{1g}^2 ; E_{1g}^1, E_{1g}^2, E_{2g}^1, E_{2g}^2$
Optically inactive modes	$B_{1u}^1, B_{1u}^2, B_{2g}^1, B_{2g}^2 ; E_{2u}^1, E_{2u}^2$

We need three equations to find the three force constants (see Fig. II-9); from equation D-2 we have, for the shear modes

$$C_W^S = (2\pi c\bar{\nu}_1)^2 M \quad (D-9)$$

Including this value into eq. D-4 and rearranging the terms

$$C_b^S = 2(\pi c\bar{\nu}_3)^2 M_2 \left[\frac{\bar{\nu}_3^2 - \bar{\nu}_1^2}{\bar{\nu}_3^2 - (M/M_1)\bar{\nu}_1^2} \right] \quad (D-10)$$

And from equ. D-5 we get

$$C_g^S = 2(\pi c)^2 M_1 \left[\frac{\bar{\nu}_4^2(\bar{\nu}_4^2 - \bar{\nu}_1^2 - \theta) + (M/M_1)\bar{\nu}_1^2 \theta}{\bar{\nu}_4^2 - (M/M_2)\bar{\nu}_1^2 - \theta} \right] \quad (D-11)$$

with $\theta = C_b^S / (2\pi^2 c^2 M_2)$ and, $M_1 = 114.8g/N_0$ and $M_2 = 78.96g/N_0$ (N_0 is the Avogadro number).

With these values we can evaluate the frequencies for all the shear modes and check with our experimental values for the E_{1g}^2 and E_{2g}^1 Raman modes (see Table II-3); we also give the values of the two E_{2u} modes, that can only be observed by neutron diffraction.

From the infrared measurements of Belenkii [66], the A_{2u}^2 (longitudinal optic: LO) mode is at $\bar{\nu}_1 = 214\text{cm}^{-1}$ which implies, from equ. E-2, that we have $C_W^C = 126.2\text{kdyn/cm}$. To find the other force constants (C_g^C, C_b^C), we use equ. D-5 and D-6, and find the following relations

$$C_g^C = 2(\pi c)^2 M_1 (\bar{v}_5^2 + \bar{v}_4^2 - \bar{v}_1^2 - \theta) \quad (D-12)$$

$$C_b^C = 2(\pi c)^2 M_2 \left[\frac{(\bar{v}_4 \bar{v}_5)^2 - (M/M_2) \bar{v}_1^2 \phi}{(M/M_1) \bar{v}_1^2 + \phi} \right] \quad (D-13)$$

with $\theta = C_b^C / (2\pi^2 c^2 M_2)$ and $\phi = C_g^C / (2\pi^2 c^2 M_1)$. From these two coupled equations we find the quadratic expressions

$$\theta^2 - A\theta + B = 0 \quad (D-14a)$$

$$A = \bar{v}_4^2 + \bar{v}_5^2 - \bar{v}_1^2 + M \bar{v}_1^2 \left(\frac{1}{M_1} - \frac{1}{M_2} \right) \quad (D-14b)$$

$$B = (\bar{v}_4 \bar{v}_5)^2 - \frac{M}{M_2} \bar{v}_1^2 (\bar{v}_4^2 + \bar{v}_5^2 - \bar{v}_1^2) \quad (D-14c)$$

or

$$\phi^2 - D\phi + E = 0 \quad (D-15a)$$

$$D = \bar{v}_4^2 + \bar{v}_5^2 - \bar{v}_1^2 + M \bar{v}_1^2 \left(\frac{1}{M_2} - \frac{1}{M_1} \right) \quad (D-15b)$$

$$E = (\bar{v}_4 \bar{v}_5)^2 - \frac{M}{M_1} \bar{v}_1^2 (\bar{v}_4^2 + \bar{v}_5^2 - \bar{v}_1^2) \quad (D-15c)$$

the solution of which are

$$\theta = \frac{1}{2} [A \pm \sqrt{A^2 - 4B}] \quad (D-16a)$$

or

$$\phi = \frac{1}{2} [D \pm \sqrt{D^2 - 4E}] \quad (D-16b)$$

with the sign in front of the square root taken so that

$\phi > \theta$ [84c]. With $\bar{\nu}_1 = 214$, $\bar{\nu}_4 = 117$ and $\bar{\nu}_5 = 231 \text{cm}^{-1}$, we find that the term under the square root for θ and ϕ (eq. D-16) is negative when θ and ϕ should be real and positive. Without the neutron data, we cannot calculate the LCM compression force constants.

APPENDIX EGroup TheoryE-I. Definitions and Properties of Groups

A group G is a set of elements ($R_i ; i = 1, \dots, h$) which obeys the following four rules:

- 1) Closure: the product of two elements of the set is an element of the set.

$$R_i R_j = R_k, \text{ for all } R_n \text{ of } G (n = i, j, k) \quad (E-1)$$

- 2) Identity: The set must contain the identity I , such that:

$$I R_i = R_i I = R_i, \text{ for all } R_i \text{ of } G. \quad (E-2)$$

- 3) Inverse: every element of the set has an inverse which is also an element of the set.

$$R_i^{-1} R_i = R_i R_i^{-1} = I, \text{ for all } R_i \text{ of } G. \quad (E-3)$$

- 4) Associativity: for any three elements of the set we have:

$$R_i (R_j R_k) = (R_i R_j) R_k, \text{ for all } R_n \text{ of } G. \quad (E-4)$$

For a finite group, the number of elements in the set is equal to the order of the group (h).

E-II. Symmetry Operations

In crystallography, the elements of the group are symmetry operations that transform a molecule or a crystal into itself,

these operations are:

I : identity.

C_n : rotation by $2\pi/n$ about an axis ($n=2,3,4,6$).

i : center of symmetry (inversion).

S_n : rotation of $2\pi/n$ followed by reflection in a plane perpendicular to the axis.

$\sigma_v, \sigma_h, \sigma_d$: reflection plane (mirror) oriented vertically (v), horizontally (h) or diagonally (d) with respect to the vertical axis of highest order.

$\{\sigma_n | \vec{\tau}\}$: glide plane; reflection followed by translation along the plane ($n = v, h, d$)

$$\vec{\tau} = \sum_{i=1}^3 x_i \vec{a}_i \quad (x_i \text{ fraction} < 1; \quad \vec{a}_i \text{ lattice vectors}) \quad (\text{E-5})$$

$\{C_n | \vec{\tau}\}$: screw axis: rotation followed by a translation $\vec{\tau}$ along the axis.

The first five operations define the elements of the point groups (finite groups); when these operations are multiplied by the translation vector group ($\vec{\tau}$)

$$\vec{\tau} = \sum_{i=1}^3 n_i \vec{a}_i \quad (n_i \text{ integers}) \quad (\text{E-6})$$

and added to the last two operations, they form the possible elements $\{R | \vec{\tau}\}$ of the space groups (infinite groups). For the last two operation [81b] to be elements of a group, C_n, σ_n and

\vec{t} (taken separately) should not be symmetry operations of the group. If we apply the space group operation on a vector \vec{b} , we get

$$\{R|\vec{t}\}\vec{b} = R\vec{b} + \vec{t} \quad (\text{E-7})$$

The operations R_i of the group G will form classes if they obey the similarity transformation

$$X^{-1}R_iX = R_j \quad (\text{E-8})$$

where X is all the operations of the group for a fixed R_i ; the R_j are a small number of operation. The operation in a class will all be of the same order (same type of operation).

E-III. Irreducible Representations and Characters

For each operation R of a group G there exists an infinite number of square matrices $\Gamma(R)$ that represent the operation, but there is a special set of representations called the irreducible representations (i.r.). The $\Gamma(R)$ of the group can be simultaneously transformed, for all R , by a similarity transformation into block-diagonal form:

$$\Gamma'(R) = S^{-1}(R)S = \begin{bmatrix} \Gamma_1(R) & 0 \\ 0 & \Gamma_2(R) \end{bmatrix} \quad (\text{E-9})$$

where S is a non-singular unitary $\ell \times \ell$ matrix (dimension ℓ).

The $\Gamma_i(R)$ are $\ell_i \times \ell_i$ matrices ($\ell = \ell_1 + \ell_2$) and are said to be irreducible representations if neither can be further transformed to smaller-dimension block form. The expression E-9 can be symbolically written as (direct sum):

$$\Gamma'(R) = \Gamma_1(R) + \Gamma_2(R) \quad (E-10)$$

We define the character $\chi_i(R)$ of a representation $\Gamma_i(R)$ as the trace of the matrix representation

$$\chi_i(R) = \sum_j \Gamma_i(R)_{jk} \delta_{jk} \quad (E-11)$$

with $\Gamma_i(R)_{jk}$, the matrix element of the i -th irreducible representation for the operation R of the group G ; the trace of each matrix in a representation is unaltered by a similarity transformation.

The characters of the i.r. of a group will have the following properties:

a) The characters of operations in the same class are identical.

b) When summed over all the classes c of operations of the group, the character system of i.r. is orthogonal, and normalized to the order h of the group

$$\sum_c \chi_i(c)^* \chi_j(c) N_c = h \delta_{ij} \quad (E-12)$$

where $\chi_i(c)$ is the character of the i -th i.r. of the c -th

class which contains N_c operations (the star means that we have to take the complex conjugate of the character).

c) Two representations are equivalent if the characters of each class of the representations are equal (necessary and sufficient condition).

d) If l_i is the dimension (degeneracy) of the i -th i.r. of the group and that we sum for all inequivalent i.r., we have

$$\sum_i l_i^2 = h \quad (\text{E-13})$$

e) The number of inequivalent i.r. is equal to the number of classes in the group.

If the character of a reducible representation Γ for each class c of symmetry operations, is $\chi(c)$, then the reduction (equ. E-9) decomposes the arbitrary representation into n_i i.r. Γ_i of the group, with character $\chi_i(c)$

$$\Gamma = \sum_i n_i \Gamma_i \quad (\text{E-14a})$$

$$n_i = \frac{1}{h} \sum_c \chi_i(c)^* \chi(c) N_c \quad (\text{E-14b})$$

E-IV. Application to Phonons

These notions can be applied to the labelling of the normal modes of vibration of molecules (point group) and crystals (space group). For simplicity, we will look at the

phonons of $\epsilon\text{-In}_2\text{Se}_2$ (D_{3h}^1 , $P\bar{6}m2$) and its character table is in Table E-Ia. In table E-II we present the notations used in group theory.

We can consider a crystal as made up of identical molecules (primitive cell) and use its point group. For the approach to be valid all the cells have to vibrate in phase and only the $\vec{k} = 0$ phonons will be identified; with first-order Raman scattering, these are the only phonons that will be observed. We can use the symmetry operations of the point group if the space group does not contain any screw axis or glide plane. In table E-III we present the space group operations of $\beta\text{-In}_2\text{Se}_2$ (D_{6h}^4 , $P6_3/mmc$) and the equivalent (isomorph) point group D_{6h} ; we also give the character table of D_6 from which we can obtain the character table of D_{6h} . The labelling of the i.r. of the space group will be the same as the isomorphic point group.

Looking at the structure of $\epsilon\text{-In}_2\text{Se}_2$ (fig. II-3a) we find that the primitive cell contains 8 atoms, with three degree of freedom for each, which give 24 normal modes of vibration. To obtain the i.r. of these modes we have to apply to the molecule (or the atoms in the primitive cell) all the symmetry operations of the group. If at each atom of the molecule (or in the primitive cell) we attach a coordinate system (x_i, y_i, z_i), we can represent each operation as a 24 x 24 matrix that transforms the vector

$(x_1, y_1, z_1, \dots, x_8, y_8, z_8)$; this matrix is formed of 3 x 3 rotation sub-matrices. The trace of the large matrix for each operation will be the character of this operation. Only the $N(c)$ atoms that are undisplaced by a rotation of θ of the molecule will have their rotation submatrix along the diagonal of the large matrix and the character for all motions of the molecule is

$$\chi(m) = (\pm 1 + 2\cos \theta)N(c) \quad (E-15)$$

with + for proper rotations and - for improper rotation (a rotation followed by a mirror plane or an inversion); the axis of highest order has to be the z axis. The reducible representation is given in Table E-Ib.

To find the reduction of this representation into i.r. of the group we have to use equ. E-14 which gives

$$\Gamma(m) = 4A_1' + 4A_2'' + 4E' + 4E'' \quad (E-16)$$

The acoustic modes are equivalent to the translation of the molecule as a whole and its character is

$$\chi(t) = (\pm 1 + 2\cos \theta) = \chi(\mu) \quad (E-17)$$

which in our example reduces to $A_2'' + E'$; for these modes at $\vec{k} = 0, \omega = 0$. The electric dipole operator behaves like x, y or z and the representations of the infrared (IR) active phonons will be $\chi(\mu)$, which is the same as $\chi(t)$:

$A_2'' + E'$; after subtracting the acoustic i.r. from D-16 we are left with

$$\Gamma(\mu) = 3A_2'' + 3E' \quad (E-18)$$

The Raman active modes will have the i.r. of the polarisability, which behaves like $x^2, y^2, z^2, xy, yz, zx$ (second-rank tensor) or like the symmetrical direct produce of the infrared representation (see next section)

$$[\Gamma(\mu) \times \Gamma(\mu)] = \Gamma(\alpha) \quad (E-19)$$

After reduction, the i.r. of the Raman modes are A_1', E' and E'' ; this implies that the E' infrared modes will also be Raman active. And we have for the Raman modes

$$\Gamma(\alpha) = 4A_1' + 3E' + 4E'' \quad (E-20)$$

The A_1' and A_2'' (longitudinal) modes are non-degenerate and the E' and E'' (transverse) are doubly degenerate; an infrared spectrum will show 6 peaks, while the Raman spectrum will show 11 peaks. All the modes having the same i.r. will in general be non-degenerate; accidental degeneracy is always possible and can be found by solving the dynamical matrix, with the appropriate force constants, which can be solved using the symmetries of the problem [75b].

E-V. Direct Product and Selection Rules

The product of two i.r. (Γ_i, Γ_j in G) of dimension n and m respectively give, in general, a reducible representation Γ of dimension $\ell = n.m$

$$\Gamma = \Gamma_i \times \Gamma_j \quad (\text{E-21a})$$

with character given by

$$\chi(c) = \chi_i(c)\chi_j(c), \quad \text{for all } c \text{ of } G \quad (\text{E-21b})$$

the reduction obtained with equ. E-14. In the case where $i = j$, the characters are, for the symmetrical product (square brackets) and the antisymmetrical product (curly brackets)

$$\chi[\Gamma_i^1 \times \Gamma_i^2] = \frac{1}{2}[(\chi(R))^2 + \chi(R^2)] \quad (\text{E-22a})$$

$$\chi\{\Gamma_i^1 \times \Gamma_i^2\} = \frac{1}{2}\{(\chi(R))^2 - \chi(R^2)\} \quad (\text{E-22b})$$

Γ_i^1 and Γ_i^2 correspond to two different modes (operators, electrons, functions) having the same i.r. and to differentiate them, they receive an additional label (Γ_{8g}^1 and Γ_{8g}^2 in part I; A_{2u}^1 and A_{2u}^2 in part II). An example of symmetrical direct product is given in section E-IV.

The direct product can be used to find if a certain interaction is allowed (part II, section I.3); it can also be used to find the polarisation conditions for a certain transition (part I, section III.1.2).

E-VI. Double Groups

The full rotation group is the group containing the symmetry operations of the sphere and is related to the symmetries of the free atom or ion. If this ion is placed in a crystal, the spherical symmetry will be reduced to the local symmetry. From quantum mechanics, we know that an arbitrary rotation of a spherical harmonic can be expressed as a linear combination of the other spherical harmonics with the same ℓ (positive integers) but different m

$$R(0,0,\alpha)Y_m^\ell(\theta,\phi) = \sum_{m'} D_{m',m}^\ell(0,0,\alpha)Y_{m'}^\ell(\theta,\phi) \quad (E-23)$$

where $-\ell \leq m' \leq \ell$ and the rotation is by an angle α about the z axis. From the properties of the spherical harmonics we have

$$R(0,0,\alpha)Y_m^\ell(\theta,\phi) = Y_m^\ell(\theta,\phi-\alpha) = Y_m^\ell(\theta,\phi)\exp(-im\alpha) \quad (E-24a)$$

and

$$D_{m',m}^\ell(0,0,\alpha) = \delta_{m',m} \exp(-m\alpha) \quad (E-24b)$$

which is a diagonal matrix, with character

$$\chi^\ell(\alpha) = \sum_{m=-\ell}^{+\ell} \exp(-m\alpha) = \frac{\sin(\ell+1/2)\alpha}{\sin(\alpha/2)} \quad (E-25)$$

In a crystal α will take specific values ($\alpha = 2\pi/n$; $n = 1, 2, 3, 4, 6$) and the corresponding representations will be, in general, reducible.

If the spin is included in the problem, the character of the representation will be

$$\chi^j(\alpha) = \frac{\sin(j+1/2)\alpha}{\sin(\alpha/2)} \quad (\text{E-26})$$

with j a half-odd-integer (odd number of electrons); in this case a rotation of $(\alpha+2\pi)$ will change the sign of the character

$$\chi^j(\alpha+2\pi) = (-1)^{2j} \chi^j(\alpha) \quad (\text{E-27})$$

We can introduce a fictitious operator R (rotation of 2π) which will double the number of operations of the group, but not the number of classes; C_2 and RC_2 belong to the same class (the same for σ and $R\sigma$):

$$\chi^j(\pi) = \chi^j(3\pi) = 0 \quad (\text{E-28})$$

In Koster [72] notation $RO = \bar{O}$ with O the operations of the single point group. The number of new irreducible representations is equal to the number of additional classes. The order of the group is doubled and the dimensions of the new i.r. can be obtained from equ. E-13. For the O_h group, there are 6 additional i.r.: $\Gamma_{6g}(2)$, $\Gamma_{6u}(2)$, $\Gamma_{7g}(2)$, $\Gamma_{7u}(2)$, $\Gamma_{8g}(4)$ and $\Gamma_{8u}(4)$ with their respective dimensions (degeneracy) in parenthesis.

E-VII. Remarks and References

Equ. E-14b is valid only if a symmetry element R and its inverse (R^{-1}) are members of the same class; if it is not the case, the following more general relation should be taken.

$$n_j = \frac{1}{h} \sum_R \chi_j^*(R) \chi(R) \quad (\text{E-29})$$

A more precise analysis for the phonons modes numbers and species can be found in Bhagavantan et al [83]. The books of Falicov [79] and Tinkham [63] are good starting points for beginners in the study of group theory in general. The application of this theory to solid state can be found in Cracknell's book [78] which also contains reprints of some fundamental articles on the subject. For most advanced treatments of the applications of group theory, many books are available [42,80,82].

Table E-I. a) Character Table of $D_{3h}(\bar{6}m2)$ point group

The top row gives the 12 symmetry operations (in Schoenflies notation) grouped in 6 classes. The first column gives the irreducible representations (i.r.) in the Koster (K) [72] notation and the second column is the Mulliken notation (M) [80]. The basis functions are given only for the optically active (O.A.) i.r. (R: Raman, IR: infrared). Note that a $\Gamma_6(E')$ phonon will be both infrared and Raman active.

K	M	I	$2C_3$	$3C_2$	σ_h	$2S_3$	$3\sigma_v$	Basis	O.A.
Γ_1	A_1'	1	1	1	1	1	1	(x^2+y^2) or z^2	R
Γ_2	A_2'	1	1	-1	1	1	-1		
Γ_3	A_1''	1	1	1	-1	-1	-1		
Γ_4	A_2''	1	1	-1	-1	-1	1	z	IR
Γ_5	E''	2	-1	0	-2	1	0	xy and yz	R
Γ_6	E'	2	-1	0	2	-1	0	(x^2-y^2) and xy	R
								x and y	IR

Table E-1. b) Reducible character of atom motion in the primitive cell. Character of reducible representations for all motions $\Gamma(m)$, for translation $\Gamma(t)$, for electric dipole $\Gamma(\mu)$ and for polarisability $\Gamma(\alpha) = [\Gamma(\mu) \times \Gamma(\mu)]$ ($N(c)$ is the number of atoms in the molecule that are undisplaced by the symmetry operations of a class c).

type:	I	$2C_3$	$3C_2$	σ_h	$2S_3$	$3\sigma_v$
	[proper]	[improper
θ°	0	120	180	0	120	0
$\cos\theta$	1	-1/2	-1	1	-1/2	1
$(\pm 1 + 2\cos\theta)$	3	0	-1	1	-2	1
$N(c)$	8	2	0	0	0	8
$\Gamma(m)$	24	0	0	0	0	8
$\Gamma(t)$	3	0	-1	1	-2	1
$\Gamma(\mu)$	3	0	-1	1	-2	1
$\Gamma(\alpha)$	9	0	1	1	4	1

From equ. 14b and for $\Gamma(m)$ (using Table E-I. a,b)

$$n(A_1) = \frac{1}{12} [(1 \cdot 24 \cdot 1) + (1 \cdot 0 \cdot 2) + (1 \cdot 0 \cdot 3) + (1 \cdot 0 \cdot 1) + (1 \cdot 0 \cdot 2) + (1 \cdot 8 \cdot 3)] = 4$$

Table E-II. Notation

A) Space Groups

a) Schoenflies notation (D_{3h}^1, D_{6h}^4); does not contain much information on the symmetries.

b) International notation ($P\bar{6}m2, P6_3/mmc$) with correspondance to Schoenflies operations in square brackets.

- Structure of unit cell

P: primitive

I: body-centered

N: center of N-face ($N = A, B, C$)

F: face-centered

R: rhombohedral centered

- Symmetry elements

1: no symmetry (identity) [I or E]

$\bar{1}$: center of symmetry (inversion) [i or I]

X: X-fold rotation axis ($X = 2, 3, 4, 6$) [C_n ; $n=X$]

\bar{X} : X-fold rotation followed by the inversion [S_n]*

X_p : X-fold rotation followed by a translation of fraction p/X along c axis (screw axis) [$\{C_n | \frac{p}{X}\}$]

$m, \bar{2}$: reflection plane (mirror) [σ]

X/m: mirror plane perpendicular to the X-fold axis [σ_h]

Table E-II. (Cont'd)

a,b,c: axial glide plane: a reflection followed by a translation in the plane of $a/2$, $b/2$ or $c/2$ along the x,y or z axis (or $(a+b+c)/2$ along [111] on rhombohedral axis).

n: diagonal glide plane: a reflection followed by a translation in the plane of $(a+b)/2$, $(b+c)/2$ or $(c+a)/2$, or for tetragonal and cubic systems, of $(a+b+c)/2$.

d: diamond glide plane: reflection followed by a translation in the plane of $(a+b)/4$, $(b+c)/4$, or $(c+a)/4$, or for tetragonal and cubic systems, of $(a+b+c)/4$. Glide planes in Schoenflies are $\{\sigma|\tau\}$.

Example: $P6_3/mmc$ (D_{6h}^4 : $\beta\text{-In}_2\text{Se}_2$):

- the cell is primitive with $z = c$ the axis of highest symmetry; this axis is a screw axis with translation of $(3/6)c$; there is a mirror plane perpendicular to it and a mirror plane parallel; there is a glide plane in the c axis with translation $c/2$; other symmetry operations can be generated by these.

*Note that $\bar{3} = iC_3 = \sigma_h C_6 = S_6$ and $\bar{6} = iC_6 = \sigma_h C_3 = S_3$

Table E-II. (cont'd)

B) Notation of the irreducible representations (i.r.) for the point groups

a) Mulliken (or chemical) [77,80]:

dimension of i.r.	label
1	A,B
2	E
3	F or T
4	G

b) Herring [80]: $\Gamma_1, \dots, \Gamma_n$ with Γ_5 and Γ_6 interchanged with respect to Koster notation; only used for the groups $C_{6v}(6mm)$, $D_{3h}(\bar{6}m2)$, $D_6(622)$ and $D_{6h}(6/mmm)$.

c) Koster et al. [72]: $\Gamma_1, \dots, \Gamma_n$.

C) Additional labelling of the i.r.

a) subscript $\rightarrow 1,2,3$: to differentiate i.r. of the same dimension (Mulliken); g or u: to identify the i.r. that are even or odd under inversion (Mulliken, Koster).

b) standard superscript \rightarrow prime (') or double-prime ("): to differentiate i.r. that are even or odd for the mirror plane containing the axis of rotation of highest symmetry (Mulliken); + or -: equivalent to g or u subscript (Koster).

Table E-II. (Cont'd)

- c) arbitrary superscript $\rightarrow 1, 2, \dots, n$: to differentiate two or more equivalent i.r. belonging to the same system (electron levels, phonons); other notations for this case exist in the literature [61].

Table E-III. Space Group D_{6h}^4 ($P6_3/mmc$) and correspondance to D_{6h} point group [76]

D_{6h}^4	$\{I \vec{t}\}$	$2\{C_6 \vec{t}\}$	$2\{C_3 \vec{t}\}$	$\{C_2 \vec{t}\}$	$3\{C_2' \vec{t}\}$	$3\{C_2'' \vec{t}\}$
D_{6h}	I	$2C_6$	$2C_3$	C_2	$3C_2'(y)$	$3C_2''(x)$
D_{6h}^4	$\{i \vec{t}\}$	$2\{S_3 \vec{t}\}$	$2\{S_6 \vec{t}\}$	$\{\sigma_h \vec{t}\}$	$3\{\sigma_d \vec{t}\}$	$3\{\sigma_v \vec{t}\}$
D_{6h}	i	$2S_3$	$2S_6$	σ_h	$3\sigma_d$	$3\sigma_v$

$\vec{t} = n_1\vec{a} + n_2\vec{b} + n_3\vec{c}$ (n_i integers; $\vec{a}, \vec{b}, \vec{c}$, primitive lattice vectors)

$\vec{t} = (\vec{c}/2)$

Character table of D_6 ($D_{6h} = D_6 \times i$) single group*

		I	$2C_6$	$2C_3$	C_2	$3C_2'$	$3C_2''$
Γ_1	A_1	1	1	1	1	1	1
Γ_2	A_2	1	1	1	1	-1	-1
Γ_3	B_1	1	-1	1	-1	1	-1
Γ_4	B_2	1	-1	1	-1	-1	1
Γ_5	E_1	2	1	-1	-2	0	0
Γ_6	E_2	2	-1	-1	2	0	0

$\Gamma_j^+, \Gamma_j^-, H_{jg}, H_{ju}$ ($H = A, B, E$): even (+,g) or odd(-,u) under inversion.

$$S_3 = iC_6, \quad S_6 = iC_3, \quad \sigma = iC_2$$

Table E-III. (Cont'd)

Basis function of D_{6h} and optical activity

Γ_1^+	$(x^2 + y^2)$ or z^2	Raman
Γ_5^+	xz and yz	Raman
Γ_6^+	$(x^2 - y^2)$ and xy	Raman
Γ_2^-	z	Infra-Red
Γ_5^-	x and y	Infra-Red

APPENDIX F.Deconvolution Method

Fig. F-1 was constructed from Lorentzian functions of the form

$$I_i(\bar{\nu}) = \frac{A_i \gamma_i^2}{(\bar{\nu} - \bar{\nu}_i)^2 + \gamma_i^2} \quad (F-1)$$

where A_i is the maximum of the intensity at $\bar{\nu} = \bar{\nu}_i$ and γ_i is the half-width at half-maximum; the parameters used to construct the figure are in Table F-Ia. In the region of interest ($200-400\text{cm}^{-1}$) the contribution of the wing of the two-phonon band is simulated by peak D. For the deconvolution of the temperature dependant spectra the following method was used. The minima before and after the doublet are joined by a straight line (H-H' in Fig. F-1); the intensity of peak A is measured vertically from this line to the maximum (A'-A). We symmetrize peak A for the portion (L-L') corresponding to the position of peak B; from the intensity measured from this line to the maximum (X-B) we subtract the component S. This method of deconvolution removes a large part of the contribution of the background; it under-evaluates the true ratio (see Table F-Ib) but will better translate the behaviour of the peaks as a function of temperature than the ratio of the total signal for each peak. This method does not permit to evaluate the half-width at half-maximum.

Table F-I. a) Convolution parameters for Fig. F-1.

Peak	$\bar{\nu}_f$ (cm^{-1})	A_f (arb.)	γ_f (cm^{-1})
A	280	13.0	18
B	305	2.8	4
C	372	4.2	8
D	420	9.0	120

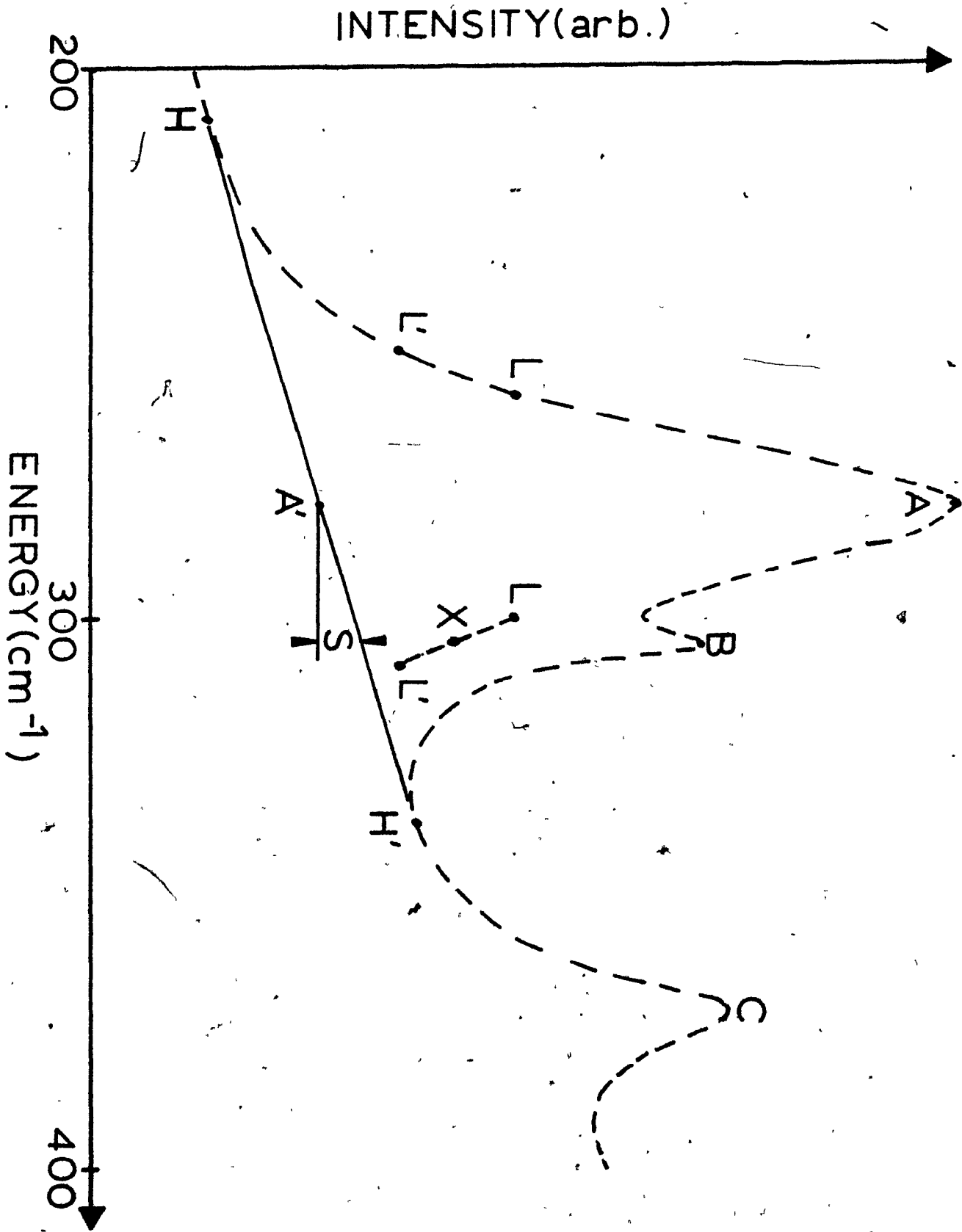
b) Ratios of the intensities of the doublet (A,B)
(the total entry corresponds to the intensities
measured from the horizontal axis).

$$I(280\text{cm}^{-1})/I(305)$$

Exact	(13.0/2.8)	=	4.64
Deconvoluted	(11.3/3.5)	=	3.63
Total	(15.3/10.8)	=	1.42

Fig. F - 1. Example of a spectrum and its deconvolution.

The dashed curve is the sum of four Lorentzians with the parameters given in Table F-1. The method of deconvolution is explained in the text of the Appendix.



C

O

REFERENCES

1. R.S. Krishnan in The Raman Effect, Volume 1 (Marcel Dekker Inc., N.Y., 1971; A. Anderson ed.) p.2.
2. M. Born and K. Huang, Dynamical Theory of Crystal Lattices (Oxford University Press, 1954).
3. E. Wigner in A.P. Cracknell, Applied Group Theory (Pergamon Press, 1968) p.199.
4. R. Loudon, Advanc. in Phys. 13, 423 (1964).
5. A. Mooradian and G.B. Wright, Sol. State Comm. 4, 431 (1966).
6. S.P.S. Porto, P.A. Fleury and T.C. Damen, Phys. Rev. 154, 522 (1967).
7. M. Krauzman, C.R. Acad. Sc. (Paris) 266, 186 (1968).
8. N.B. Manson, W. Von der Ohe and S.L. Chodos, Phys. Rev. B3, 1968 (1971).
9. D.G. Boziniis and J.P. Hurrell, Phys. Rev. B13, 3109 (1976).
10. A. Mooradian and A.L. McWorther, Phys. Rev. Lett. 19, 849 (1967).
11. A. Mooradian in Laser Handbook (North-Holland Pub. Co., Amsterdam 1972; F.T. Arecchi and E.O. Schulz-du Bois, eds) Volume II, p.1433.
12. P.A. Fleury and R. Loudon, Phys. Rev. 166, 514 (1968).
13. D.J. Lockwood, G. Mischler, I.W. Johnstone and M.C. Schmidt, J. Phys. C12, 1955 (1979).
14. C.H. Henry, J.J. Hopfield and L.C. Luther, Phys. Rev. Lett. 17, 1178 (1966).

15. D.D. Manchon, Jr. and P.J. Dean in Proceed. of the Xth Intern. Conf. on the Physics of Semiconductors, Cambridge, Mass., U.S.A., August 1970 (U.S. Atomic Energy Commission, Washington 1970) p.760.
16. L.L. Chase and D. Walsh in Proceed. of the XIVth Intern. Conf. on the Physics of Semiconductors, Edinburgh 1978 (Institute of Physics, Bristol, London 1979; B.L.H. Wilson ed.) p.533.
17. J.A. Koningstein and O.S. Mortensen in The Raman Effect (Marcel Dekker Inc., N.Y. 1973; A. Anderson ed.) p.519.
18. D.J. Lockwood and N.L. Rowell in Proceed. from the VIIth Intern. Conf. on Raman Spectroscopy, Ottawa 1980 (North-Holland; W.F. Murphy ed.) p. 154.
19. J.E. Kardontchik, E. Cohen and J. Makovsky, Phys. Rev. B13, 2955 (1976).
20. M.D. Sturge, Solid State Phys. 20, 91 (1967).
21. J.P. Mon, Phys. Lett. 36A, 479 (1971).
22. A. Billat, J.P. Mon and M. Voisin, Phys. Stat. Sol. (b) 67, 335 (1975).
23. S. Guha, Phys. Rev. B21, 5808 (1980).
24. D.G. Mead and J.C. Irwin, Sol. State Comm. 20, 855 (1976).
25. S. Jandl and C. Carlone, Sol. State Comm. 25, 5 (1978).
26. D. Walsh, S. Jandl and J.Y. Harbec, J. Phys. C13, L125 (1980).
27. W. Heitler, The Quantum Theory of Radiation (Clarendon Press, Oxford, 3rd ed;1954) p.192.

28. E.E. Anderson, Modern Physics and Quantum Mechanics, (W.B. Saunders Co., 1971) p.314.
29. C.Y. Fong, W. Saslow and M.L. Cohen, Phys. Rev. 168, 992 (1968).
30. F. Bassani and B. Preziosi, Electrons in Crystalline Solids, Lectures of an International Course, Trieste 1972 (International Energy Agency, 1973) p.619.
31. A. Abragam and B. Bleaney, Electron Paramagnetic Resonance of Transition Ions (Clarendon Press, Oxford 1970) p.367.
32. E. Low, Phys. Rev. 109, 256 (1958).
33. T. Ray and J.R. Regnard, Phys. Rev. B9, 2110 (1974).
34. F.S. Ham, W.M. Schwarz and M.C.M. O'Brien, Phys. Rev. 185, 548 (1969).
35. We used the formulae of Ref. 34 and transformed them with the relation $L_{\pm} = L_x \pm iL_y$.
36. R.C. Whited, C.F. Flaten and W.C. Walker, Sol. State Comm. 13, 1903 (1973).
37. M.V. Andriyashik, M. Yu Sakhnovskii, V.B. Timofeey and A.S. Yakimova, Phys. Stat. Sol. 28, 277 (1968).
38. J.P. Larkin, F.G. Imbusch and F. Draynieks, Phys. Rev. B7, 495 (1973).
39. S.D. Ross, Inorganic Infrared and Raman Spectra (McGraw-Hill, 1972).
40. H. Marantz, R.I. Rudko and C.L. Tang, IEEE J. Quantum Electronics QE5, 38 (1969); we also looked at the scattered light from a sample of indium selenide with the laser ignited by not lasing.

41. R.A. Cowley in the Raman Effect, Vol. 1 (Marcel Dekker, Inc., N.Y. 1971; A. Anderson, ed) p.117.
42. J.L. Birman in Handbuch der Physik Vol. XXV/2b, Light and Matter Ib (Springer-Verlag, Berlin 1974; S.Flügge and L. Genzel ed.), p.321.
43. A.A. Maradudin, in Proc. First Intern. Conf. on Localized Excitations in Solids, U. of California, Irvine, Sept. 1967 (Plenum Press, N.Y., 1968) p.1.
44. Crystal Data, Determinative Tables, J.D.H. Donnay and G. Donnay eds., American Crystallographic Association Monograph 5, Williams and Heintz Map Corp., Washington 1963.
45. M.J.L. Sangster, J. Phys. C14, 2889 (1981).
46. M.J.L. Sangster, D.K. Rowell and A.S. Ashman, J. Phys. C14, 2899 (1981).
47. G. Peckham, Proc. Phys. Soc. (London) 90, 657 (1967).
48. M.J.L. Sangster, G. Peckham and D.H. Saunderson, J. Phys. C3, 1026 (1970).
49. P. Cossee, Molec. Phys. 3, 125 (1960).
50. A.D. Liehr, J. Phys. Chem 67, 1314 (1963).
51. J.E. Ralph and M.G. Townsend, J. Chem. Phys. 48, 149 (1968).
52. J.Y. Wong, Phys. Rev. 168, 337 (1968).
53. E.U. Condon and G.H. Shortley, The Theory of Atomic Spectra (Cambridge University Press, London; 1977) p.193.

54. W.Thorson and W. Moffitt, Phys. Rev. 168, 362 (1968).
55. A.L. Shawlow, A.H. Piksis and S.Sugano, Phys. Rev. 122, 1469 (1961).
56. J.E. Wertz, J.W. Orton and P. Auzins, J. of Appl. Phys. Suppl. to Vol. 33, 322 (1962).
57. A.J. Mann and P.J. Stephens, Phys. Rev. B9, 863 (1974).
58. V. Wagner and P. Koidl, Proceed. of the Intern. Conf. on Magnetism, Munich, Germany, Sept. 1979 in J. Magn. and Magn. Mater. (Netherlands) 15-18, 33 (1980).
59. E. Mooser and M. Schlüter, Nuovo Cimento 18B, 164 (1973) Fig. 1.
60. E. Mooser, I. Ch.Schlüter and M. Schlüter, J. Phys. Chem. Solids 35, 1269 (1974).
61. R.M. Hoff, J.C. Irwin and R.M.A. Lieth, Can. J. Phys. 53, 1606 (1975) Fig. 2 and 3.
62. T.J. Wieting and J.L. Verble, Phys. Rev. B5, 1473 (1972).
63. M. Tinkham, Group Theory and Quantum Mechanics (McGraw-Hill 1964) p.249.
64. J. Trudel, D. Walsh and G. Donnay in Proceed. of the VIIth Intern. Conf. on Raman Spectroscopy, Ottawa, Canada 1980 (North-Holland, 1980; W.F. Murphy ed.) p.72.
65. J.C. Irwin, R.M. Hoff, B.P. Clayman and R.A. Bromley, Sol. State Comm. 13, 1531 (1973).
66. G.L. Belenkii, L.N. Alieva, R. Kh. Nani and E. Yu. Salaev, Phys. Stat. Sol. (b) 82, 705 (1977).

- ()
67. T.J. Wieting, Sol. State Comm. 12, 931 (1973).
 68. C. Carlone and S. Jandl, Sol. State Comm. 29, 31 (1979).
 69. J. Kanamori, Progr. Theor. Phys. 17, 177 (1957).
 70. E.B. Tucker, Phys. Rev. 143, 264 (1966).
 71. N.S. Hush, Disc. Faraday Soc. 26, 138 (1958).
 72. G.F. Koster, J.O. Dimmock, R.G. Wheeler, H. Statz, Properties of the Thirty-Two Point Groups (M.I.T. Press, Cambridge, Mass.; 1963).
 73. H.A. Jahn and E. Teller, Proceed. Roy. Soc. (London) A161, 220 (1937).
 74. H.A. Jahn, Proceed. Roy. Soc. (London), A164, 117 (1938).
 75. G. Herzberg, Molecular Spectra and Molecular Structure II - Infrared and Raman Spectra of Polyatomic Molecules (Van Nostrand Reinhold, Toronto, 1945) a:p261, b:p145.
 76. G.F. Koster, Space Groups and Their Representations, in Solid State Physics Vol. 5 (ed: F. Seitz and D. Turnbull: 1957) p. 173.
 77. G. Burns, Introduction to Group Theory with Applications (Material Sciences Serie, Academic Press 1977; ed.: A.M. Alper and A.S. Nowick).
 78. A.P. Crackwell, Applied Group Theory (Pergamon Press, 1968).
 79. L.M. Falicov, Group Theory and Its Physical Applications (University of Chicago Press, 1966).
 80. M. Lax, Symmetry Principles in Solid State and in Molecular Physics (Wiley Interscience; John Wiley and Sons, N.Y. 1974).

81. N.W. Ashcroft and N.D. Mermin, Solid State Physics (Holt, Rinehart and Winston; 1976) a:p547; b:p126.
82. M. Hamermesh, Group Theory and Its Applications to Physical Problems (Addison-Wesley, Mass. 1962).
83. S.B. Bhagavantán and T. Venkatarayudu, Theory Groups and Its Application to Physical Problems (Bangalore Press; Waltair India, 1948) p. 106.
84. T.J. Wieting and J.L. Verble, in Electrons and Phonons in Layered Crystals Structures, Volume 3 of Physics and Chemistry of Materials with Layered Structures (Reidel 1979; T.J. Wieting and M. Schlüter, ed.) a:p323; b:p399; c:p398; d:p365; e:p364.
85. J.C. Phillips, Phys. Rev. 188, 1225 (1968).
86. H. Uwe and T. Sakudo, Phys. Rev. B15, 737 (1977).
87. K.P. Lee and D. Walsh, Phys. Lett. A27, 17 (1968).
88. A. Jesion, Y.H. Shing and D. Walsh, Phys. Rev. Lett. 35, 51 (1975).
89. E. Cohen, M.D. Sturge, R.J. Birgenau, E.I. Blount, L.G. Van Uitert and J.K. Kjems, Phys. Rev. Lett. 32, 232 (1974).
90. R.J. Elliott, R.T. Harley, W. Hayes and S.R.P. Smith Proc. Roy. Soc. London A328, 217 (1972).
91. J.C. Walling in Laser Focus, 18, No. 2, 45 (1982).
92. L.F. Johnson, H.J. Guggenheim and R.A. Thomas, Phys. Rev. 149, 179 (1966).
93. Alain Pofrier, Ph.D. Thesis, McGill University, Montreal, 1982.

(1)
94. ~~Bill~~ Cowan, Ph.D. Thesis, McGill University, Montreal,
1976..

95. B.R. Judd, Can J. Phys. 52, 999 (1974).